UNIVERSITY OF BIRMINGHAM

Advanced Micro-Engineered Platforms for Novel Device Technologies

By

JONATHAN JAMES STANLEY RICKARD

A thesis submitted to the University of Birmingham for the degree of DOCTOR OF PHILOSOPHY

College of Engineering and Physical Sciences
School of Chemical Engineering
University of Birmingham
December 2017

Abstract

The objectives of this thesis are to explore, design, fabricate and implement the use of advanced micro-engineered platforms to be exploited as versatile, novel device technologies.

An increasing number of technologies require the fabrication of conductive structures on a broad range of scales and large areas. Here, we introduce advanced yet simple electrohydrodynamic lithography for patterning conductive polymers directly on a substrate with high-fidelity. We illustrate the generality of this robust, low-cost method by structuring thin films *via* electric-field-induced instabilities, yielding well-defined conductive structures with a broad range of feature sizes. We show the feasibility of the polypyrrole-based structures for field-effect transistors, which might herald a route towards submicron device applications.

We also demonstrate a miniaturised platform technology for timely, sensitive and rapid point-of-care diagnostics of disease-indicative biomarkers. Our micro-engineered device technology (MEDTech) is based on reproducible electrohydrodynamically fabricated platforms for surface enhanced Raman scattering enabling tuneable, high-throughput nanostructures yielding high-signal enhancements. These, integrated within a microfluidic-chip provide cost-effective, portable devices for detection of *miniscule* biomarker concentrations from biofluids, offering clinical tests that are simple, rapid and minimally invasive. Using MEDTech to analyse clinical blood-plasma, we deliver a prognostic tool for long-term outcomes, in the hospital or at the point-of-care.

To the One

Acknowledgements

The work in this thesis was carried out under the supervision of **Dr Pola Goldberg Oppenheimer,** head of the Advanced Nano-Materials Structures and Applications (ANMSA) group in the school of Chemical Engineering at the University of Birmingham. I would like to take this opportunity to express my appreciation and gratitude to all those who have contributed to this fascinating journey in my mature years.

First and foremost, I would like to express my deepest gratitude to **Dr Goldberg Oppenheimer** for believing in my abilities and giving me the opportunity to carry out this exciting research and guiding me with her experience, wisdom and supporting me to follow and try my ideas. Her relaxed and understanding nature, inspiring ideas, enthusiasm and long chats about all things science and beyond have all contributed towards this amazing journey through my PhD.

My highest gratitude goes to my second supervisor **Professor Liam Grover** for fond conversations and a touch of humour about every aspect of life. I would also like to thank the support of the ANMSA group which **Pola** has made an international and friendly place to be a part of with everyone helping each other. In particular, **Chiara Busa** who was with me at the genesis of the group and we have together been an integral part of the development of the ANMSA group. Special words of appreciation to **Professor Quentin Ramasse**, for his kind words of recommendation and his motivating support and engorgement.

A special thank you goes to all the administrative staff at the School Chemical Engineering and especially, **Mrs Lynn Draper** for always smiling and being so helpful and encouraging. I would also like to thank **Ms Sarah Fleming** for her rapid

professional support. I also thank all the technical support staff at the Biochemical Engineering Laboratories and in particular, Ms **Elaine Mitchell** for her invaluable help and Mr **Dave Smith** for his help and our chats on music and gigs.

I am grateful to the Cavendish Laboratory, Electron Microscopy suite team including, **Dr Richard Langford**, **Eric Tapley** and **Melvyn Marsh** for their help and support and the use of the electron and ion beam microscopes. I also thank the **Electronics Group** at the Cavendish Laboratory of the University of Cambridge for their kind help and use of etching equipment in particular, **Huw Prytherch** and **Barry Shores** for trying to drill impossibly small holes close together. I am also grateful to **Nigel Palfrey** and **Gavin Ross** from the Cavendish workshop for help and guidance in the machining of parts for the equipment which I was fabricating.

Further words of thank you to my friends and fellow band members of 13th Chime: **David Middle**, **Mick Hand** and **Rob Shaul**, the gothic punk band I am the bass player in, for their patience, understanding and support whilst I could not play the many possible gigs over the stretch of my PhD. We have still had a blast playing the USA, Russia and a few European countries and recording an album. For sharing my birthday, entertaining me and making me laugh, thank you **Roni Oppenheimer.**

Lastly I would like to thank my family, my sister **Lisa Chapman** and her family **including, Barry Chapman, Kieran Chapman,** my brother, **Matthew Rickard** and my other sister, **Kirsty Rickard.** I especially would like to thank, my daughter, **Jane Rickard** and my granddaughter, **Gracie Rickard** for their love, support, encouragement and her shouts of “Grandad”, every time she sees me.

I wouldn’t have made it without you all.

Table of Contents

List of list of illustrations

start.

polystyrene produces pillars with a hexagonal spacing pattern as this allows the minimum electrostatic pressure. The whole setup is then cooled to room temperature and the voltage removed. The top substrate is then removed revealing the pillar structures on the bottom substrate. This pillar pattern is what is predicted by the theory which shows that smaller pattern features can be made by using a thinner initial film, a smaller spacing between the electrodes or using a polymer with a lower surface tension and a stronger electric field.

Figure 3.4: Optical micrographs of a time series of electrohydrodynamic lithographic patterning of a Polystyrene film. The top electrode is a pattern of lines yielding a heterogeneous electric field. (A) The patterning begins by forming pillars between the two electrodes. (B) as time continues the pillars begin to coalesce. (C) as even more time passes the pillars coalesce even more beginning to form lines. (D) finally the pillars all coalesce to reproduce the top electrode pattern, in this case lines. Page 73

Figure 3.5: Micrographs of electrohydrodynamic patterned substrates. (A) Pattern of lines. (B) Large pillar pattern. (C) Small pillar pattern. (D) Pattern of lines which are not quite perfect also showing the area outside the top patterned substrate. Page 74

Figure 4.1: The structure of Polypyrrole Page 76

Figure 4.2: Schematic representation of electrically driven patterning set-up. (A) A thin film is liquefied and has characteristic undulations at $z=h_0$. A constant voltage, U, is applied across the electrodes. The potential difference between the substrates gives rise to an electric field, E_f that drives the flow. The dielectric of the film, ε and the gap ε^g moderate the electrical force from the applied voltage. The electrostatic force is initially balanced by the surface tension of the film, γ, giving a characteristic wavelength, λ, of the instability with viscosity η. (B) Heterogeneous top substrate directs the instability towards the protruding line structures where the electric field is strongest creating cones that reach up towards the top substrate and eventually forming pillars spanning the gap. This is followed by a coalescing of the pillars creating a positive replica of the top patterned substrate in (C) In the valleys of the top patterned substrate the film remains stable on a much longer time scale. Page 81

Figure 4.3: Schematic diagram of the solvent vapour pressure EHD setup showing the two flows of N2 gas coming in with one being diverted through a bubbler chamber to add solvent, chloroform, to the gas flow. The flow rate of each flow is controlled by a mass flow controller to control the final mixed saturation Page 82

the probe with a single 50 micron fibre which delivers the laser to the sample surrounded by five 200µm collection fibres encased by epoxy inside the metal tube. (C) A Raman spectrum of polystyrene with the Raman signal from the walls of the fibres overwhelming the signal from the polystyrene sample, making this setup unusable for Raman detection of samples.

Figure 5.8: (A) Raman collection setup with laser coming in at the top enabling position adjustment. The laser passes through a lens and then a band pass filter housed in the laser exit cone to clean up the laser signal removing any Raman signal generated in the connecting fibre. (B) Photograph of the collection fibres housed through a supporting bar which holds the fibres in position. The fibres are then held in a hole with a particular size which allows only one configuration that the fibres can be located, which is around the edge of the hole leaving a small gap for the laser beam. (C) A photograph showing the fibres organised around the edge of the hole leaving a small gap in the middle. Page 109

Figure 5.9: Photographs of: (A) of the back of the Raman collection setup showing the FC connector that plugs directly into the spectrometer. The arrow indicates the notch filter housing. (B) the modified fibre holding bar with a 300µm hole in the middle surrounded by five 300µm holes to hold the collection fibres in position and (C) top-view through the holding bar into the collection bar with five fibres going through 5 holes and a centre hole of 300µm for the laser beam. Page 111

Figure 5.10: Photographs of (A) the fibre optic arrangement with a top bar supporting the fibres coming in and allowing the laser beam through without any fibres getting in the way; (B) the fibres coming through the 300µm holes in the exit bar and also demonstrating the damaging of the outer covering of the fibres by the sharp edges of the holes and (C) the polished fibres where the five collection holes are not perfect in distance from the centre laser hole, resulting in a non-consistent collection angle. Page 112

Figure 5.11: Schematic diagram of the final Raman collection setup. The 300mW diode laser is connected to a lens tube via a fibre optic. The beam is collimated by an aspheric lens and passes through a 785nm bandpass filter. The beam is then reflected down by a dichroic mirror and through a microscope objective lens which focuses the laser beam onto the sample. The reflected light is then collected by the objective lens and the collimated beam is then reflected towards the spectrometer by a gold mirror at 45°. The beam then passes through a 785nm edge filter to block the Rayleigh and anti-Stokes signal. The beam is then Page 113

the initial film thickness combined with the patterned top substrate.

Figure 6.4: (A) Reproducible spectra of benzenethiol on RED-SERS substrates across a number of areas reveal consistent signal and substrate regularity. Insets: (i) A photograph of the gold coated RED-SERS platform with an active area at the bottom right corner. (ii) A representative SERS map overlaid on top of the corresponding optical image reveals that the SERS signal (red) comes exclusively from the RED pillars. No SERS signal is observed from the flat gold or in between the pillars. (iii) FTDT (Finite-difference time-domain) simulation shows the enhanced electromagnetic fields tightly confined on top of periodic pillar surface, maximizing the detection sensitivity. (B) Histogram of the measured electromagnetic enhancement factors of the RED-SERS substrates (*n*=17) shows a narrow distribution with an average enhancement on the scale of $8x10^9$. Page 129

Figure 6.5: Limit of detection and finger print SERS spectra of representative TBI biomarkers. RED-SERS substrates were used as an assay to perform dilutions using the specified concentration range for each biomarker. SERS spectra of **(a)** NAA and **(c)** S100B detected from 100nM to1fM concentrations at identical integration times and laser power of 10mW and the corresponding calibration curves used to calculate the limits of detection, which is three times the standard deviation of the blank divided by the gradient of the linear curve, for **(b)** NAA and **(d)** S100B obtained from the dilution experiments. Page 131

Figure 6.6: The assay was performed for each biomarker using the specified concentration range yielding calibration curves of SERS spectra acquired with an excitation laser of 785nm and a laser power of 50mW with each point representing an average of five measurements of each concentration ±STEDV used to calculate the LoD and LoQ of $1420cm^{-1}$ for the NAA, $1070cm^{-1}$ for S100B and $1150cm^{-1}$ for the GFAP. Inset: PCA score plots of PC1 and PC2 show the relationship between the multiplex spectra of the three single biomarkers. The green cluster is the NAA spectra, the purple cluster represents the S100B and the red is the GFAP. Page 132

Figure 6.7: Spiked blood with TBI-indicative biomarkers. (A). Spike-and-recovery was used for validating and assessing the MEDTech and to establish whether there is a difference between the diluent used to prepare the standard curve and the biological sample matrix. SERS spectra of the spiked blood (grey) in comparison to the normal, non-spiked blood (black). (B). 10µL of analyte was Page 135

from three time points following the sTBI applied to determine the success of the MEDTech for classifying the sTBI, EC only and HV groups at **(c)** *t*=0 **(d)** *t*=8h and **(e)** *t*=48h . The AUC indicates that the change in the NAA levels following the sTBI is a valuable marker to discriminate sTBI from the EC with the NAA showing an excellent performance with AUC=0.99 (p<0.0001) at *t*=0 and AUC=0.91 at *t*=48h post sTBI. (f-h). Box plots of the plasma NAA levels in EC group and in patients with sTBI, representing the 25^{th} and 75^{th} quarties, range and whiskers and the median (p<0.001) with normal based, two-sided 95% confidence interval of less than ±5% for each class.

Figure 6.16: Rapid, PoC MEDTech based TBI bodiagnostics **.** (A) Neurological imaging using H^1-MRI provides stratification of TBI in a hospital environment. In the early stages post TBI, the brain leaks neuro biomarkers at *miniscule* concentrations into the CSF and blood stream. A small volume of blood is collected *via* a finger prick and placed into the (B) optofluidic lab-on-a-chip for a rapid plasma separation schematically shown. (C) an optical image of the copper master used for fabrication of the PDMS along with a zoomed-in SEM image of the micro-channel filters and reservoirs of the fabricated PDMS microfluidic chip integrated with RED substrates , photographed on the right hand-side, functional with an input of 1-2 drops (10-20μL) of whole human blood (extracted by a standard pin-prick tool) to output blood plasma with an operation time on the scale of 1-2 minutes and is based on the capillary motion and comb filter separation approach. The microfluidics platform is ensuring a seamless integration of RED-SERS substrate in the fluid flow creating a thin layer of blood plasma over the SERS active substrates. Page 151

Figure 6.17: A) Initial cad designs of the microfluidic chip all with the same major flaw with the flow of the blood directly at the comb filter with the red blood cells then blocking up the filter. B) Micrograph showing the filter blocked by the red blood cells and also showing the filter had not sealed properly allowing some red blood cells through. Page 152

Figure 6.18: Cad drawing of the final microfluidic chip showing blood inlet, capillary flow main channel, filter combs, SERS substrate area, flow snake to allow longer times of flow and waste collection area. Page 153

Figure 6.19: (A) Micrograph of filter combs within microfluidic chip prior to blood insertion, the main capillary channel is visible on the right hand side with 2 sets of Page 154

filter combs branching off to the side and connected to the RED-SERS substrate collection area. (B) Micrograph of microfluidic chip once a drop of blood has been introduced into the inlet box, the plasma and red blood cells are clearly visible in the main capillary channel with plasma clearly visible in the filter combs and in the RED-SERS collection boxes with 100% filtering out of the red blood cells. It can be seen in the bottom filter comb that some of the filters were blocked and never allowed plasma through but with several filter combs per collection area enough plasma is allowed through to the collection boxes.

Figure 7.1: Methodology for optimization of a RED substrate for SERS detection of up to *N* biomarkers (BM). Multiplex, ideally under a single excitation wavelength and specificity for the quantification of each target biomolecule are required. This methodology is further used for tailoring the SERS substrate to the target biomarkers (BMs) and defining the required active regions (AR) on the substrate, as a function of multiple surface functionalization, where further required.

List of Tables

Abbreviations

CT	Computerized Tomography
DNA	Deoxyribonucleic acid
DW	Deionized Water
EBL	Electron Beam Lithography
EBL	Electron Beam Lithography
EC	Extra-cranial
EF	Enhancement Factor
EHD	Electrohydrodynamic Patterning
EHL	Electrohydrodynamic Lithography
FET	Field Effect Transistor
FIB	Focussed Ion Beam
FTDT	Finite-difference time-domain
GFAP	Glial-Astrofibrillary Protein
GH	Golden Hour
HV	Healthy Volunteer
IBL	Ion Beam Lithography
LED	Light Emitting Diode
LoQ	Limit of Quantification
MEDTech	Micro-Engineered Device Technology
MRI	Magnetic Resonance Imaging
MSA	Molecular Self-Assembly
NA	Numerical Aperture
NAA	N-acetylasparate
NAO	National Audit Office
NSE	Neuron-Specific Enolase
OLED	Organic Light Emitting Diode

PDMS	Polydimethylsiloxane
PoC	Point of Care
PPy	Polypyrrole
PS	Polystyrene
PTFE	Polytetrafluoroethylene
RED	Reproducible Electrohydrodynamically
ROC	Receiver Operating Characteristic
SCD	Spray Carbon Dioxide
SEM	Scanning Electron Microscope
SERS	Surface Enhanced Raman surfaces
sTBi	Severe Traumatic Brain Injury
STM	Scanning Tunnelling Microscope
TBI	Traumatic Brain Injury
TEM	Transmission Electron Microscope
UV	Ultra Violet
VTE	Vacuum Thermal Evaporation

List of Publications

1. **Rickard J.J.S.,** Farrer I., Goldberg Oppenheimer P. **Tunable Nanopatterning of Conductive Polymers via Electrohydrodynamic Lithography**. *ACS Nano*, **2016**, 10, 3865-3870
2. Busà, C., **Rickard, J.J.S.,** Chun, E., Chong, Y., Navaratnam, V., Goldberg Oppenheimer, P., **Tunable Superapolar Lotus-to-Rose Hierarchical Nanosurfaces via Vertical Carbon Nanotubes Driven Electrohydrodynamic Lithography.** *Nanoscale*, **2017**, 9, 1625 – 1636
3. **Rickard J.J.S.,** Farrer I., Goldberg Oppenheimer P. **Tunable Nanopatterning of Conductive Polymers via Electrohydrodynamic Lithography**. *ACS Nano*, **2016**, 10, 3865-3870
4. **Rickard J.J.S.,** Goldberg Oppenheimer P. **Advanced Lithographic Micro Surfaces for Biodiagnostics** *Nano-World Magazine*, **2016**, 3

Patent Pending

Surface Enhanced Raman Scattering Apparatus and Method. Goldberg Oppenheimer, P., Rickard, J. J. S., Di-Pietro, V., Belli, A. Patent Pending, 1701182.6, 2017

CHAPTER 1

Introduction

Upon our first glance at the world we see plants, animals, people, buildings and all manner of objects made from many different materials. When we take a closer look using a microscope, we find that many of these have intricate micron and nanometre scale patterns. These patterned microstructures lead to many amazing and unique properties such as the iridescent colours of butterfly wings, through to the hierarchical structure on the feet of geckos and the superhydrophobicity of the Lotus flower leaf (Figure. 1.1.).

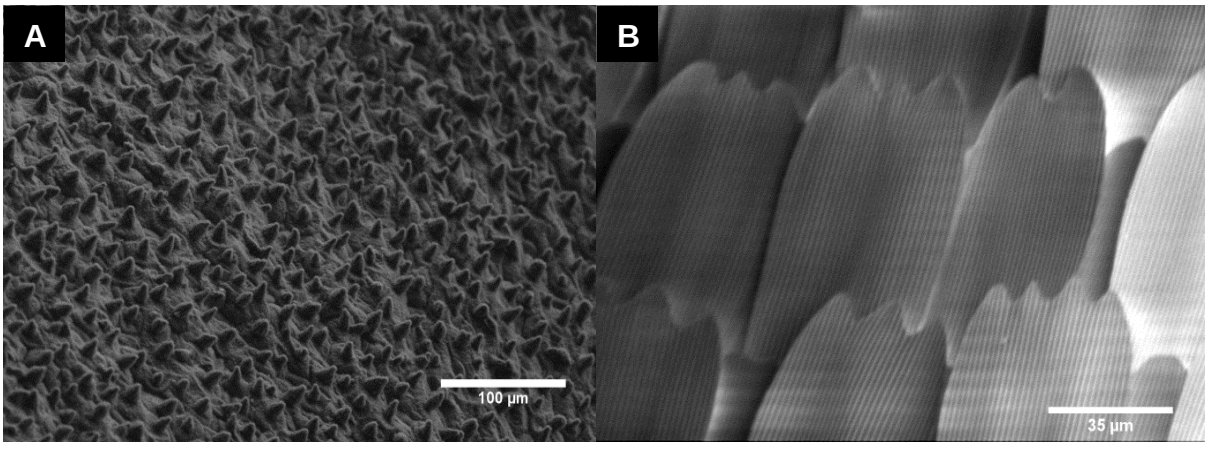

Figure 1.1: (A) SEM image of a lotus leaf showing cone structures along with fine nano-hairs that render it superhydrophobic taken using an Hitachi s3400 microscope. (B) A zoomed-in SEM micrograph of the uncoated insulating scales from the wing of a butterfly showing the microstructure, taken using an FEI Helios Microscope.

If we can replicate or enhance these naturally occurring micro and nano structures, this will then allow us to exploit their unique properties to our advantage and to further fabricate novel and advanced miniaturised devices, inspired by nature. In this work we wanted to produce vertical field effect transistors from a conductive polymer to create a higher density of transistors using a cheap and facile method, compared to the current silicon technologies. In conjunction we also wanted to create a test for traumatic brain injury using biomarkers that could be done in less than 5 minutes at the scene of a road traffic accident, on the sports field or at a hospital, at the point of care, POC, with the aim of the test being cheap and quick compared to the current gold standard of magnetic resonance imaging, MRI, which can only be done at a hospital using a very expensive machine. We created micro and nano structures using electrohydrodynamic patterning, EHD, to create these novel devices. In this chapter we look at different lithographic methods that can be used to produce micro and nano structures that we require to produce our structures and devices. We also look at Field effect transistors and how they work and were invented. In particular we examine polymer FETs and vertical FETs to show what has been achieved so far. We also look at Raman and surfaced enhanced Raman as this is the detection technique we use for the detection of traumatic brain injury biomarkers. There is a broad range of lithographic methods which have been developed in the past few decades for fabricating small patterned devices [3] such as for instance, photo lithography [4], electron beam lithography (EBL) [5], LIGA (***Li****thographie,* ***G****alvanoformung,* ***A****bformung*) [6] focused ion beam patterning (FIB) [7], a range of imprinting methods and a somewhat less conventional technique, known as

electrohydrodynamic patterning (EHD) [8]. However, each of the many existing patterning methods have certain advantages and disadvantages.

1.1 Lithographic Methods – State of the Art

1.1.1 Photolithography

Photolithography uses light projected through a patterned mask onto a substrate covered with a light sensitive film, *i.e.,* photoresist, which is then developed leaving the pattern, or the negative of the pattern, on the surface of the substrate [9],[10].

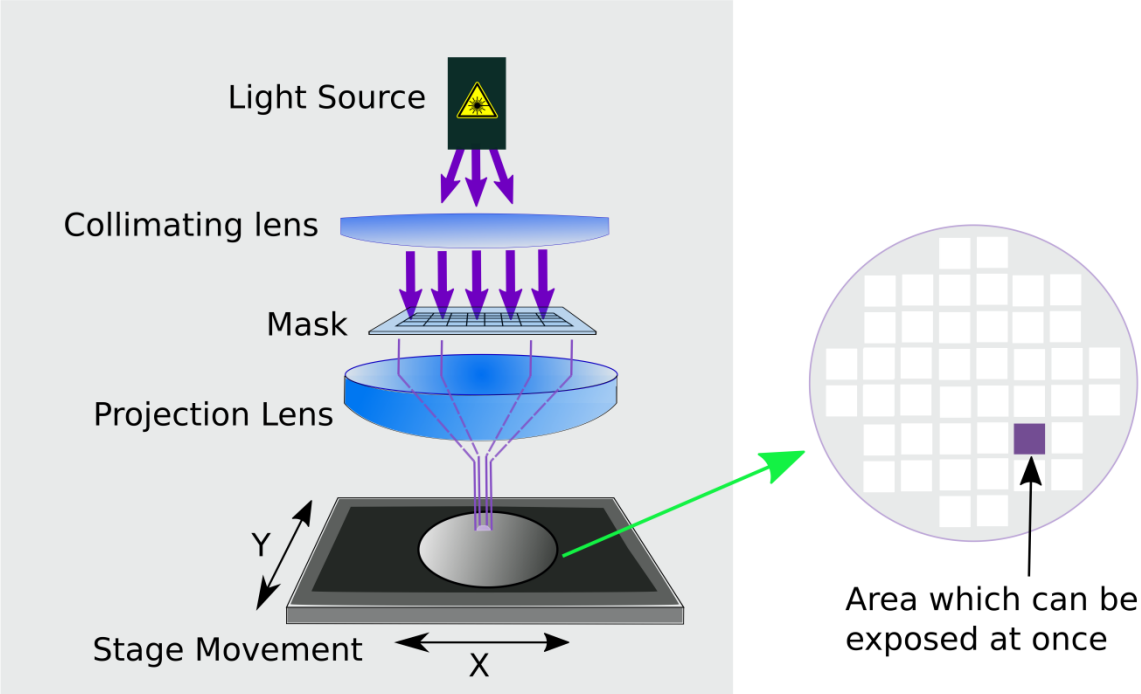

Figure 1.2: Schematic representation of a typical semiconductor photolithography setup showing a source of light collimated by a condenser lens which is projected through a photomask and focused onto the substrate by a projection lens reducing the size of the mask image by roughly four times. The substrate is then stepped to the next position allowing a large area to be exposed with a high resolution.

The simplest form of photolithography is to place the mask in contact directly on top of the resist. However, while this yields high resolution, any particles on the photoresist can be transferred to the mask and thus damage it. Therefore a better approach is to use a projected image of the mask onto the resist [10]. This has several advantages as the mask will not be contaminated and damaged by any contact with the resist and the projected image can be reduced in size compared to the original mask by the projection lens. The projected image of the mask can be projected to more than 8 times smaller on the substrate than the size of the structures on the mask [11] (Figure 1.2.). This makes mask production much easier as the mask structure sizes can be larger than would be required for contact lithography to achieve the same size structures. The photoresist can be either positive, thus leaving the image of the mask on the substrate, or negative, leaving the inverse of the mask on the substrate, depending on what is required. Currently, photolithography is the most common method used by the semiconductor industry to produce most microelectronic devices.

Resolution is defined as the ability to resolve, or separate, two points of an object. The theoretical resolution of a projection photolithography system,r, is limited by the Rayleigh criterion of the projection optics and equals the wavelength of the light, λ, multiplied by an experimental limiting factor, K which is typically between 0.5 and 1 and depends upon processing conditions and the photoresist used and its thickness, divided by the numerical aperture of the system [12] Equation [1.1].

$$r = \frac{K\ \lambda}{NA} \qquad [1.1]$$

The numerical aperture (NA) relates to the angles of the light that can be accepted or emitted from the optic system. This is given by the equation [1.2] where, NA equals the refractive index of the material the optic system is in, n, multiplied by the *sin* of the angle θ, which is the maximum half angle of the cone of light that can enter the lens Equation [1.2].

$$NA = n \sin \theta \quad [1.2]$$

In a typical photolithography setup the resolution is limited by the wavelength of the light used and the refractive index of the medium between the lens and the object to be imaged. The most common wavelengths of light used in modern high resolution semiconductor fabrication plants are the deep ultraviolet excimer lasers at 248nm and 193nm ultra violet light [13]. Until 2007 the Intel corporation used air as the medium between the lens and the substrate, however, to improve the resolution they have introduced immersion photolithography to produce even smaller nodes which they patented in 2002 [14]. By using a medium other than air between the lens and the substrate, it was possible to increase the refractive index, thus, increasing the numerical aperture. Therefore, to increase the resolution, the semiconductor industry uses pure water to fill the distance between the lens and the substrate giving a numerical aperture of 1.44 but only giving 1.2 for full field scanners [15] and therefore, achieving structures down to less than 32nm [16] .

1.1.2 Electron Beam Lithography

Electron Beam lithography (EBL) enables higher resolution than optical photolithography to be achieved [17]. EBL uses a focused beam of electrons scanned

over a substrate to expose an electron sensitive resist coating the substrate which is subsequently developed, using a solvent, to either leave a positive or negative image on the substrate (Figure 1.3). Another advantage of EBL is that it does not require a mask since the beam can be directly controlled from a computer aided design (CAD) system.

Figure 1.3: A photograph of a representative Raith Nanofabrication EBPG5200 electron beam lithography set-up.

Since, the wavelength of electrons accelerated to 50kV is 0.0055nm, which is substantially smaller than the size of an atom, which is roughly 0.1nm, therefore hypothetically it should be possible to pattern down to an atomic scale using EBL. Unfortunately however, due to the aberrations of electron lenses along with the interactions of the electrons with the resist mean, that at the present moment, the smallest that can be achieved are features down to 5nm in size [18]. Moreover, EBL is a slow and cumbersome process and therefore is predominantly used to fabricate the high resolution masks for photolithography applications.

1.1.3 LIGA (*Lithographie, Galvanoformung, Abformung)*

LIGA is a German acronym that stands for ***Li**thographie, **G**alvanoformung, **A**bformung* (Lithography, Electroplating, and Molding). This is a lithography technique that can create high aspect ratio structures, taller structures than the width, down to the sub-micron scale. It was first developed to produce separation-nozzle systems for uranium enrichment by E. W. Backer and a team at Institut für Kernverfahrenstechnik des KernforschungszentrumsKarlsruhe in 1982.

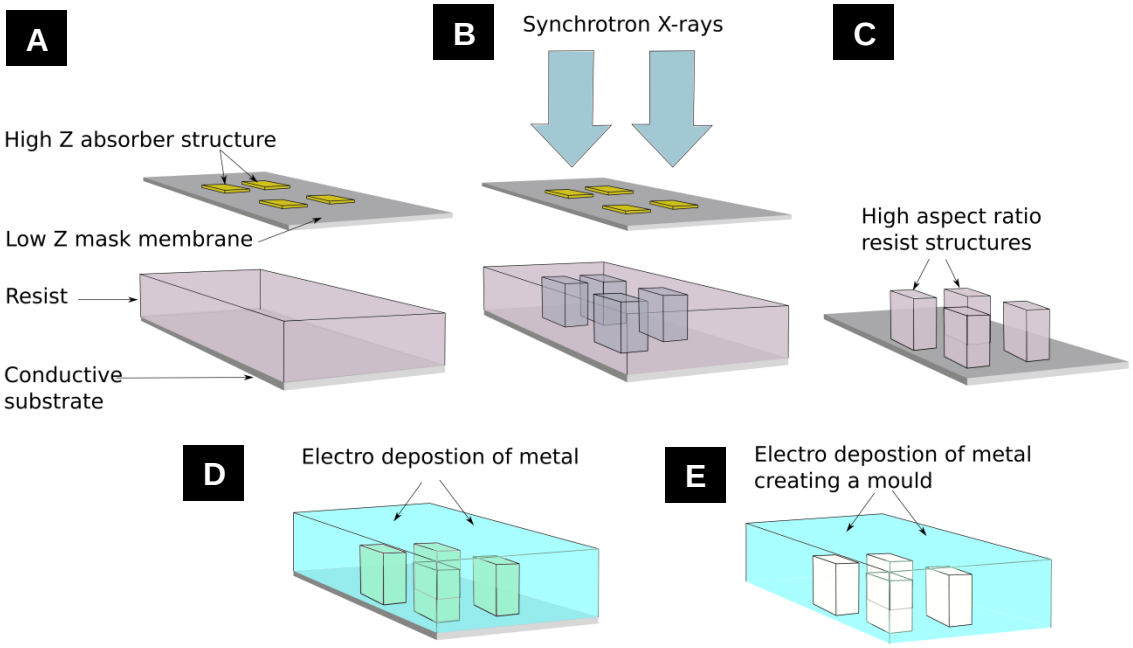

Figure 1.4: Schematic diagram of X-ray LIGA process . A) A Low Z membrane mask is covered with a high Z X-ray absorber material in the shape of the required pattern. A substrate is coated with a thick layer of photoresist, either spun coated or cast. B) Synchrotron radiation is shone through the mask and some is blocked by the high Z material with the rest exposing the resist not protected by the high Z material. C) The resist is then chemically developed, either leaving or removing the exposed resist depending on whether the resist is positive or negative, in the pattern of the mask, leaving structures with a high aspect ratio on the substrate. D) The resist structures are covered by electro plating. E) The electroplated structures are removed from the substrate and the resist is removed by chemical solvent leaving a mould ready to cast many devices.

There are two types of LIGA, X-ray and UV. X-ray LIGA has a better resolution but requires a very expensive synchrotron radiation source. UV LIGA is much cheaper as the mask can be a much simpler chrome mask rather than the expensive masks required for X-ray LIGA but the UV system has less resolution with lower aspect ratio structures than X-ray LIGA. X-ray LIGA (Figure 1.4) uses synchrotron generated X-rays that are passed through a mask that uses a low Z material substrate, usually made of graphite or glassy vitreous carbon, that allows the X-rays through and beam stopping patterns on the substrate made of a high Z material, X-ray absorbing material, usually gold, lead or nickel. This patterning is usually made using electron beam lithography which adds to the cost of production. The X-rays pass through the low Z parts of the mask onto a substrate coated in a layer of X-ray sensitive photoresist. The photoresist has to be applied in thick layers and must be free from stress, typically PMMA is used. The resist is then chemically developed removing the unexposed or exposed resist, depending on what is required, leaving a high aspect ratio pattern, higher structures compared to the width of the structures. Electrodeposition of a metal is then used to coat the structures with a thick layer of metal. The metal and remaining resist is then peeled off the substrate. The remaining resist is chemically removed leaving a three dimensional metal mould. This mould can then be used in injection moulding to produce the required devices many times. UV LIGA uses a cheaper source of ultra violet electromagnetic radiation than X-ray LIGA with a much simpler mask, such as a chrome on glass mask, and using a polymer positive or negative photoresist. The resolution is reduced compared to X-ray LIGA and with lower aspect ratios achievable so is used when costs must be kept low.

1.1.4 Focused Ion Beam Lithography

Focussed ion beams were first generated in 1975 by W. Escovitz, T. Fox and R. Levi-Setti [19], who produced a gas field ionization source using hydrogen which they used to image unstained, critical point dried biological specimens in a transmission mode. The researchers produced an image of a chromosome with a sub-micron resolution, revealing the great potential of focussed ion beam. However, since these gas ion beams were of a low current and thus, yielding low signal, it took several minutes to capture an image. In 1978 R. Seliger *et* al*.* successfully generated a high current, of 3000nA, liquid metal ion source using gallium [20], producing a spot size of 100nm, focused on the sample. More excitingly, they used a gallium ion beam to machine lines into a gold film down to a width of 100nm, opening up the possibility of nanofabrication of structures with many potential applications.

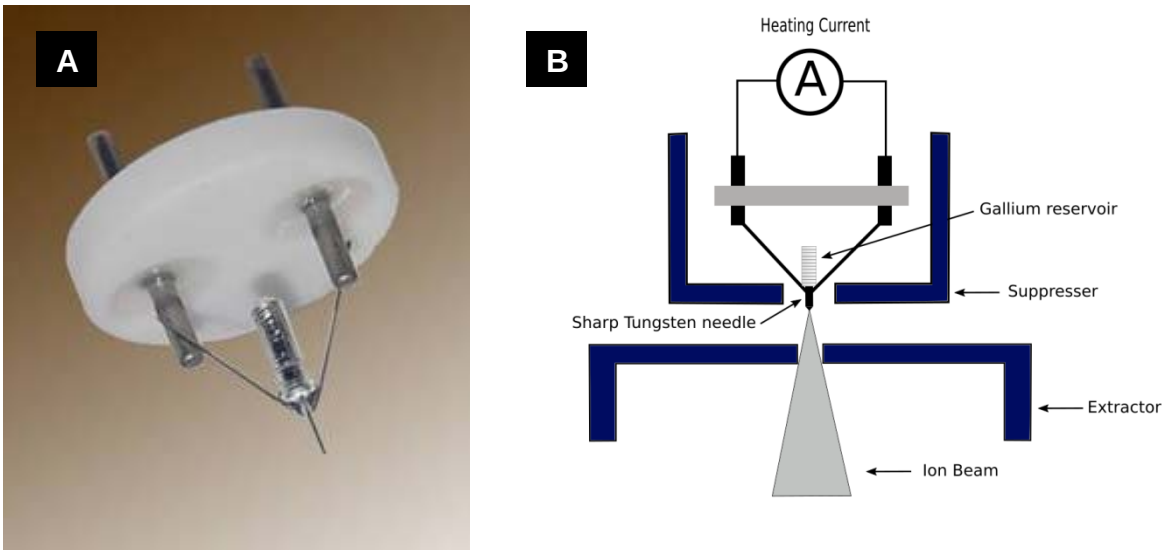

Figure 1.5: (A) Photograph of a liquid metal ion source produced by Raintree Scientific Instruments Corporation showing the reservoir of gallium attached to the back of the sharp tungsten needle. (B) Schematic diagram of liquid metal ion source layout.

Ions have been produced with liquid-metal ion sources from a broad range of elements including, Al, Au, B, Be, Cu, Ge, Fe, In, Bi, As, Li, P, Pb, Pd, Cs, Si, Sn, and Zn, yet the most popular source has been gallium [21]. The liquid metal ion source is produced by wetting of a sharp tungsten needle, with a radius of roughly 100nm, by the desired metal to be ionized (Figure 1.5). This is achieved by heating a reservoir of the metal attached to the back of the needle, *via* a capillary action and gravity, thus coating the needle with liquid metal. A negative bias is applied to a cathode, known as *the extractor*, creating a high electric field at the tip, where the liquid metal forms an atomically sharp cone which in turn, creates a high enough field for the ions to tunnel out. A high voltage, applied to a second cathode, is then used to accelerate the ions to the desired accelerating voltage. The beam of ions is controlled using current limiting apertures and a series of electrostatic deflectors and octopoles which focus the beam to a spot and scan it over the sample. By controlling

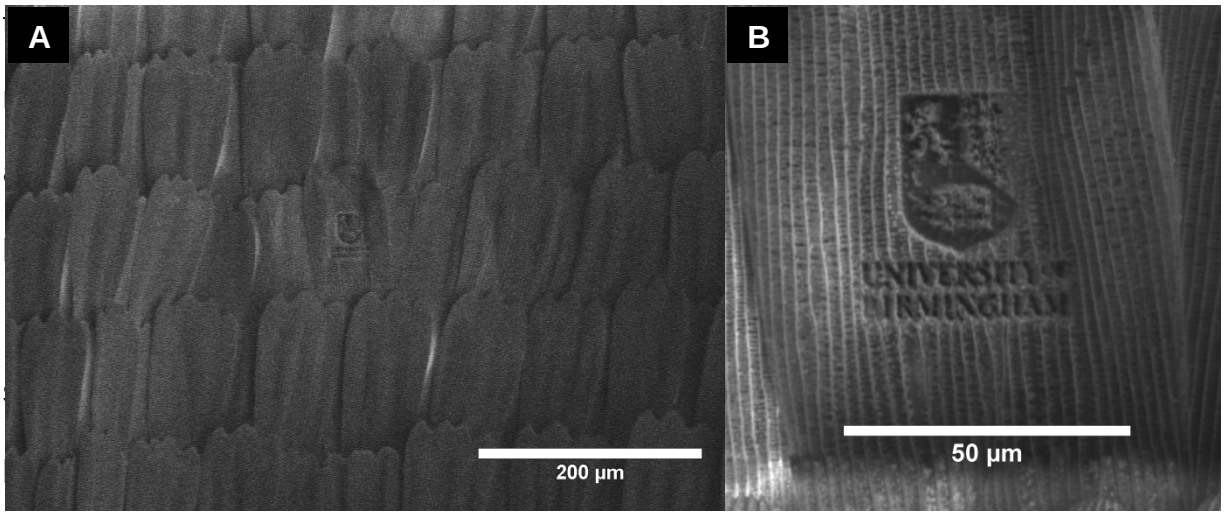

Figure 1.6: (A) An SEM image of a butterfly wing showing the scales with a University of Birmingham crest (centre of the image) which has been focussed ion beam milled into a single scale using an FEI Helios Nanolab 650 scanning electron and ion beam microscope with a built in lithography patterning system which is capable of producing very fine and detailed nano patterns into any material (B) Zoomed-in SEM image of the University of Birmingham crest showing the fine details and even more, the cross member structures within the butterfly wing scale, which is an insulator and is uncoated.

Any material can be patterned using IBL, even insulating substrates which can either be coated with a thin conducting layer or by using a flood gun of low energy electrons to negate any charge build-up. IBL can produce patterns down to 3 or 4nm and with new sources of ions being produced, *e.g.,* helium, it may be possible to go down to 1 or 2 nm patterning resolution [23]. Currently, IBL is a very time consuming technique and requires well trained personnel, yet, in the future it might possibly be accelerated by exploiting multiple beams, used simultaneously.

1.1.5 Molecular Self Assembly

An additional method to create patterned structures is to use molecular self-assembly (MSA) which is the spontaneous assembly of molecules into stable structures [24] [25] (Figure 1.7).

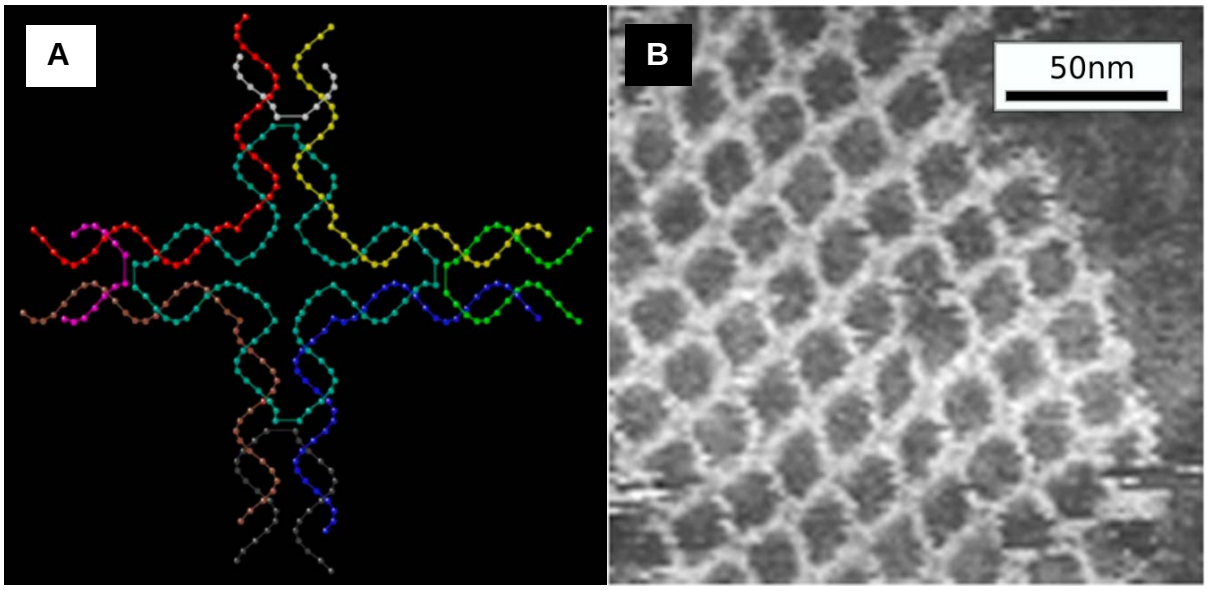

Figure 1.7: Molecular self-assembly of DNA Nanostructures (A) DNA "tile" structure consisting of four branched junctions oriented at 90° intervals. These tiles serve as the primary "building block" for the assembly of the DNA nanogrids shown in (B). Each tile consists of nine DNA oligonucleotides as shown. (B) An atomic force microscope image of a self-assembled DNA nanogrid. Individual DNA tiles self-assemble into a highly ordered periodic two-dimensional DNA nanogrid, Adopted from [22].

Nature uses MSA to create structures from lipid membranes for cells to collagen fibres for skin [26] [27]. Controlling molecular self-assembly is difficult nevertheless, many research groups around the world are working on this type of patterning to generate a range of functional devices including for instance, creating solar cells using small self-assembled molecules [28] or using DNA origami to create nano patterned surfaces [29].

1.1.6 Nanoimprint Lithography

A simple yet, a high resolution technique known as nanoimprinting can also be used to make nano-patterns [30] (Figure 1.8).

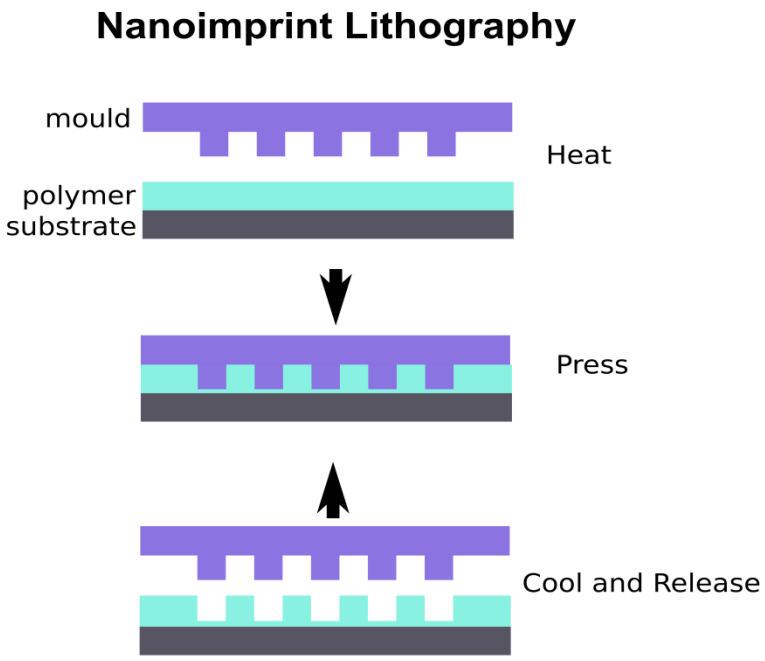

Figure 1.8: Schematic diagram of the Nanoimprint lithography process. The substrate is covered in a layer of polymer that is heated until the polymer is soft. The mould is then pressed into the softened polymer. The whole setup is then cooled well below the glass transition temperature of the polymer and the mould is then removed, leaving a negative image of the mould in the polymer.

In the nanoimprinting process, a thin layer of a thermoplastic is spun onto a substrate and subsequently heated above its glass transition temperature until it has softened. A patterned mould is then pressed into the thermoplastic and the whole setup is cooled down, freezing the formed pattern within the initial resist. The mould is finally removed, leaving an imprinted pattern on the substrate. The substrate can further be etched using a reactive ion etch to remove the parts not covered by the patterned thermoplastic. While nanoimprinting enables fabrication and reproduction of small, sub-micron structures, down to 10nm, it is limited by deformation issues as the mould is pressed into and removed from the thermoplastic and edge sharpness as wear happens [30]. In addition, the imprinting is limited by the quality of the mould which is typically pre-fabricated *via* another technique.

1.1.7 Electrohydrodynamic Lithography

Recently, a novel lithographic method has been developed and optimised in our group known as electrohydrodynamic lithography (EHL) for fabricating tuneable micro and nano sized patterned surfaces from a broad range of materials [31 32].

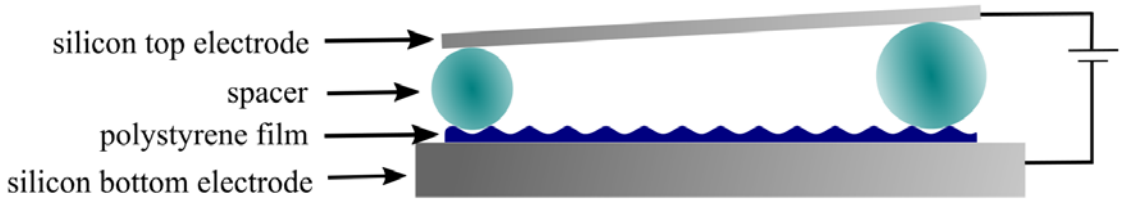

Figure 1.9: Schematic diagram showing the capacitive device setup for EHD. The setup consists of a conductive bottom electrode covered by a thin polymer film. Spacers then create an air gap between the top conductive electrode, which can be planar or patterned, and the polymer film. A bias is applied between the two electrode to create an electric field

assembling a capacitive device setup (Figure 1.9). A conductive substrate, usually made of silicon but in theory can be any material that is conductive or an insulator coated with a conductive layer, used as a bottom electrode in a capacitor device, is coated with a thin layer of material to be patterned. A top conductive electrode, which can be either structured or planar, is placed above the original substrate with a small, nanoscale gap in between. A bias is applied between the two substrates and the whole setup is heated above the glass transition temperature of the material to be patterned. Due to the electrostatic pressure build-up at the dielectric interface between the patterned material and an air gap, a replication of the patterned top electrode is accomplished. If a planar top substrate is used, pillars with a hexagonally spaced symmetry layout are generated since the micro-capacitor like set-up tends to minimize the electrostatic pressure (Figure 1.10).

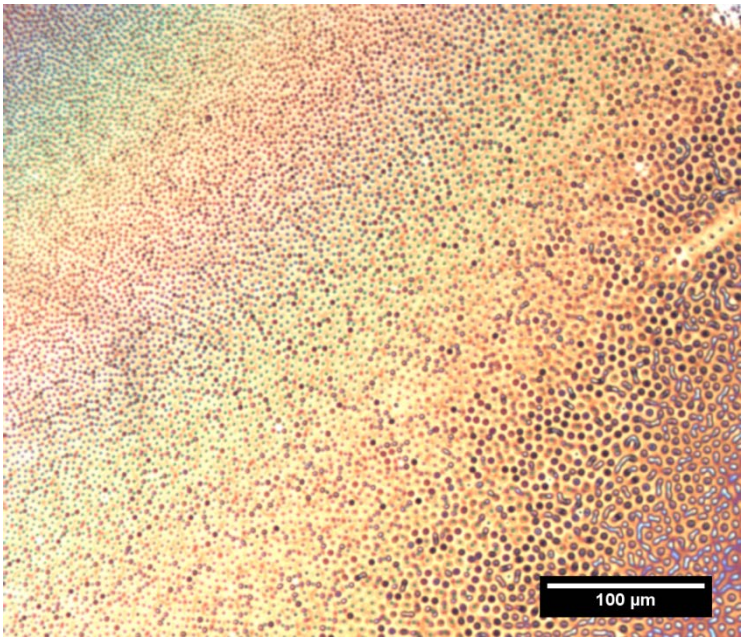

Figure 1.10: An optical microscopy image of the electrohydrodynamically produced polystyrene pillars. Early stage instabilities can be seen in the bottom right hand side of the image with pillars of different sizes showing different colours in the top left of the image.

Once the EHL patterning process is complete, the whole device is cooled below the glass transition temperature of the patterned material, quenching the pattern in place, before the top substrate is removed. EHL enables fabrication of patterns down to tens of nanometres. However, it is still limited by the overall size of the patterned area that can be accomplished. The above described patterning methods have opened new avenues for a range of advanced and innovative devices being continuously fabricated to meet the challenges of the 21st century, for a variety of applications including, environmental [33], healthcare [34, 35], communications and computing [36].

In this work, by exploiting and optimising the EHL method, we show design and engineering of further novel, miniaturised devices tackling some of the major challenges in the fields of point of care (PoC) and field effect transistors (FETs). In chapter 4 we will discuss the challenge of making vertically aligned FETs and meeting that challenge using leaky dielectric EHL. Secondly we will show using EHL how to create Surface Enhanced Raman surfaces (SERS) and to use them to diagnose traumatic brain injury at point of care in a timely way.

1.2 Field Effect Transistors

Field effect transistors were originally proposed and patented in 1930 by J.E. Lilenfeld [37]. Although Lilenfeld patented the FET, only in 1947 did William Shockley and his group at Bell Labs fabricate the first working FET for which he and his team received the Nobel prize in 1956 (Figure 1.11). A FET uses an electric field to control the conductivity path between a source and a drain through a semiconductor

1.2.1 Background of Polymer Based Field Effect Transistors

Since their invention, FETs have been mainly made of doped silicon, however in the last thirty years there has been considerable interest in using conducting polymers to produce FETs. Polymer FETs have some advantages over traditional silicon based transistors in that they can be flexible unlike silicon and also can be cheap to make and process, using less energy to manufacture. The first polymer based FET was developed in 1987 [38].

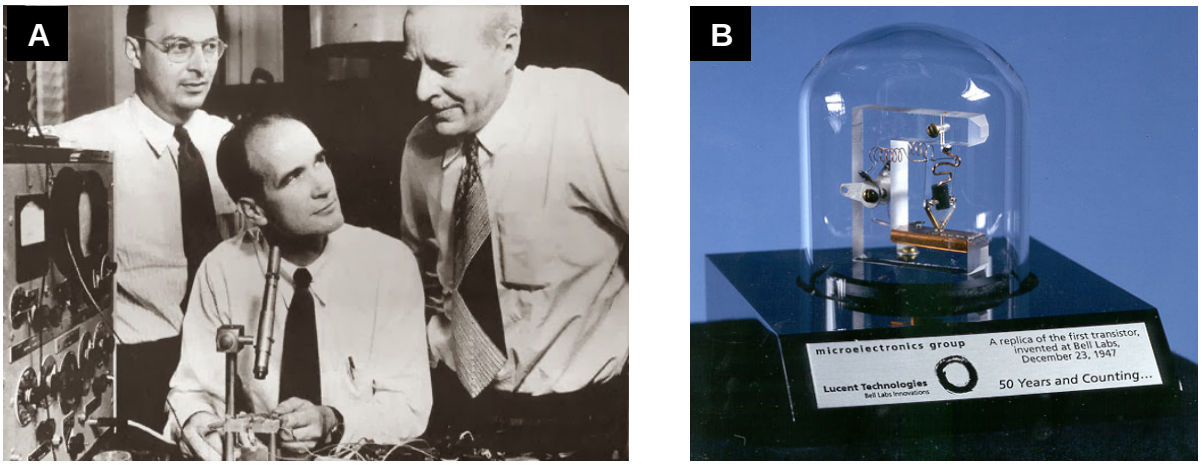

Figure 1.11: (A) John Bardeen, Walter Brattain, William Shockley, the co-inventors of the first working FET. (B) A photograph of a replica of the first working FET. [1]

While it still used silicon, gold and gallium and therefore not entirely made of only polymer, it did show that polymers could be used in a FET. Only in 2007 was it shown that the performance of single conducting polymer nanowires can have comparable performance to silicon nanowire based FETs [39]. Furthermore, it was shown to be possible to assemble several wires on one substrate, which showed a

great promise for multiple transistor devices, yet considerable work still needs to be done to accomplish this intricate task accurately and repeatedly [40]. In 2006 it was further demonstrated that it is possible to make polypyrrole thin film transistors and combine this with conventional silicon processing to produce a device that was shown to work as an oxygen detector, thus fabricating a Schottky barrier-type field-effect transistor [41]. Furthermore, an all polymer FET was fabricated including a flexible polymer substrate by Lee *et* al. [42]. These FETs were fabricated using photolithography at room temperature and it was claimed that the transistors are transparent and mechanically flexible, although the conduction parts were rather dark. It also proved difficult to achieve high resolution, nevertheless a line width of 5μm was produced. In 2007, by using thin films and an embossing technique, FETs on a sub-micron scale were produced, with a 700nm thickness of the spin coated insulating inkjet printed layers [43]. These gates were vertical which yielded a considerably higher packing density than traditional horizontal layer FETs. One of the major flaws of polymer based FETs though was that they are not highly robust and easily damaged. However, in 2014, it was shown that it is possible to create polymer FETs that were stable in hostile environments and could be used as sensors, even in sea water [44]. Another weakness of the polymer FETs is a low current limit, nevertheless It was later shown that it is possible to make high current high density vertical FETs that use low voltage [45], although it did involve major silicon lithography processing, diminishing the value and advantage of using conducting polymers. FETs using a polyaniline nanowire and an electrolytic solution as the gate have also been produced, however, it was found that such FETs were not stable, most

probably due to the usage of hydrochloric acid and sodium chloride electrolyte which may have directly affected the integrity of the nanowire [46].

In chapter 4 we will demonstrate and discuss a novel route for fabricating vertical field effect transistors using a leaky dielectric on a sub-micron scale using an optimized EHL fabrication method.

1.3 Raman and Surface Enhanced Raman Scattering (SERS) Based Point-of-Care Diagnostics

1.3.1 From Raman to SERS

As we wish to produce a device to detect traumatic brain injury biomarkers using surface enhanced Raman we need to look at what Raman is and what surface enhanced Raman is. Electromagnetic radiation is comprised of both waves and photons which have oscillations of electric and magnetic fields, perpendicular to each other, propagating at 299,792,458 metres per second through a vacuum [47]. Visible light is an electromagnetic radiation within a certain part of the electromagnetic spectrum with a wavelength between 400nm to 700nm [47]. Shining light upon molecules results in most of it being elastically scattered and while its direction of travel changes, its frequency remains the same, also known as *Rayleigh* scattering, named after Lord Rayleigh who discovered the effect [48]. However, a very small portion of roughly 1 in 10 million, of the photons of light, interact with the molecules or

atoms either gaining or losing some energy, inelastically scattered and therefore, changing the frequency of those photons. This effect was discovered by C.V. Raman and K.S. Krishnan in 1928 and also separately by G. Landsberg and L. Mandelstam in 1928 (Figure 1.12). But as Raman and Krishnan published first this inelastic scattering is called the Raman effect with C.V. Raman receiving the Nobel prize in 1930 for his work on scattered light phenomena [49].

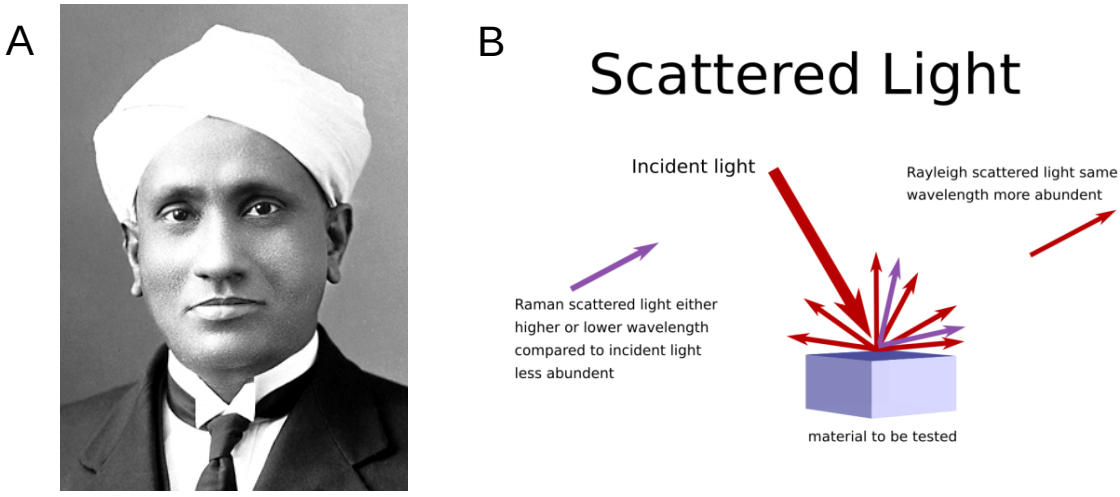

Figure 1.12: (A) Dr. Chandrasekhara Venkata Raman Nobel prize winner 1930 for his work on the scattering of light and for the discovery of the effect named after him. (B) Schematic diagram of light being scattered by a material with the majority of the light being scattered at the same frequency as the incident light, Rayleigh scattered, and a very small proportion being Raman scattered at a different frequency to the incident light.

Raman spectroscopy uses a monochromatic light source, typically from a laser, where photons of light are incident upon a certain material and excite vibrational modes of the molecules. Most of the photons are scattered with the same frequency as they started with, Rayleigh elastic scattering. However, a certain proportion of the photons of light release or receive some energy from the molecules that they interact with, *i.e.,* inelastic scattering, resulting in *Raman* scattering. The amount of Raman

scattering depends on the polarizability of the electron cloud of the molecule, which is the ability of the oscillating electric field of the photons of monochromatic laser light to induce a dipole moment in the electron cloud of the molecule. The bonds in molecules can stretch, rotate, twist and bend. The molecular bond energy levels are quantised thus, the Raman scattering frequency changes in discrete steps. Therefore, if the Raman light is collected in a spectrometer, which by using a grating spreads out the different frequencies of light onto a detector, the collected spectrum will give discreet peaks, known as lines, that identify which bonds are present and in this way, recognise the molecule the light has been scattered from. If the scattered emitted photons have lost energy compared to the incident light, known as 'Stokes' shifted, named after Sir George Stokes, who in 1852 published a paper on fluorescence about the changing frequency of ultra violet light into visible wavelengths by uranium glass [50], and if the photons have gained energy, they are 'Anti-Stokes' shifted [51].

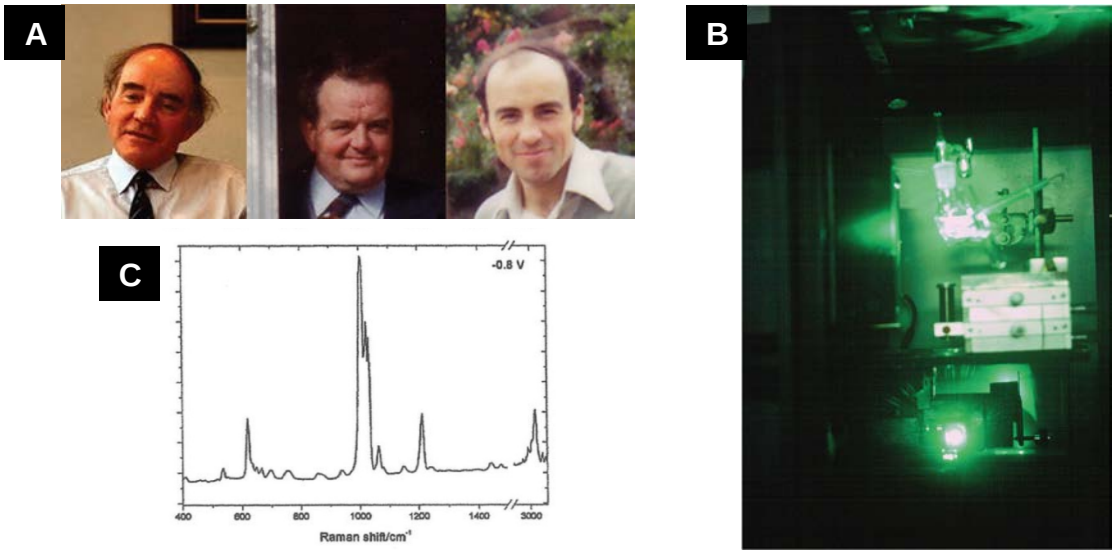

Figure 1.13: (A) Martin Fleischmann, Pat Hendra and Jim McQuillan (B) Photograph of the Raman spectroelectrochemistry cell(C) Surface-enhanced Raman spectra recorded at different potentials on a roughened silver electrode using an electrochemical Raman [2]

Surface enhanced Raman spectroscopy was first observed by Martin Fleischmann, Patrick Hendra and James McQuillan at the University of Southampton in 1973 (Figure 1.13), who noticed that the Raman spectrum of pyridine on a roughened silver surface had a much higher value than would be expected. The researchers assumed that the enhancement was due to a larger surface area [52]. However, in 1977 two competing explanations of the enhancement phenomena were proposed showing that it was not due to a larger surface area but because of a true enhancement of the Raman scattering. When a molecule is adsorbed or, very close to a metallic surface, a large enhancement of the Raman bands is observed. The first explanation is the chemical theory proposed by Grant Albrecht and Alan Creighton [53] suggesting the formation of charge-transfer complexes, which only happen for molecules that have formed a chemical bond with the surface of the noble metal. However, this does not explain the observed signal enhancement for molecules at a distance. These distant enhancements can be explained by the second model, the electromagnetic theory, as proposed by David Jeanmaire and Richard van Duyne [54]. When the photons of light from the monochromatic light source hit the surface of the noble metal they excite surface Plasmons which, in turn, enhance the electric field of the photons. Plasmons can be thought of as a quantized oscillation of the electron density with respect to the fixed positive ions in a metal. The enhancement is the greatest when the wavelength of the incident photons is in resonance with the plasmon frequency. The enhancement can be 10^{14} or even higher of the level of the Raman signal, which corresponds down to a single molecule detection level [55]. However, in reality, SERS spectra are a result of multiple contributions such as physisorption, chemisorption and substrate excitations, electron–hole pairs and

surface plasmons, which are all involved in the SERS phenomena, thus making a high degree of complexity to determine which part gives what enhancement [56]. It is widely accepted though that SERS is an enhancement of the electromagnetic field of a small metal particle or surface, giving a high dipolar resonance surface plasmon, enhancing the Raman scattering. The field enhancement can scale as high as E^4, where E is the local optical field [56]. SERS substrates are most commonly made of nano particles of gold or silver noble metals in the size range of a few nanometres to a few hundred nanometres [57] [58]. These substrates or liquid suspensions of nanoparticles do have a drawback as they work by creating plasmon enhancing local points, known as 'hot spots', which are created when the particles come close together or touch each other. One of the biggest drawbacks of such hotspots is their irreproducibility, as it is impossible to create exactly the same size particles with the same crystal orientation and the same touching points from batch to batch, leading to inconsistent results [59].

1.3.2 Background History of using Raman and SERS for Analysing Human Blood

We use human blood to detect biomarkers from traumatic brain injury using SERS to determine if a patient has traumatic brain injury as we show in chapter 6. The history of using Raman and SERS to investigate biomarkers and disease starts in 1974 when a landmark paper was published by K. Larsson and L. Hellgren from the University of Göteborg, "*A study of the combined Raman and fluorescence scattering from human blood*" [60]. This paper showed the potential of Raman

spectroscopy to be used to investigate blood plasma to determine diseases. The researchers have compared blood from patients with Iues, erysipelas, mycosis fungoides, viral hepatitis, sepsis, leukaemia and advanced carcinoma with blood from healthy people and saw noticeable differences. While this indicated that Raman spectroscopy could be potentially used to diagnose diseases, the equipment and technology of the time were very expensive, had low sensitivity, slow and difficult to use. In 1988, a paper showing oxygen uptake by red blood cells in patients with rheumatoid arthritis using resonance Raman was published [61] showing that there were significant differences in blood oxygenation levels from joints with rheumatoid arthritis and joints of people without arthritis. They looked at how the oxygen is bound to the iron in the heme group, it has an effect on the geometry and a considerable effect on the electronic structure of the heme rings. Thus, using resonance Raman spectroscopy, the π to π* transitions that give resonance will be influenced by two major factors, an electronically driven change caused by oxygen binding and a sterically driven change caused by the cooperative movement of the protein. They used several peaks to determine how oxygenated the blood was including using the ratio between the peaks at 1383cm^{-1} and 1602cm^{-1}.

This once again indicated the great potential of Raman as a diagnostic tool. Furthermore, in 1988 a review paper named "*Medical Application of Raman Spectroscopy*" provided a comprehensive overview and showed the diverse medical applications being investigated including, looking at protein degradation in ocular lens ageing, whether the contraction of muscle fibres induces changes in contractile proteins such as myosin and actin, investigating the protein coatings of viruses, using resonance Raman *ex situ* to investigate sub cellular mitochondria and looking at the

differences between synthetic and natural enamels of teeth, all of which proved the great potential of Raman spectroscopy for the medical field and diagnostic applications [62]. Moreover in 1993, the use of near infra-red Raman spectroscopy to monitor blood glucose levels was investigated by a group from Oklahoma State University, which has shown that levels of glucose, lactate, ascorbate, pyruvate, and urea could be measured at meaningful levels [63]. They used an aqueous humor in a cuvette to monitor the levels of less than 1 wt % however, the detection technology was not very sensitive as it took an hour to get one spectrum and therefore not providing a practical solution for real time diagnosis, yet proving that metabolites could be measured at meaningful levels. A group at the Massachusetts Institute of Technology, in 1996, also used near infra-red Raman spectroscopy and looked at glucose, lactic acid and creatinine in phosphate buffered saline solution detecting levels down to 1.3mM [64]. The spectrum collection time took 100 seconds showing it might be possible to use this technique for real time diagnosis. In 2001, a group mainly from Chalmers University of Technology in Göteborg, showed that by using surface enhanced Raman spectroscopy they could determine doxorubicin levels in blood plasma down to a level of 1μM which is a clinically useful level [65]. In this work a principal component analysis was also used to help recover the information from the complexities of the blood plasma spectrum without the need for any sample preparation, whereas conventional methods for analysing doxorubicin can detect lower levels, yet require a lot of pre-treatment of the plasma and thus taking many hours to complete. In 2002, another group from the Massachusetts Institute of Technology showed it was possible to measure concentrations of multiple analytes simultaneously in whole blood with clinical accuracy, once again, without any sample

preparation [66]. The group quantitatively measured glucose, urea, total protein, albumin, triglycerides, haematocrit and haemoglobin using a partial least-squares algorithm with clinically relevant precision. The researchers also attempted to measure the concentration of bilirubin, however as it is at least an order of magnitude lower than that of the other analytes studied they could not resolve it, therefore, indicating that a more sensitive detection method is needed to measure the lower level of bio markers in blood. In 2005, a group from Northwestern University proposed a system for real time glucose monitoring [67]. They used a decanethiol/mercaptohexanol functionalized surface for detecting the glucose levels which was stable for a 10 day period in bovin plasma. The results were very promising with reliable statistics, with a validation of the data at 87%. In 2012 a group from Boston University published a paper using SERS to look at whole human blood [68]. Here, the investigation started using ordinary Raman spectroscopy and could measure changes in blood that had been stored by seeing the levels of hypoxanthine rising due to the degradation of purine, showing that purine was coming from red blood cells, white blood cells and platelets which were stored at 8°C. This was followed by a comparison between dried and liquid blood samples. An important finding of this study was that it is essential to keep the incident laser excitation at low energy levels (*i.e.,* $< 7 \times 10^4$ W/cm^2 and less than 30 sec data collection time) in order to avoid photothermal and photochemical effects. Subsequently, blood samples were analysed using the SERS method, where the blood was placed on the SERS substrate and allowed to dry. The results showed that using normal Raman most of the signal was obtained from the haemoglobin while the signal detected with SERS was coming from many other blood components. Additionally, it was shown how

blood changes if it is stored over 24 hours at 8°C, and thus importantly demonstrating that for meaningful results, in particular for clinical applications the tests should be performed using fresh blood. Another finding of very similar spectra for whole blood compared to blood plasma using SERS, indicated that there might not be a need to separate the blood into its constituent parts. An additional study by the group from the University of Trieste, in 2014, examined SERS spectra using gold and silver nanoparticles in filtered serum and plasma samples [69], revealing the need to filter the proteins out of the plasma to get any meaningful SERS spectra. Importantly, they noted that ethylenediaminetetraacetic acid and citrate anti coagulants considerably affect the spectral peaks whereas li-heparin does not. The SERS spectra of serum and plasma were dominated by the bands from uric acid and hypoxanthine, instead of a larger set of metabolites, thus suggesting that SERS may not be good for diagnosis in plasma or serum. It is possible that some information was lost due to the way plasma and serum were obtained during the filtering process, potentially removing many important biomarkers. The results over the last few decades with major advances in detector and laser technologies show the great potential for Raman and SERS as a diagnostic tool for real time diagnosis of disease and biomarker detection. Thus we decided to create a test for Traumatic Brain Injury (TBI) which we discuss in chapter 6. At present SERS is not in mainstream clinical use but with the cost of Raman spectrometers and lasers reducing the technique is on the cusp of breaking into mainstream clinical diagnosis.

1.3.3 SERS as a Tool for Detecting Traumatic Brain Injury

TBI is a leading and increasing cause of death and disability worldwide and by 2020 TBI is predicted to become the main case of neurological disability and as such, has created the need for a low cost and rapid point-of-care (PoC) diagnosis test urgently. The increase is due to increase of fall-related severe head injuries with age among older people [70] and road traffic accidents for all ages [71]

In emergency-care practice, life-critical decisions must be made within a period of minutes that influence patients' prognosis and the efficacy of treatment. In the current system over half of major trauma patients are over-triaged and a third are under-triaged, missing significant trauma [72]. The roadside assessment of TBI is a major issue due to many confounders (*e.g.,* hypotension, hypoxia, drugs, alcohol or early intubation). The diagnosis of TBI is made radiologically after resuscitation or often when sedation is stopped several days later, while every hour of delay results in the loss of millions of neurons and billions of synapses. The challenges of accurate diagnosis and monitoring of TBI have created an urgent need for rapid, ultra-sensitive, point of care (PoC) detection of TBI-associated biomarkers. The National Audit Office (NAO) in their report "Major trauma care in England" (February 2010) estimates that there are at least 20,000 cases of major-trauma each year in England resulting in 5,400 deaths and many others resulting in permanent disabilities requiring long-term care. There are around a further 28,000 cases which, although not meeting the precise definition of major trauma, would be cared for in the same way. Major trauma costs the NHS between £0.3 and £0.4 billion a year in immediate treatment. The cost of any subsequent hospital treatments, rehabilitation, home care

support, or informal carer costs are unknown, but it is estimated that the annual lost economic output as a result of major trauma is between £3.3 billion and £3.7 billion per year [72].

Timely assessment of injury severity is a priority in the management of TBI patients. TBI evolves rapidly in the first few minutes to hours, posing challenges in two particular out-of-hospital scenarios: mild-TBI ('concussion') and major-trauma. Even in a hospital setting, the current analysis modalities are not fast (or economical) enough to underpin clinical decision making in rapidly evolving conditions such as TBI. There is a compelling need for testing that can aid the stratification of patients at risk of deterioration and improve initial triage and outcome prediction in the acute setting.

Several blood TBI-indicative biomarkers demonstrate correlation with injury severity and hold potential diagnostic, prognostic and stratification values. However, there is currently no technology to measure these compounds at point-of-injury with sufficient timeliness and sensitivity. Analysis of blood is predominantly carried out in specialised laboratories, using mainly high performance chromatography, mass spectrometry or ELISA, requiring expensive labels for each target biomarker with time-to-results in the range of several hours or even days and requiring complex equipment, not suitable for PoC as we are looking for biomarker levels of less than 100nM and test times of less than 10 minutes. In this thesis a novel and advanced device technology is developed which using surface enhanced Raman combined with microfluidics to rapidly process whole blood is successfully validated for timely diagnosis of severe TBI.

1.4 Thesis Outline

Following the Introduction chapter, the experimental tools and analytical techniques used to complete the research within this thesis are described in detail in **Chapter 2**. The materials and the solvents exploited for the studies, their required processing and the protocols developed and employed to achieve the nano and micro-structures and functional miniaturised devices are also detailed in this chapter. The characterization techniques used to analyse the fabricated substrates and devices including for instance, optical microscopy, electron microscopy, and photolithography and focussed ion beam lithography are discussed along with the theoretical overview of their principals and the relevant history background.

In **Chapter 3**, the theory of the electrohydrodynamic lithography, which lies at the heart of all the fabricated device technologies in this thesis, is introduced and both qualitatively and quantitatively discussing and demonstrating how the externally induced electrostatic forces within a capacitor-like set up can generate very high electric fields yielding highly tuneable, low-cost patterns on a sub-micron scale for a range of applications. Each possible case scenario, either it is the homogeneous electric field or the heterogeneous electric field, where a pre-patterned top electrode is used allowing to fabricate structures down to 100nm scale lengths, are discussed and overviewed in detail.

Subsequently, **Chapter 4** demonstrates the fabrication of our novel vertical field effect transistors assembled from a directly patterned conductive polymer, *i.e.,* polypyrrole using the electrohydrodynamic lithography. In this chapter we also show the testing of these nano scale FETs to assess and demonstrate their performance

using a micromanipulator and using potassium hydroxide as the electrolyte gate. For the development and production of a point-of-care diagnostic platform, an indispensable part was required and it is development, optimisation and testing of the miniaturised portable Raman set-up, designs and iterations of which are described in details in **Chapter 5**. This chapter initially introduces the essential theoretical background on the mechanisms for Raman scattered light, followed by explaining the principals of the surface enhanced Raman scattering phenomena. It is then followed by demonstrating the several iterations of Raman probe design and engineering, discussing the challenging problems encountered, introducing the chosen optimisation steps, all leading a step closer to the optimal portable Raman setup to be integrated with our novel SERS substrates for PoC bio-diagnostics, discussed in **Chapter 6**. Herein, we demonstrate a miniaturised platform technology for timely, sensitive and rapid point-of-injury diagnostics of traumatic brain injury, which is a leading cause of morbidity and mortality worldwide with neuro-disabilities requiring long-term care, of indicative biomarkers. Micro-engineered device technology (MEDTech) is based on label-free reproducible electrohydrodynamically fabricated substrate for surface enhanced Raman scattering platforms enabling versatile, tuneable, high-throughput nanostructures to match the laser-excitation wavelengths, yielding high signal enhancements. These, further integrated within a microfluidic-chip provide highly-sensitive, cost-effective portable devices for direct detection of miniscule concentrations of biomarkers from biofluids, offering useful clinical tests that are simple, rapid and minimally invasive while bringing biodiagnostics to a state-of-the-art point with the tests taking just a few minutes. Using MEDTech to analyse clinical blood plasma samples from patients, we found that TBI-indicative biomarkers

are released immediately after TBI and act as markers of primary injury, suggesting the potential for enabling a significant triaging and prognostic value for long-term neurological outcomes, whether in the hospital or in the field setting.

Finally, the thesis concludes with **Chapter 7** summarizing the experimental outcomes, applications and further possible optimisations. This chapter overviews the novelty, advantages and disadvantages of our methods in comparison to the current state of the art existing techniques, highlighting the potential of the electrohydrodynamic patterning as a complementary method for a broad range of future applications. The first successful fabrication and proof-of-concept application in this work has demonstrated patterning of conductive polymers into a range of nano and micro architectures and highlighted the promise in these for the high-density, flexible vertical field effect transistors with improved properties. The chapter then summarises the novelty and the high potential of our MEDTech for traumatic brain injury detection device with its low-cost, rapid and simple detection of TBI indicative biomarkers at the point-of-care. By taking just a pin prick of blood, inputting it directly into a microfluidic chip, rapidly separating out the plasma and delivering it to the active areas on our advanced SERS platform and subsequently, shining a laser upon the substrate, the generated scattered Raman light with its corresponding spectra is then interpreted to ascertain if the patient has traumatic brain injury. The thesis finally concludes with a section discussing the outlook, suggesting further optimisation processes as well as the prospects for the future of both the FET devices and the MEDTech and its applied potential for early-stage detection of other major, devastating diseases such as, cancer, immunology and neurodegeneration.

CHAPTER 2

Experimental Tools and Analytical Techniques

This chapter describes the materials, experimental and analytical techniques used to make and prepare the vertical FET, Microfluidic chip, Surface enhanced Raman substrates and Raman Collection device.

2.1 Experimental Set-Up for Electrohydrodynamic Patterning

The electrohydrodynamic patterning method was used in this study to produce the semiconducting micro and nano-pillars for the field effect transistor (FET) and the unique structures for the surfaced enhanced Raman substrates and thus, it was an integral part for the research in this thesis. The basic setup for the EHD is based on assembling a capacitor style set-up, which is comprised of a bottom conductive electrode with a thin film on top, made from an insulating or conductive material that is to be patterned. Above and nearly perfectly parallel to the film, is another conductive electrode, which can be planner or patterned, with a small, controllable air gap between the electrode and the bottom substrate which is coated with the thin

film. A bias is then applied between the two conductive electrodes to create an electric field, which is in the order of 10^8 V/m due to the very small inter-electrode gap which is in the order of a few hundred nanometers. The whole setup is placed in an oven and annealed above the glass transition temperature of the material to be patterned, softening the material until it is a very viscous fluid. As time progresses, the very viscous fluid moves, redistributing, to reduce the overall system's energy and minimize the electrostatic forces caused by the electric field between the electrodes. This in turn, gives yield to the formation of patterns that either replicate the imposed top substrate structures or, if the top substrate is planar, results in the formation of pillars which are arranged in a hexagonal spacing pattern. The whole device is then cooled considerably below the glass transition temperature of the patterned material. The top electrode can then be removed, leaving the EHD generated structures on the bottom substrate. Below is a detailed description of the materials, solvents and techniques used to produce and characterise the EHD micro and nanostructures.

2.2 Materials

2.2.1 Silicon Substrates

Single side polished silicon wafers were purchased from Si-Mat Silicon Materials with a diameter of 100mm and a thickness of 525µm +/- 25µm. The wafers were *n*-type phosphorus doped, the dopant atoms which are usually pentavalent give more electrons than holes to create an n-type semiconductor structure, with a typical

resistivity of 1-5 ohm cm and a surface roughness of less than 1nm. These wafers were used as the EHD patterning substrates. To be used as the bottom electrode, silicon wafers were cleaved, using a diamond scribe and a ruler, into 10 x 10 mm^2 squares and for the top electrode, 7 x 7 mm^2 squares. To produce a range of structures other than pillars pre-patterned silicon wafers were used as the top conductive electrodes (Figure 2.1). These were produced by Xtreme Lithography, Ulm, Germany and were fabricated by electron beam lithography (EBL). Cad drawings, produced using Autocad 2012, of different structures, including pillars, squares, cross hatch and line patterns were sent to X-lith Gmbh who then produced patterns on 10mm by 10mm substrates with 200µm by 200µm areas of the patterns.

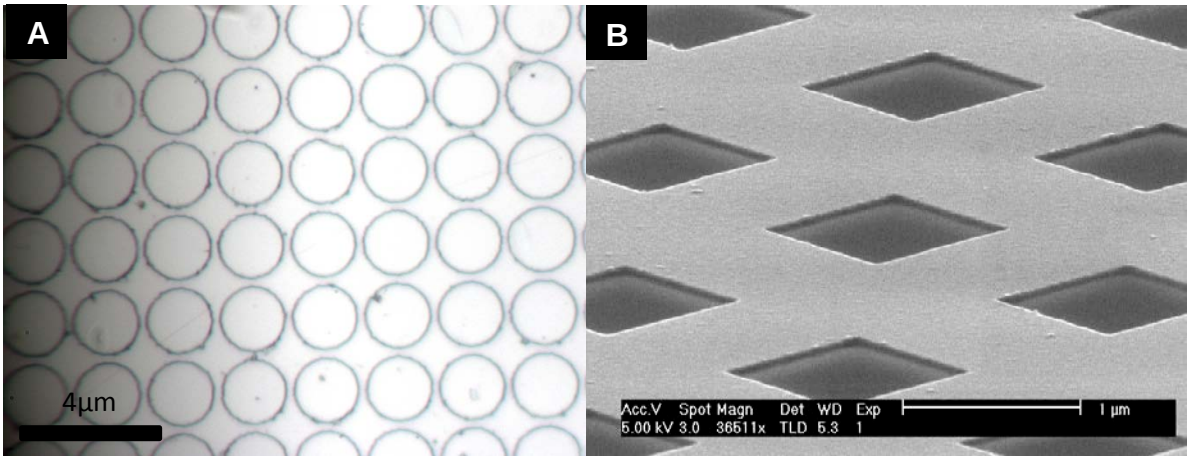

Figure 2.1: Micrographs of patterned top substrates produced by X-lith Gmbh. A) Micrograph of a patterned substrate showing 2µm pillars. B) SEM micrograph of a cross hatch grid substrate tilted to show the topography.

2.2.2 Patterned Materials

To fabricate the pillar structures which were further used as surface enhanced Raman substrates, polystyrene with a molecular weight of 100,000 g/mol, purchased from Fluka 81410-1G and from Sigma Aldrich, was used. To produce the conducting

pillars for the FETs, a second polymer was used, an organic conductive polypyrrole (PPy) which was modified to become soluble in organic solvents and was synthesized, with slight modifications, following the procedure described in patent PCT/KR2001/000982 [73]. More specifically, we used 10g of dry pyrrole monomer and added this to a solution which was comprised of 24.3g of dodecylbenzene sulfonic acid (DBSA) dissolved in 300 ml deionized water (DW). This was then stirred for 30 minutes. We then added 7.3g of ammonium persulfate to 100ml of deionized water and added this to the first solution and this was left to react while being stirred for 18 hours. 300ml of methanol was then added to the solution to stop the reaction. The final solution was filtered to obtain black PPy powder. The PPy was washed several times with methanol and an excess of DW followed by filtering, eventually yielding pure PPy. The molecular weight of the PPy was 157 kg/mol and the glass transition temperature was 98°C.

2.2.3 Thin Layer Gold Sputter Coating

To create SERS active substrates a thin layer of a noble metal is essential to coat the EHD fabricated pillar nanostructures. Gold was chosen for this purpose, as it has the compatible plasmonic enhancement for our requirements of pillar size and the laser wavelength. We used a Polaron E500 which works as a magnetron sputter coater (Figure 2.2). The system works by having the sputtering material *i.e.,* gold, held at a negative potential of 600V. The sample to be coated is placed underneath the gold target at a distance of 4cm and is held at a ground potential. This creates an electric field between the anode, the sample, and the cathode(the sputtering target) all of

which are placed within a vacuum chamber at a pressure of 8 x10^{-2} mbar. Argon is then introduced into the vacuum in small amounts through a leak valve to create an inert atmosphere and because of the electric field, the gas breaks down as the electrons are attracted towards the sample and the positive nucleus is attracted towards the gold target. This in turn, creates the glow discharge plasma.

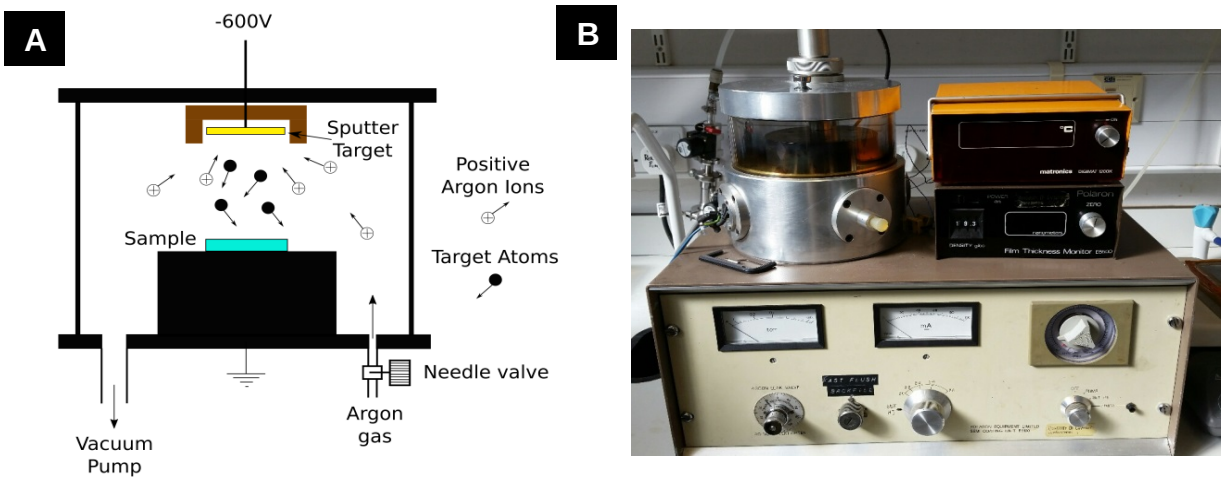

Figure 2.2: (A) Schematic diagram of a sputter coater showing the chamber pumped by a rotary vacuum pump with a needle valve letting argon gas into the chamber. An electric field is generated by applying minus 600V to the sputter target and the chamber at ground potential which ionizes the argon gas, Positive argon ions are attracted towards the negatively charged gold sputter target and collide into the target knocking out gold atoms, which subsequently sputter coat the sample with a thin layer of gold. (B) A photograph of the Polaron E5500 sputter coater fitted with a gold target used in our experiments.

The heavy, positive ions of argon bombard the gold target knocking out gold ions and also creating secondary electrons which help to maintain the glow discharge by continually ionizing the argon gas. The target is also surrounded by a permanent magnet which deflects the electrons away from the sample while ionizing more of the gas. The gold atoms are sputtered everywhere and coat the sample with a thin, nanometre, layer of gold. The thickness of the coating given by the Polaron E5500 was calibrated using substrates coated over various times being measured by an Atomic Force Microscope (AFM).

2.2.4 Surface Energy Modification of the Top EHD Patterning Electrode

During the fabrication process of the SERS active substrates using the EHD method, the top electrode can occasionally adhere to the generated pillar structures and subsequently remove these from the bottom substrate, destroying the EHD fabricated structures during the removal of the top electrode. To prevent this destructive process, we have modified the surface energy of the top substrate by creating a self-assembled monolayer of an organo-silane release agent. Trichloro(1H, 1H, 2H, 2H-perfluorooctyl)-silane (purchased from Sigma-Aldrich, 448931) was used for this purpose. This silane covalently bonds to the oxygen atoms in the silicon dioxide on the surface of the silicon wafer and self assembles into a monolayer which does not adhere to the polymer used for the EHD patterning. For a typical silanization process, we have put two drops of the trichloro(1H, 1H, 2H, 2H-perfluorooctyl)-silane liquid in a boat made of aluminium foil within a desiccator and placed the substrate next to the foil boat. Subsequently, we have applied a rough vacuum for 30 minutes which enabled the liquid to evaporate yielding a vapour atmosphere within the desiccator, eventually generated a monolayer on top of the silicon substrate [74].

2.3 Lithography

2.3.1 Cleaning of Silicon Substrates

It is imperative that the silicon substrates be as clean as possible to give an initially smooth, homogenous layer of the intended patterning material. For advanced cleaning, we used a spray carbon dioxide (SCD) system, which was built in house, to remove the dust particles and other contaminations present on the silicon substrates. The SCD set-up is based on a system used for cleaning large astronomy telescope mirrors [75] [76] combined with an additional technique of heating the substrate to help remove volatile hydrocarbon contamination and reduce humidity. Subsequently, the SCD set-up uses a compressed gas cylinder which contains CO_2 at high pressure causing most of the CO_2 to be a liquid. This cylinder is equipped with a dip tube which is immersed into the liquid, forcing the liquid out of the cylinder, prior to any gas being able to escape. A paint spray gun (Figure 2.3) was directly attached to the carbon dioxide cylinder via an insulated high pressure hose, purchased from BOC, enabling the full high pressure of the cylinder to be sprayed.

Figure 2.3: (A)Photograph of the spray gun converted with PTFE washers inside and a custom exit nozzle used in the CO^2 snow cleaning system. (B) Schematic cross section of custom nozzle.

The spray gun was modified with a Polytetrafluoroethylene (PTFE) sealing washer system, replacing the standard rubber washers, to cope with the low temperatures of the liquid carbon dioxide, which are typically, lower than minus 78°C. The liquid carbon dioxide from the cylinder expands as it exits the nozzle of the spray gun which cools down the CO_2 liquid further and changing some of it into solid particles of carbon dioxide, dry ice, giving a mixture of gas, liquid and solid carbon dioxide. The ratio between dry ice, liquid and gas carbon dioxide can be controlled by adjusting the aperture size of the nozzle of the spray gun. For our CSD system, a nozzle was machined from stainless steel and subsequently drilled to a size of 500µm. Using this set-up, for thorough cleaning of the silicon wafers, we have used a spraying technique of 'from side to side' and 'from the front towards the back' and as the mixture is sprayed across the substrate, at an angle of roughly 45º, the small particles of dust and silicon, typically generated from the cleaving of the wafer are knocked off by the small particles of solid carbon dioxide and the flow of gas. During this cleaning process, the solid carbon dioxide sublimes and therefore, does not leave any residue. Any hydrocarbon contamination is removed from the surface of the silicon electrodes which are also heated to 200ºC during the CSD cleaning, evaporating volatile hydrocarbons. The liquid CO_2 from the mixture acts as an organic solvent dissolving the hydrocarbon contamination which subsequently is blown away by the gas from the spray or evaporate because of the heating [77].

2.3.2 Photoresist

Photoresist is a material that is sensitive to light in such a way that when the material is exposed to light, changes occur within the material and when a

developing solution is used to process the photoresist, either the part that was exposed to the light is soluble in the developer and is removed *i.e., positive resist*, or the part that is not exposed is soluble in the developer and is removed, *i.e., negative resist*. In our experiments, a resist that gave a positive image was used meaning that once developed, the same image that is on the mask is left remaining on the substrate, which will protect the substrate from the later etching process. AZ 1514H positive photoresist was purchased from Microchemicals GmbH and it was chosen because it has good adhesion to metals including copper and is sensitive to ultra violet light in the range of 320nm to 440nm wavelengths. We used AZ® 351B developer which is based on buffered NaOH and was used in a 1:4 dilution (1 part of concentrate to 4 parts of deionized water) also, purchased from Microchemicals GmbH.

2.3.3 Spin Coating Thin Films

Spin coating is a known method for producing thin and ultra-thin homogenous layers [78] (Figure 2.4). For our experiments, we typically require a thin, 1 to 2 µm, and ultra-thin *i.e.,* < 200nm, homogeneous polymer film for the microfluidic chip photolithography and for the EHD lithography, accordingly. We used a Laurel WS-650-23 spin coater to produce the required thin homogeneous films. Typically, a substrate was placed on the chuck and held in place by a vacuum. During the spin coating the lid was shut for safety to prevent anything spinning off the substrate to spread outside the spin coater which was spinning at high speeds or to prevent the substrate coming loose and escaping from the coater. The spin coater itself was also

placed within a fume-cupboard to assure protection from hazardous, evaporating solvents.

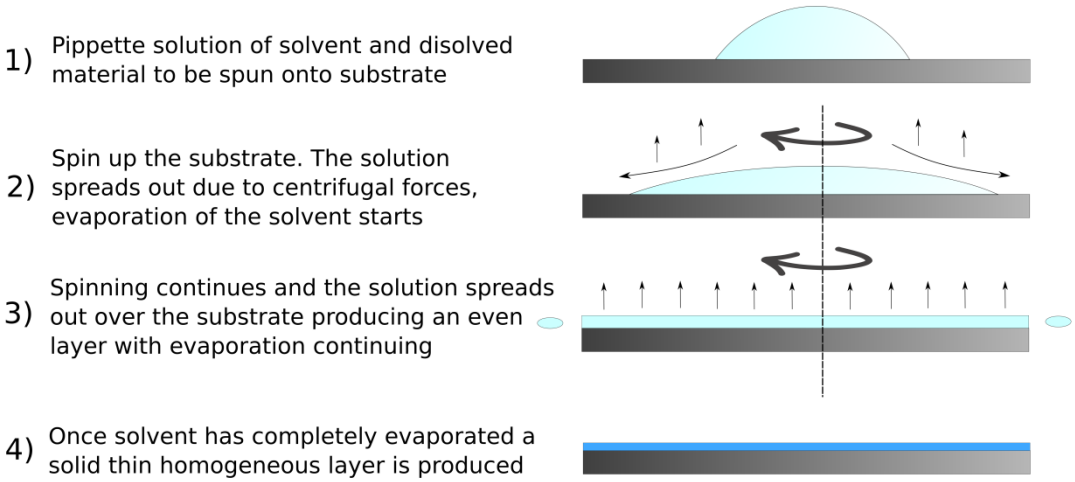

Figure 2.4: Spin coating is a simple way to create a thin homogenous layer. A solution of a solvent with the required layer material dissolved within is pipetted onto the substrate. The spin coater is then spun up and the solution is forced to spread over the substrate due to centrifugal force. Excess solution is spun over the edge of the substrate. The solvent evaporates as time passes and the layer keeps thinning as the spinning continues until all the solvent has evaporated, leaving a homogenous thin layer.

Firstly, a solution of the material with the required concentration to be spun into a thin homogeneous film was deposited on the substrate. The substrate was subsequently spun up with a high acceleration to the desired spinning speed, typically between 1000 to 4000 rpm, chosen depending on the thickness of the thin layer required, viscosity of the liquid and the speed of evaporation of the solvent. As the spin coater accelerates, the liquid spreads radially due to the centrifugal forces and any excess liquid is ejected from the edges of the substrate. The film is continually thinning as the spinning continues until the solvent has entirely evaporated, leaving a solid homogenous layer covering the substrate. The competition between the centrifugal

force, caused by the spinning speed, and the evaporation rate of the solvent determines the final thickness of the film.

Figure 2.5: Interference colours from a thickness gradient in a polystyrene film on a silicon wafer, with refractive indices of 1.6 and 4.1, respectively. (Reproduced from [127]). Starting from brown (20 nm) on the left, through light purple (400 nm), pink (520 nm)and eventually to alternating light green and pink (~ 1.5 μm), the colour eventually changes to a transparent grey for very thick films.

To qualitatively determine the spin-coated film thickness, we used the colour produced from the interference between the light reflected from the surface of the silicon substrate and the light reflected from the top surface of the thin layer of polymer (Figure 2.5) and the AFM as a more quantitative method.

2.3.4 Photolithography Set-Up with a 365nm UV Exposure Unit

Photolithography requires the photoresist to be exposed to a form of radiation to either harden or degrade a part of the resist, which when developed, the unwanted part of the resist layer is washed away. We used a positive photoresist (AZ1514H), which responds to the UV (Ultra Violet) light between 310nm to 440nm. We chose 365nm wavelength LEDs (Figure 2.6) as they were cost effective had a narrow wavelength emission as well as a full width at half maximum of 9nm, thus reducing chromatic aberration of the light through the silica chrome mask.

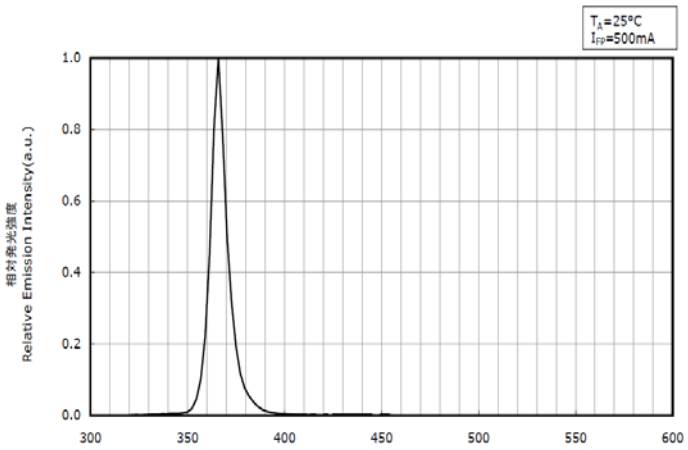

Figure 2.6: Emission spectrum of Nichia NCSU276AT-0365 UV LED 365nm 780mW showing a narrow wavelength emission which is advantageous for sharper mask projection onto the substrate.

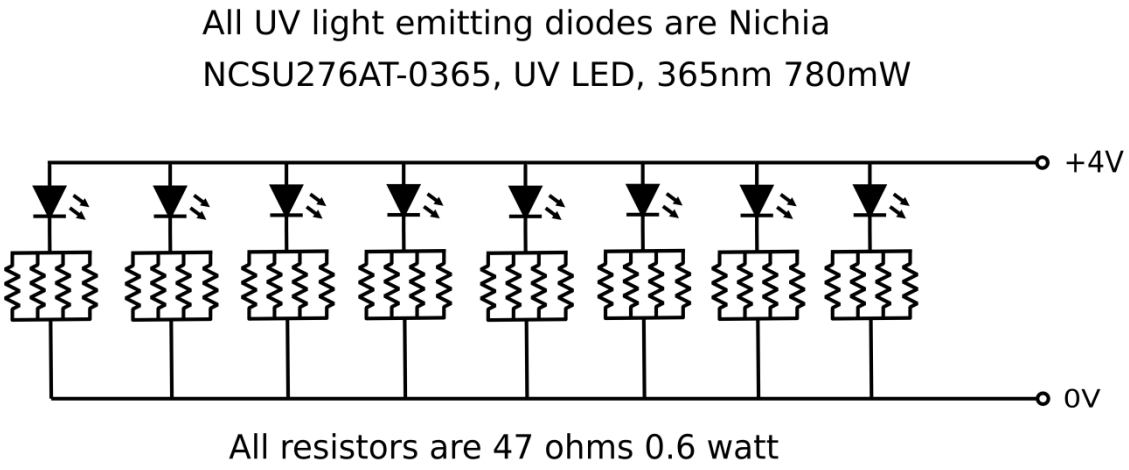

Figure 2.7: Circuit diagram of 365nm LED UV photolithography exposure unit.

A home built ultra violet (UV) exposure unit was made using Nichia NCSU276AT-0365 UV LEDs, 365nm 780mW, 2-Pin in a Surface Mount package (purchased from RS components) (Figure 2.7.) due to lack of timely access to a mask aligner. Eight surface mounted LEDs were organised in two rows of 4 and were carefully hand soldered onto the veroboard, produced by Vero Technologies (purchased from Maplin Electronics) (Figure 2.8.), eight were chosen to give an even beam spread

over an area of 7cm by 7cm. As the beam angle from these leds is over 45° and the distance between the led and the substrate is 10cm the area covered is larger than the required 7cm by 7cm.

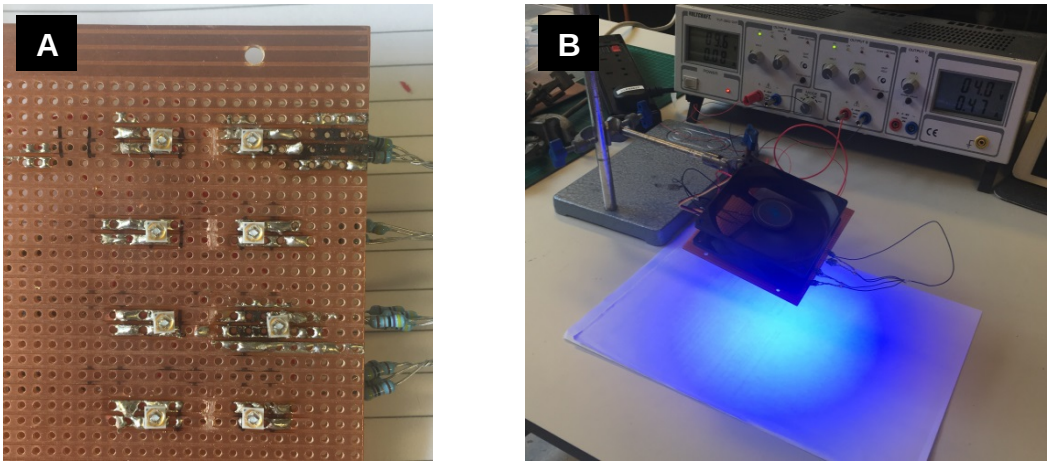

Fig 2.8: (A) Veroboard with Nichia surface mounted UV leds and current limiting resistors just visible on the right hand side. (B) Complete exposure unit showing the setup with a piece of A4 paper fluorescing showing an even spread of the 365nm UV light over an area greater than 7cm by 7cm.

being current limited by four 47Ω, 0.6 watt metal film resistors wired in parallel (Figure 2.7). The LED's were driven at 4 Volts from a laboratory power supply (VOLTCRAFT VLP 2403 0 - 40 Vdc 0 - 3 A240V) with 2 independent outputs, (purchased from Rapid Electronics). A computer 12V 90mm square cooling fan was mounted on top of the veroboard to cool the LEDs and was controlled from the second side of the above mentioned power supply at 6 Volts to run at a slow speed to reduce any vibration. The UV unit was mounted 10cm above the substrate using a retort stand. An exposure time of 2 minutes was used in the experiments, which was established as optimal *via* experimental exposure tests.

2.3.5 Mask Design for Photolithography

The design for the microfluidic chip was initially prepared using Autodesk AutoCAD 2016 and exported in a dxf file format.

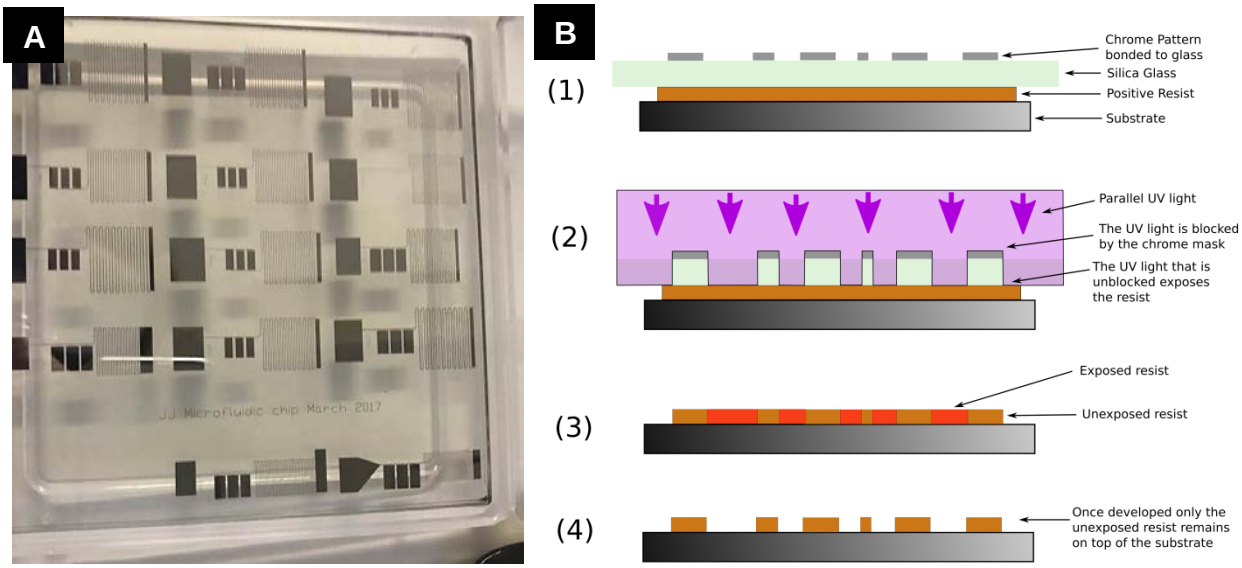

Figure 2.9 (A) photograph of chrome mask showing multiple microfluidic chip designs on one mask. (B) Schematic diagram showing how chrome mask works in contact mode, 1) chrome mask is placed directly on top of the resist, in contact. 2) Parallel ultra violet light is shone through the mask exposing the resist on the parts without chrome on the silica glass mask. 3) The mask is removed and the substrate and resist are developed. 4) Once developed only resist that hasn't been exposed to the ultra violet light remains on the substrate. The substrate can now be used as is or the substrate can be etched with the parts still coated in resist being protected from the etch.

This design was then converted to GDS file format by using the free software Klayout from klayout.de. The final chrome mask was 5" square (Figure 2.9) and placed upon 2.3mm thick soda lime glass with a resolution of class 4, printed by JD Photo Data.

2.3.6 Focussed Ion Beam Scanning Lithography

Focussed ion beam lithography is a scanning lithography technology available to produce very small structures, predominantly over a small area. The machine we

used in this work was a dual beam scanning microscope, FEI Helios NanoLab 650 situated in the Cavendish Laboratory in Cambridge (Figure 2.10), equipped with a scanning electron beam, perpendicular to the ground, and a focussed ion beam at an angle of 52° to the electron beam.

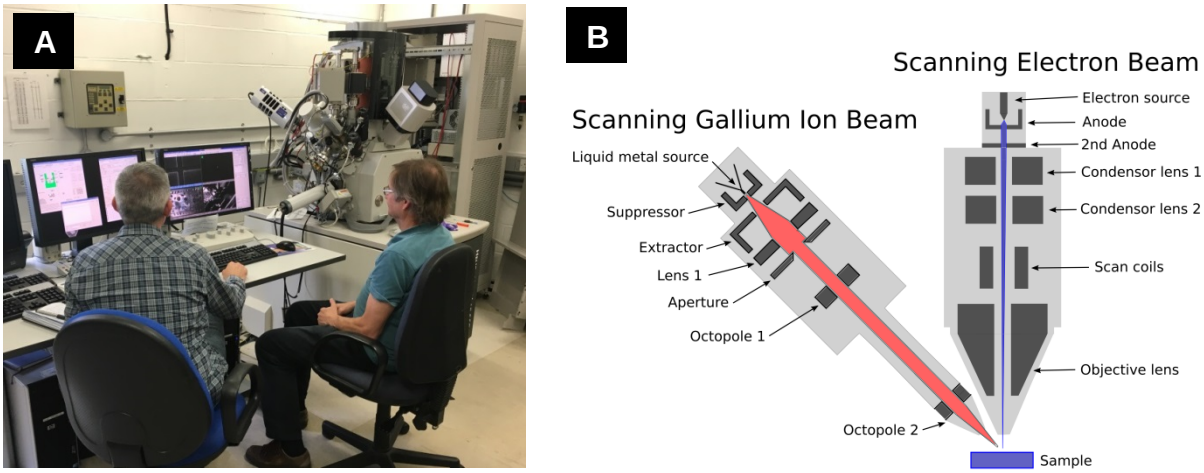

Figure 2.10: (A) Photograph of an FEI Helios NanoLab 650 Dual beam Scanning microscope comprising an electron beam and at a 52 degree angle a gallium ion beam, situated at the University of Cambridge Physics laboratory. An integrated patterning system allows lithography down to a few nanometres scale. (B) Schematic diagram of the Helios dual beam microscope.

The FIB uses positive ions that are focussed using electrostatic lenses to form a spot on the samples surface. Currently, it is possible to buy ion beam machines with sources of Argon, Helium and Gallium. The liquid metal ion source on the FEI Helios microscope is single isotope gallium. The ions are produced by having a sharp tungsten needle with a spiral container of gallium mounted on the back. The needle is mounted facing downwards. When the needle and the gallium container are heated the gallium melts and, due to gravity and capillary forces, coats the needle in a thin layer of liquid gallium. A high electric field is produced by applying approximately 2kV between the needle and a cathode, forcing the liquid gallium

coating to form a very sharp liquid cone tip. The high field strength is sufficient to release the gallium ions from the sharp tip, which are then accelerated towards the cathode with a hole in the middle, allowing the gallium ions through. The gallium ions are subsequently accelerated further by a second cathode and then focused to a spot on the sample using a series of electrostatic lenses and octopole lenses. When the focussed ion beam hits the surface of a sample, the ions sputter away material at any location where the beam is moved, allowing patterns to be sputtered into essentially any material. The ion beam is typically accelerated between 2 to 30kV, depending on the depth of sputtering required at each pass of the beam, also the beam damages the surface leaving an amorphous layer if the sample was crystalline, the depth of this layer can be reduced by lowering the accelerating voltage of the ion beam. The heavy, high energy ions impact the surface of the substrate and knock out atoms, sputtering, which are then pumped away by the vacuum system, with a very small amount redepositing on the substrate in the proximity of the impact site with a proportion of ions implanted into the sample and potentially, contaminating the substrate. The Helios dual beam ion source is a single isotope of gallium to reduce chromatic aberration due to ions of different mass taking a slightly different path through the lens system and thus not focussing at exactly the same point on the surface of the sample, enabling a resolution of sub 5nm at an acceleration of 30kV [79, 80]. The microscope has a built-in 16-bit lithography system allowing simple patterns such as, boxes, squares and circles to be easily created, patterns can also be generated from bitmap Images. Since heavier atoms are sputtered more slowly than lighter atoms, so that patterns of a specific depth can be sputtered into the substrate the patterning software has built-in known sputtering rates for various materials, thus

improving the accuracy of the depth of the sample sputtered away by the lithography system.

2.4 Microfluidic Chip Production

2.4.1 Master Mould Substrate

Copper sheet was purchased from Rapid Electronics (Modelcraft Copper Sheet 400 x 200 x 2mm) and was cut into substrates with dimensions of 75mm x 25mm x 2mm, the thickness of the copper sheet is not critical. The substrates were then hand polished using various grades of wet and dry paper (400, 600, 800, 1200 grades) lubricated with water. The substrates were then further polished using Original Autosol Metal Polish and lastly, with Brasso metal polish. The polished copper substrates were finally cleaned using an acetone soaked tissue and baked on a hotplate at 100°C for 2 minutes in air.

2.4.2 Ferric Chloride Etching

Once the copper substrate has been patterned using the photoresist, etching was required to produce the final master mould. The printed circuit board industry regularly uses ferric chloride to etch the copper coated fibre boards, building upon this, we have exploited this simple, well known technique to etch our master mould substrates. The ferric chloride, purchased from Mega Electronics, was placed in a

plastic tray in a tilting and rocking plate, which gently moves the ferric chloride backwards and forwards, thus keeping fresh liquid in contact with the copper substrate during the etching process (Figure 2.11A). The whole process was carried out at room temperature and the etching was completed in 2 minutes giving an etch depth of 10µm +/- 0.5µm, as measured by SEM.

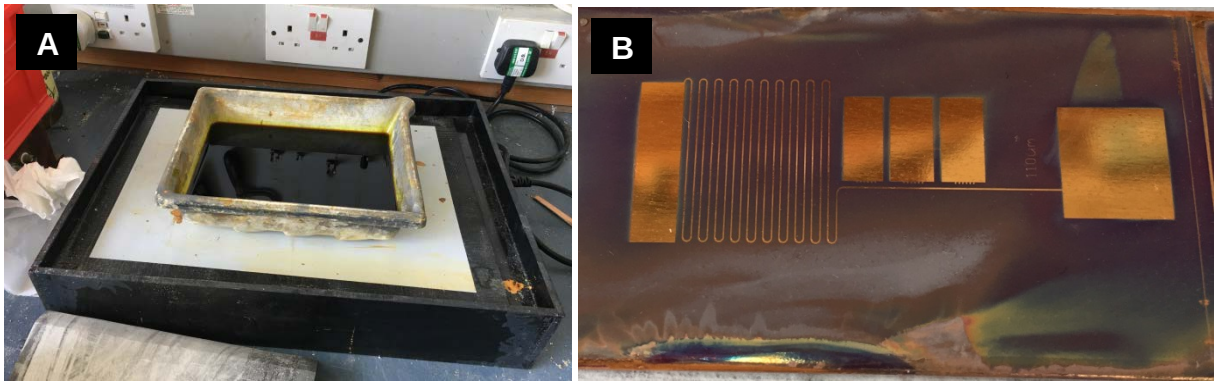

Fig 2.11: (A) Ferric Chloride tilting etch bath. (B) Copper substrate after etching by ferric chloride with the AZ photoresist still on.

Following this, the substrate was thoroughly washed with water for 2 minutes to remove all the ferric chloride residues. Subsequently, the AZ photoresist was removed using acetone (Figure 2.11B). The substrate was cleaned with an acetone soaked cloth and subsequently the substrate placed vertically and sprayed from the top with acetone from a squeezable plastic bottle allowing the acetone to run down the substrate, allowing the residues to flow off. Finally, the substrate was baked on a hotplate at 100°C for 2 minutes in air.

2.4.3 PDMS Casting

To create the microfluidic chip we need to cast a top part that has the microfluidic pattern cast into it which will then be bonded to a glass slide to create the microfluidic

chip. We chose to use PDMS as it is flexible, transparent, economical and easy to work with. Prior to casting, small pieces of silicon were cut and glued, using superglue, to the master mould to create larger voids in the collection areas, blood inlet box and the waste blood collection area (Figure 2.12). To fabricate the microfluidic chip, a material that is clear, with high resolution reproduction and can be easily cast on a mould was required. Polydimethylsiloxane (PDMS) was chosen as a low-cost, simple, biocompatible and reliable casting agent, which is also a popular choice for fabricating microfluidic chips by other groups [81] [82]. Sylgard 184 (purchased from Farnell) polydimethylsiloxane was used as the casting agent in our experiments.

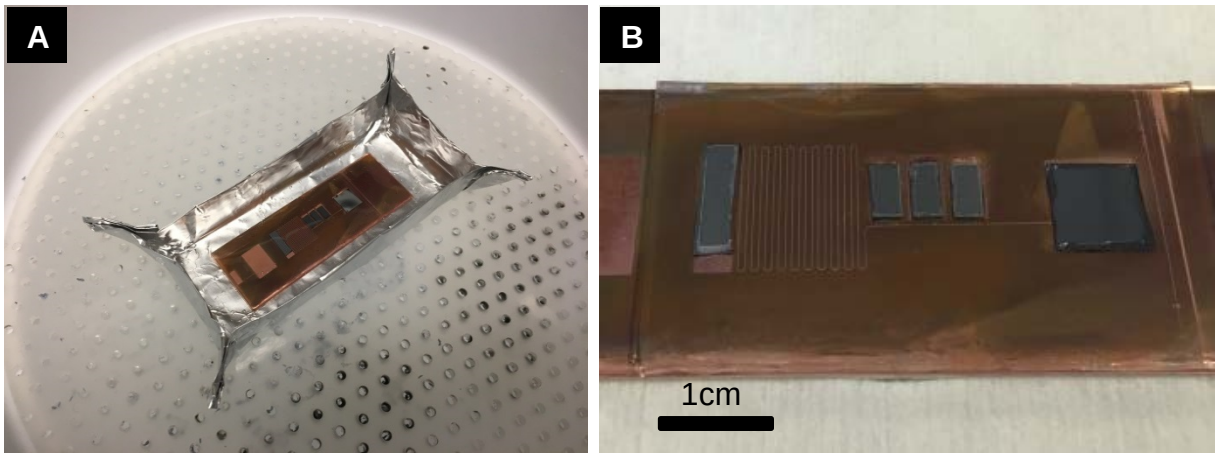

Figure 2.12: (A) the copper substrate within the aluminium foil boat covered with PDMS in the degassing chamber. (B) Copper substrate with cast PDMS on top and trimmed with the collection boxes, blood inlet and waste blood collection boxes cut out.

To cast the PDMS we mixed it with the hardener at a volume ratio of 5 to 1 of silicone elastomer to curing agent, to produce a stiffer than the ‘standard’ PDMS to help in reducing microchannel collapse in the final device, as in previous castings at the standard 10 to 1 mix we saw some channel collapse. The two parts of elastomer and hardener were mixed for 2 minutes. To remove the consequent air bubbles from the

mixture, we constructed an aluminium foil boat, placed the substrate inside and poured PDMS into the boat until the level was about 1mm higher than the glued on silicon pieces on top of the copper master substrate mould. The boat was then placed in a vacuum chamber and pumped for 10 minutes to remove all the air bubbles that were introduced during the mixing of the PDMS (Figure 2.12 A). Subsequently, the boat with the substrate and PDMS was placed on a hotplate at 125 °C for 20 minutes to allow it to set. After cooling the boat down to room temperature, the aluminium foil was peeled off, leaving the copper master mould covered with the set PDMS. Using a sharp clean scalpel, the 3 collection box areas, the blood inlet box and the waste blood collection box were cut out of the PDMS (Figure 2.12 B). Finally, slowly and carefully the PDMS was peeled off from the master mould. No mould release agent was used to help remove the PDMS from the master. A success rate of 80% was achieved in the production of the microfluidic chips.

2.4.4 PDMS to Glass Plasma Adhesion

Once the PDMS is formed and removed from the master mould it needs to be adhered to the glass substrate to form the completed microfluidic device. While the moulded PDMS is hydrophobic, when it is exposed to an air plasma the surface methyl groups (*Si-CH_3*) are changed to silanol groups (*Si-OH*). This changes the surface of the PDMS to become hydrophilic and if both surfaces are silicon based this allows hydrogen bonding of the oxidized surfaces (O-Si-O) [81] [83]. We have therefore, placed the PDMS replica and a glass slide facing up inside a Harrick

Plasma Cleaner PDC-32G-2 and plasma etched it at full power for 1 minute. The PDMS replica was then immediately and carefully placed onto the glass slide, bonding the PDMS to the slide. The correct alignment prior to the PDMS touching the glass is crucial given that it is a one-time bond, once the PDMS is on the glass it is stuck extremely firmly and cannot be moved to readjust alignment. To get the bonding to start it may be necessary to gently press in one corner to get the adhesion to start. A contrast change is visible when titling the slide in the light demonstrating where the PDMS has glued, darker areas, and where it has not, lighter areas (Figure 2.13).

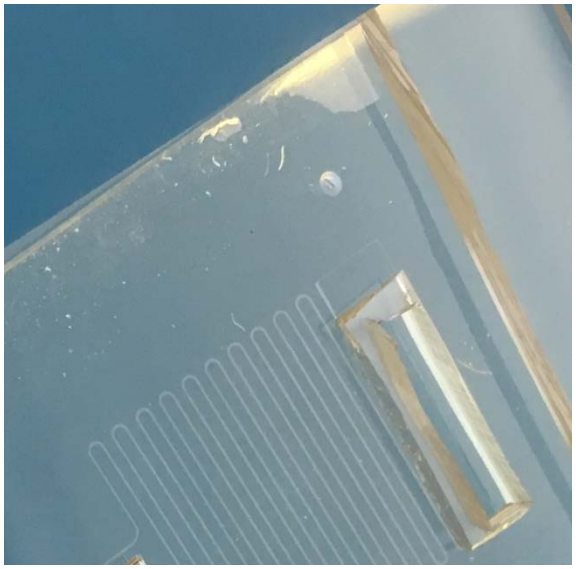

Figure 2.13: PDMS plasma adhered to a glass slide. The microfluidic channels are clearly visible as is a patch at the top of the image where the PDMS has not glued to the glass slide. With just a gentle press in the corner the adhesion will start.

2.5 Characterization Techniques

A range of imaging techniques was used to assess, understand and analyse the produced devices and substrates. While optical microscopy was used predominately

for the initial characterization, it has a resolution limit due to the diffraction barrier, which is half the wavelength of the light. For instance, green light has a wavelength of around 500nm and thus, a resolution limit of 250nm, and therefore, it could not resolve the smallest features produced in our experiments. Subsequently, scanning electron microscopy was used enabling a much higher resolution with for instance, a resolution of 1.5nm at 5kV electron acceleration.

2.5.1 Optical Microscopy

Optical microscopy was essential for analysing the produced devices, substrates, spun coated layers, microfluidic chip and for testing and setting up of the Raman collection box. We used an Olympus BH2 microscope for imaging of the EHD substrates and the microfluidic chip. The microscope was equipped with bright-field reflection and transmission capabilities with magnifications up to 1500 times. The images were viewed and captured using an eye piece mounted CCD camera (5 megapixel Tucsen camera) connected to a laptop. This high optical magnification was required to observe the small sub-micron pillars produced and observe their colours, which indicate the thickness of the pillar structures as well as being able to image the pillar diameters. The optical microscope was also used for imaging the microfluidic chip with the sub-micron filter structures and to visualize and monitor the blood separating process in real time, with red blood cells being disc shaped with a typical diameter of between 6 to 8μm and a thickness of roughly 2μm [84]. The microfluidic chip has a thickness on the order of several millimetres and the standard microscope objectives do not have a large enough working distance with a high enough magnification to image the microfluidic channels and image the blood flowing

through. We have therefore, used Olympus ultra-long working distance objectives with magnifications of 20x, 50x and 100x. It was also necessary to image the laser beam used for the surface enhanced Raman setup for alignment. For imaging the class IIIB 785nm laser beam we have used an Andonstar A1-AV-200W USB narrow webcam-microscope, purchased from Ebay.co.uk, with magnifications between 1 and 500 times (Figure 2.14). The webcam microscope was connected to a laptop *via* USB yielding real-time images and video.

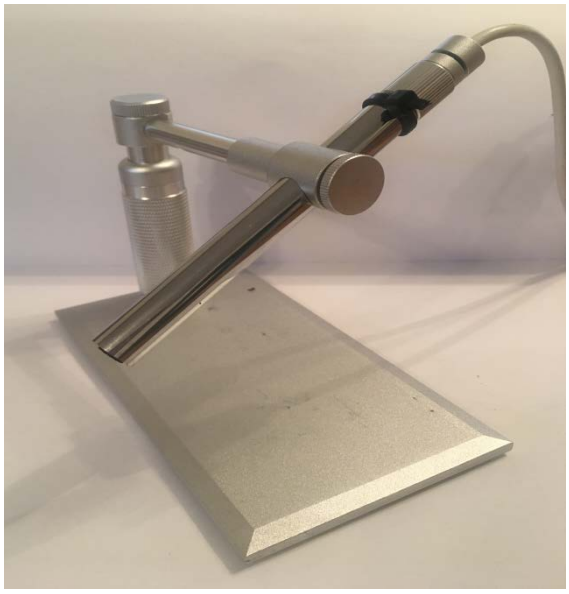

Figure 2.14: Photograph of Andonstar narrow webcam microscope.

2.5.2 Scanning Electron Microscopy

FEI XL30 SFEG scanning electron microscope (SEM) with a Schottky thermally assisted field emitter and an Hitachi S3400 SEM with a tungsten hairpin emitter were employed for imaging samples at various magnifications and accelerating voltages. SEM was invented in 1935 by M. Knoll who was imaging

targets in television camera tubes. Although Knoll did not achieve a very high resolution, only of roughly 10x magnification, it did show the possibility of scanning electron beams [85]. Other researchers also made attempts to construct a functional SEM, notably for instance, V. Zworykin at RCA, however, all failed. This was until 1948 when Sir C. Oatley at the Department of Engineering at the University of Cambridge assigned a PhD project to his student, Dennis McMullan, with the aim of building a working SEM, even though Oatley was told by several experts that it was a "total waste of time" as nothing useful would be seen. Against many odds, McMullan managed to successfully build a functional SEM which was based upon a transmission electron microscope (TEM) he had initially constructed (Figure 2.15).

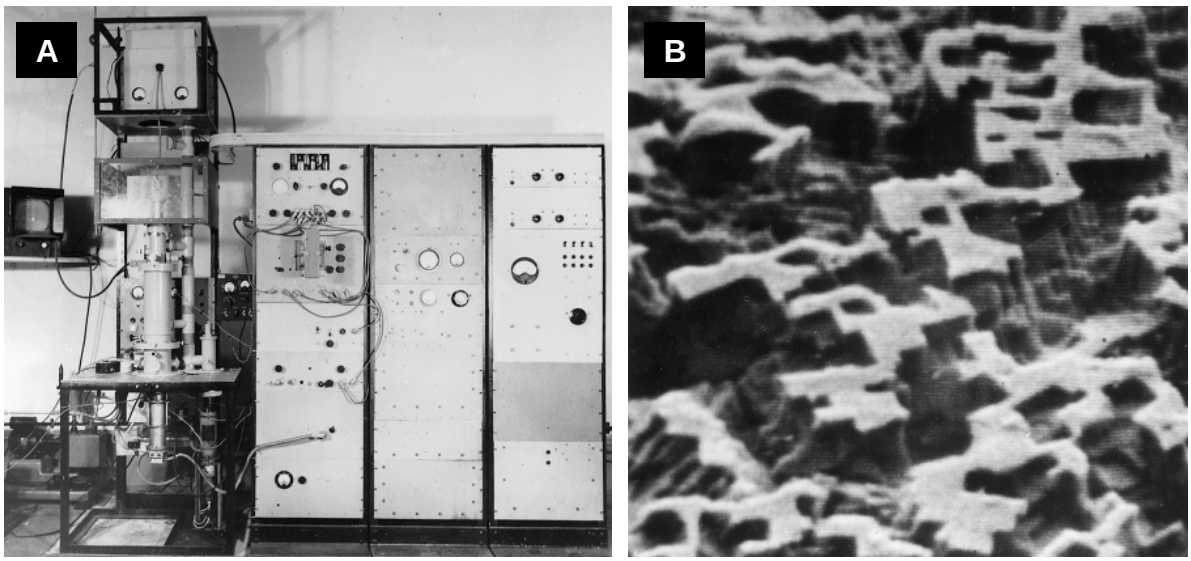

Figure 2.15: (A) The first working SEM named SEM1 in 1953 at the department of engineering at the University of Cambridge (B) An SEM image of etched aluminium sample acquired with SEM1 built by Dennis McMullan in 1952. Reproduced from ref 83.

Over the next few years 5 prototype SEMs were constructed at the Engineering Department and finally, in 1965, the first commercial SEM was released by Cambridge Instruments which was based on the prototype SEM's. The principle of

the SEM is based on de-magnifying a source of electrons which are focused into a spot on a samples surface. There are three main types of sources with the first and the most basic being a bent piece of tungsten wire. Since, at the point of the bend there is a high resistance point, passing a current through the wire, results in the filament heating up at the bend. The filament is heated until turning white and electrons are pulled off by a bias being applied to an anode at a positive voltage compared to the filament. This in turn generates high current, many electrons, however they have a wide spread of energy, resulting in large chromatic aberration in the electron lenses, meaning that the different wavelengths of the electrons are not focussed to the same point by the electron lens. The second source of electrons uses a tungsten needle with a zirconium coating which is heated up to 1200ºC. This generates a Schottky barrier, which when a bias between the tip and an anode is applied, allows electrons to tunnel from the tip, yielding a high current of electrons, narrowing the energy spread of the beam of electrons and thus reducing the chromatic aberration, thus, making the spot size smaller and subsequently, increasing the resolution. The best source of electrons however, is a cold field emitter which is made from a single crystal tungsten needle with a sharpness down to 1 atom. When a bias of around 3.5kV is applied to the anode, a very high electric field is generated at the tip, enabling the electrons to tunnel from the atomically sharp needle towards the anode. This produces a very coherent, in phase, beam of electrons with a very narrow energy spread of the electrons and a very high brightness source, reducing the spot size even more, and yielding the highest resolution. The source of electrons is de-magnified by a condenser lens and then the current needed in the beam is determined by a second condenser lens and

condenser aperture combination. The aperture blocks the outer part of the beam, removing the most aberrated part of the beam and increasing the resolution yet, at the same time reducing the current, which lowers the signal level collected from the sample. The beam is then focused into a small spot on the surface of the sample by the objective lens which is then scanned in a raster motion over the surface of the sample. As the beam of electrons impacts the sample, the electrons interact with the surface and are scattered by the atoms within it giving off low energy, secondary electrons, which provide topographical information as well as the backscattered electrons, which provide the atomic and crystal orientation information. These scattered electrons are collected by a detector, usually an Everhart Thornley or more recently and in lens detector which reduces aberrations caused by the field from the Everhart-Thornley detector, and are amplified at each scanned point and finally fed into a frame store and displayed on a computer screen. The achieved resolution is around 1nm, however, it does depend on the type of sample and the acceleration of the electrons.

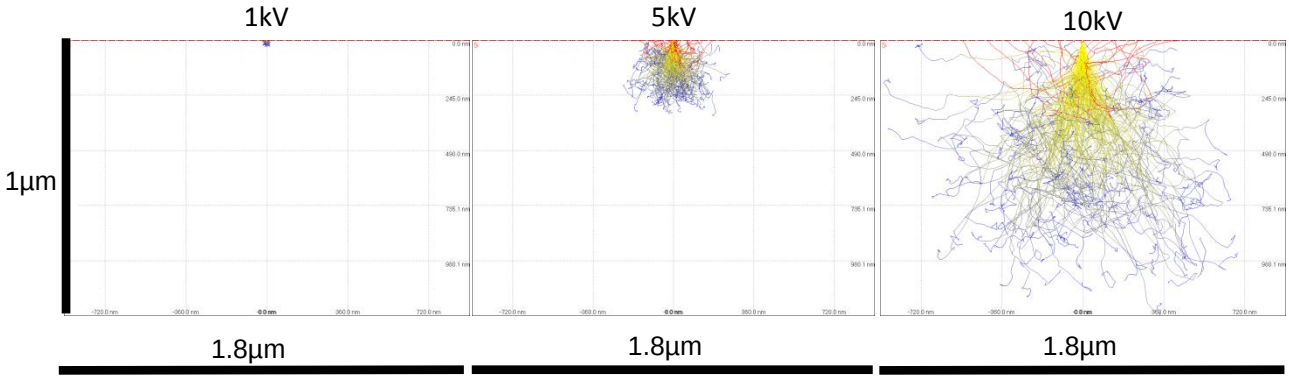

Figure 2.16: Electron interaction volume diagrams computed using win casino 3.0. at different acceleration voltages. The diagrams show the massive difference in interaction volume between 1kV and 10kV and indicate that to see fine surface detail the acceleration voltage must be low.

Another significant resolution limiting factor is the aberrations from the poor electron lenses, despite the fact that the wavelength of electrons accelerated at 5kV is 0.02nm should theoretically allow a sub-atomic resolution. The other resolution limiting factor is the interaction volume of the incident beam (Figure 2.16). The incident electrons have a mean free path depending on the acceleration of the electrons. When secondary electrons are collected, which have a low energy of typically less than 50 eV, only those coming from the surface will have a long enough mean free path to escape from the sample and be collected. As the accelerating voltage of the electrons is increased, not only does the depth of the secondary electrons increase but also the width of collection is increased thus, reducing the accomplishable resolution.

2.5.3 Atomic Force Microscopy

The atomic force microscope (AFM) was invented in 1986 [86] by Gerd Binnig, Calvin Quate and Christoph Gerber. The AFM was based upon the scanning tunnelling microscope (STM) which was invented in 1982 by Gerd Binnig and Heinrich Rohrer who received the Nobel Prize for Physics in 1986 for their invention. The AFM and STM are both part of the scanning probe microscopy family. The AFM has advantages over the STM as it works on non-conductive as well as conductive samples, whereas the STM will only work with conducting samples. The AFM gives high resolution information about topography and material mechanical properties. The AFM uses a sharp tip, usually made of silicon but can be made of other

materials, mounted on the end of a cantilever with a spring constant of between 1 to 100 N/m (Figure 2.17).

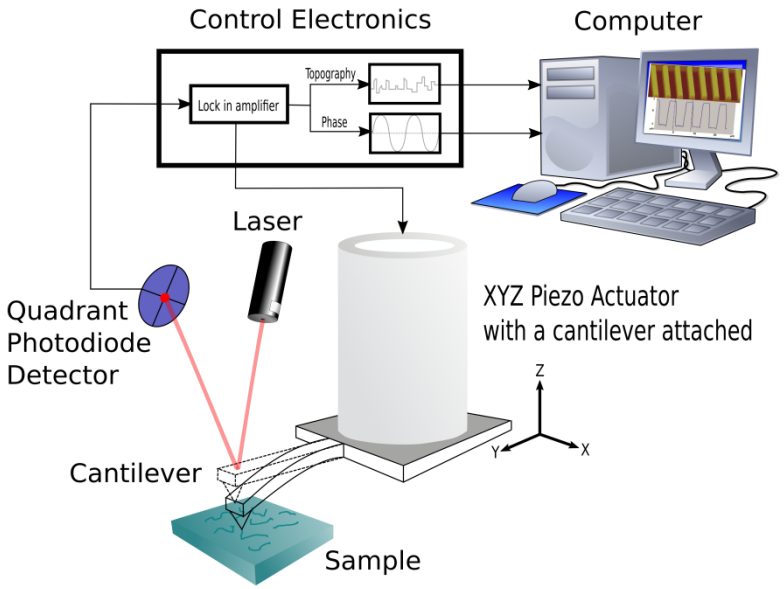

Figure 2.17: Schematic diagram of an atomic force microscope showing the cantilever attached to an X,Y and Z piezo actuator. A laser beam is reflected off the back of the cantilever onto a quadrant photodiode detector, who's signal is fed into a lock in amplifier. If the cantilevers frequency is changed by coming into contact with a surface the signal from the photodiode detector is changed and the Z direction of the piezo actuator is changed until the signal from the photodiode detector is back to its original set position.

The AFM can be used in three main modes, tapping mode, contact mode and non-contact mode, and these can be used in a vacuum, gaseous or liquid environment. In contact mode the AFM works by a laser beam being reflected from the back of the cantilever onto the middle of an optical quadrant detector. The cantilever is attached to a piezo x,y and z actuator. As the cantilever is lowered and comes into contact with the surface the cantilever then bends deflecting where the laser beam hits on the quadrant detector giving an offset signal. This signal is then fed back to the z actuator which adjusts to keep the offset signal constant. Knowing

how far the z actuator has moved to keep the offset at the set point gives a measure of the height of the sample. The cantilever is scanned over the surface in a raster with the z actuator movement monitoring the height changes to keep the laser at the set offset point and thus building up a height map of the sample. In tapping mode the cantilever is oscillated just above the resonant frequency of the cantilever by the piezo actuator in the z direction. As the cantilever comes into contact the resonance of the cantilever is changed. This change in frequency is detected and fed back to the z actuator which as the tip is scanned over the sample adjusts the height to keep the cantilever at the set resonating frequency of just touching the surface, and as the cantilever is rastered over the sample a topographical map of the sample can be constructed from the z height actuator data fed to a computer. It is also possible to use a non-contact mode, as the tip approaches the sample the resonating frequency of the tip can be affected by Van der Waals forces of attraction, between the atoms in the surface of the sample and the atoms at the tip of the cantilever, changing the frequency of the cantilever and this offset frequency is kept constant by the z actuator moving as the AFM head is rastered over the sample. In both tapping and non-contact mode another set of information can be obtained from the setup and that is the phase information which is the difference in phase between the input oscillating frequency and the measured frequency from the reflected laser beam onto the quadrant detector. This phase difference signal gives the stiffness and adhesion of the tip to the surface of the sample, giving compositional differences of the materials in the surface of the sample. AFM measurements were performed using a Nanoscope IV Dimension 3100 (Veeco Instruments Inc.). The AFM was used to measure experimental parameters including the initial film thickness of spun polymer

films, the heights, diameters and the lateral distances between EHD generated structures created in the polymer films. The AFM was also used to calibrate the film thickness against time in the gold sputter coater.

CHAPTER 3

Electrohydrodynamic Lithography: Theoretical Background

In the recent years, there has been considerable interest and developments in the field of electrohydrodynamic lithography (EHL) [87], [88]. The first report of deformation of the surface of a liquid caused by an electric field was as early as 1897 when J. Swan observed that “there were suddenly breaks out on the surface of the viscous liquid a star shaped figure formed of deeply furrowed, closely clustered, outward-branching rays…” [89]. In 2000, the first sub-micron structure was generated using EHL patterning with patterns on the scale of 140nm and it was further suggested that sub-100nm structures should also be possible [90]. Schäffer *et* al showed that by using a patterned top electrode in a capacitor setup it was possible to make structures smaller than the natural resonant wavelength of a thin film, being on the length scale which is useful for making structures for optoelectronic and other devices.

3.1.1 Theory of EHL

The theory of electrohydrodynamic lithography is complex, with the crucial parameters for tuneable patterning being the thickness of the viscous dielectric thin

film, the spacing between the electrodes and the strength of the electric field [90]. It is also possible, with a careful choice of low viscosity polymers to considerably speed up the structure formation process, from hours down to minutes. However, a rapid controlled termination of the process is also essential to prevent the coalescence of the form structures, which can be achieved by *in-situ* monitoring of the current being drawn across the capacitive setup [91]. The basic concept of the EHL is based on the fact that if a thin layer of a liquefied insulator is placed in a capacitor like setup and an electric field is applied across the two electrodes, (Figure 3.1) it results in an amplification of the low amplitude resonant waves, which are always present in the surface of a liquid due to the Brownian motion of the molecules [90].

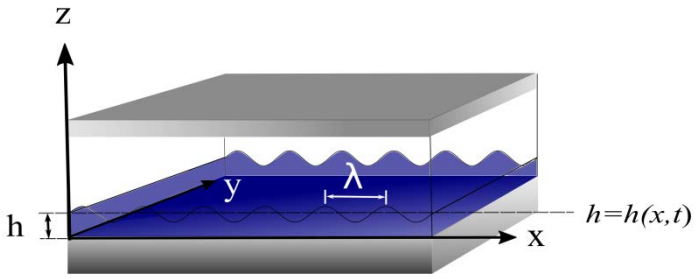

Fig 3.1: Schematic diagram of a thin polystyrene film with a thickness h on a silicon substrate with an air gap and a top silicon electrode. The Brownian motion causes undulations with a wavelength *λ*.

The surface tension, γ is the dominant force opposing the surface fluctuations, attempting to reduce the overall surface area. The application of an electric field, E_p across the polymer-air interface generates high electrostatic pressure and therefore, can overcome the surface tension resulting in the formation of an electrohydrodynamic instability. A typical experimental setup is shown schematically in Figure 3.1. The z–coordinate of the film's interface is given by *h=h(x,t)* where *x* is the lateral coordinate and *t* is the time. To simplify the system and calculate the

resonant wavelength of the instabilities it is sufficient to concentrate on one coordinate. Since the initial undulations are very small, to calculate the initial waves a sinusoidal undulation with a wave number *q* and amplitude ζ can be used:

$$h(x,t) = ho + \zeta\, exp(iqx + t/\tau) \qquad [1]$$

Calculating the time constant *t* for each wave vector *q* (dispersion relation) determines if undulations with wavelengths $\lambda = 2\pi/q$ are exponentially amplified (growth rate $t^{-1} > 0$) or damped ($t < 0$). The Navier-Stokes equation yields the velocity profile, *U* in the film and combined with an equation of continuity for the system the dynamics of the air/liquid interface can be derived. The Navier-Stokes equation for an incompressible Newtonian fluid is given by:

$$\rho(\frac{\partial u}{\partial t}) + u(\frac{\partial u}{\partial x}) + v(\frac{\partial u}{\partial y}) + w(\frac{\partial u}{\partial z}) = -\frac{\partial p}{\partial x} + \eta(\frac{\partial^2 u}{\partial x^2} + \frac{\partial^2 u}{\partial y^2} + \frac{\partial^2 u}{\partial z^2}) + \rho g_x \qquad [2]$$

and the equation of continuity is:

$$\frac{\partial u}{\partial x} + \frac{\partial v}{\partial y} + \frac{\partial w}{\partial z} = 0 \quad . \qquad [3]$$

Since the high viscosity of the liquefied polystyrene film gives rise to a low flow velocity, the Navier-Stokes equation can be simplified and the convective term in the Navier-Stokes equation can be ignored, leading to Equation [4]

$$\rightarrow u(\frac{\partial u}{\partial x}) + v(\frac{\partial u}{\partial y}) + w(\frac{\partial u}{\partial z}) = 0 \qquad [4]$$

Furthermore, a quasi-steady state can be assumed for the system $\rightarrow \rho(\frac{\partial u}{\partial t}) = 0$ and since in a thin film gravity is negligible $\rightarrow \rho g_x = 0$. Also, the in the *x* direction $\rightarrow v = w = 0 \rightarrow \frac{\partial u}{\partial x} = 0$.

Taking into account the above assumptions, results in:

$$0 = -\frac{\partial p}{\partial x} + \eta(\frac{\partial^2 u}{\partial y^2}) \Rightarrow \frac{1}{\eta}(\frac{\partial p}{\partial x}) = \frac{\partial^2 u}{\partial y^2} \qquad [5]$$

and $0 = \frac{\partial p}{\partial y}$ [6]

showing that the pressure *p* is even across the film in the z-direction. Integration of this equation gives a parabolic velocity curve:

$$u = \frac{1}{2\eta}(\frac{\partial p}{\partial x})y^2 + c_1 y + c_2 \qquad [7]$$

The no-slip condition for viscous fluids assumes that at the boundary with a solid the fluid will have zero velocity relative to the boundary:

(i). y=0 u=0 (non-slip boundary condition)

(ii). y=h $\sigma_{xy} = \eta \frac{\partial u}{\partial y} = 0$

Substituting these boundary conditions yields the constants as following:

$$c_1 = -2\frac{\partial p}{\partial x} y\Big|_{y=h} = -2\frac{\partial p}{\partial x} h, \quad c_2 = 0$$

Substitution into equation [7] results in:

$$u = \frac{1}{2\eta}(\frac{\partial p}{\partial x}) y(y-2h) \qquad [8]$$

Furthermore, the lateral Poiseuille flow rate in the direction of decreasing pressure yields the following relation

$$j_x = \int_0^h u dy = -\frac{1}{3\eta}\frac{\partial p}{\partial x} h^3 \qquad [9]$$

The pressure is uniform across the depth of the film. However, it does depend on the film thickness and the pressure distribution at the surface of the film can be written as:

$$p = p_0 - \gamma\frac{\partial^2 h}{\partial x^2} + p_{el}(h) + p_{dis}(h) \qquad [10]$$

p_0 is the ambient pressure, γ is the surface tension. The second term is the Laplace pressure. The third term is the destabilizing electrostatic pressure on the interface caused by the electric field, $E_{p,}$ and the polarization charges [90 92] and given by:

$$p_{el} = -\varepsilon_0 \varepsilon_p (\varepsilon_p - 1) E_p^2 = -\varepsilon_0 \varepsilon_p (\varepsilon_p - 1) \frac{U^2}{[\varepsilon_p d - (\varepsilon_p - 1)h]^2} \quad [11]$$

ε_0 is the dielectric permittivity of a vacuum, ε_p is the dielectric constant of the polystyrene and *d* is the spacing between the two electrodes. The initial sinusoidal undulation (Eq.[11]) with an initial film thickness h_o and initial undulation *A* is given by

$$h(x,t) = h_0 + Ae^{(iqx + t/\tau)}. \quad [12]$$

The last term of the Equation [10] yields the disjoining pressure, which is the pressure due to the attractive force between two surfaces divided by the area of the surfaces [93]. The high electric field indicates that only the electrostatic pressure and the Laplace terms need to be taken into consideration and the balance of the air/liquid polystyrene interface is given by the continuity equation:

$$\frac{\partial h}{\partial t} + \frac{\partial}{\partial x}\left(\frac{h^3}{3\eta}\frac{\partial p}{\partial x}\right) = 0 \quad [13]$$

The dispersion relation of the system, which correlates the time constant τ with the wave vector *q* of the undulations of the film is given by

$$\frac{1}{\tau} = -\frac{h_0^3}{3\eta}[\gamma q^4 + \frac{\partial p_{el}}{\partial h} q^2] \quad [14]$$

These predictions are schematically shown in Figure 3.2. While for $\frac{\partial p_{el}}{\partial h} \geq 0, \quad \tau < 0$ for all q - undulations are damped, so the film is *stable*, for $\frac{\partial p_{el}}{\partial h} < 0$, all modes with $\tau > 0$ and $q < q_c = \sqrt{-\frac{1}{\gamma}\frac{\partial p_{el}}{\partial h}}$ are amplified and the film becomes unstable.

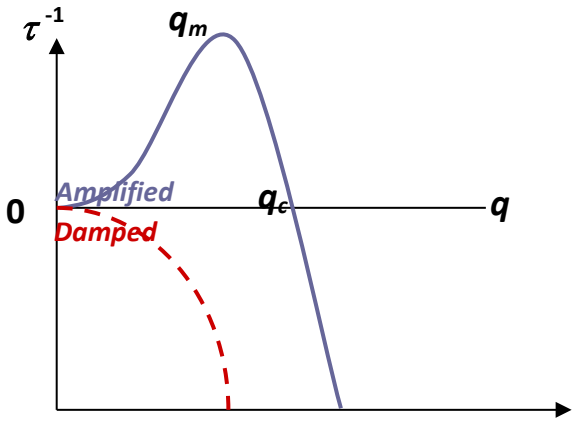

Figure: 3.2. Graph of the dispersion relation (Eq.[13]). When there is zero or a positive electrostatic pressure the modes are damped (τ<0), and the dispersion relation gives a dominant mode q_m with the growth rate time τ_m^{-1}, for a negative p_{el}.

$$q_m = \sqrt{-\frac{1}{2\gamma}\frac{\partial p_{el}}{\partial h}} \qquad [15]$$

Finally yielding the most unstable wavelength, with d being the air gap between the top electrode and the thin film:

$$\lambda_m = 2\pi\sqrt{\frac{2\gamma}{-\partial p/\partial h}} = 2\pi\sqrt{\frac{\gamma U}{\varepsilon_0\varepsilon_p(\varepsilon_p-1)^2}}E_p^{-3/2} = 2\pi\sqrt{\frac{\gamma[\varepsilon_p d-(\varepsilon_p-1)h]^3}{\varepsilon_0\varepsilon_p(\varepsilon_p-1)^2U^2}} \qquad [16]$$

The maximum growth of the instability scales to the forth power, which is proportional to the surface tension and depends inversely on the viscosity for a wavelength λ:

$$\frac{1}{\tau_m} = \frac{\gamma h_0^3}{3\eta} q_m^4 \qquad [17]$$

Equation [17], shows that smaller pattern features can be made by using a thinner initial film, h_0, a smaller spacing between the electrodes, d, or using a polymer with a lower surface tension and a stronger electric field. The defining experimental variables that characterize the instabilities are therefore

$$\lambda_0 = 2\pi[\varepsilon_0 \varepsilon_p (\varepsilon_p - 1) U^2] / \gamma \qquad [18]$$

$$E_0 = 2\pi U / \lambda_o \qquad [19]$$

$$\tau_0 = 3\eta / h_0^3 q_0^4 \qquad [20]$$

Equation [16] can be simplified and written in the form of

$$\frac{\lambda}{\lambda_0} = \left(\frac{E_p}{E_0} \right)^{-3/2} \qquad [21]$$

Equation [17] along with [20] show the effect of the time constant on the electric field:

$$\frac{\tau}{\tau_0} = \left(\frac{E_p}{E_0} \right)^{-6} \qquad [22]$$

In conclusion, λ_0 is the resonant wavelength of the initial instabilities in the thin film caused by the Brownian motion of the molecules, E_0 is the electric field and τ_0 is the time constant of the instability. From equations [18]-[22], it can be seen that the strength of the electric field is the most important parameter for driving and controlling the instability in the polymer film $\lambda \propto E^{-3/2}$ however, the time constant for the onset of the instability has a strong dependence on the electric field $\tau \propto E^{-6}$ also scaling with the electrode spacing, *d*, to the sixth power, $\tau \propto d^6$ and linearly with the viscosity of the film *i.e.,* $\tau \propto \eta$ [94].

3.2 Principle of Electrohydrodynamic Patterning

Building upon the theoretical background described in section 3.1 it is worth discussing the hydrodynamic pattern formation in a more qualitative manner. There are two main case scenarios, one under a homogenous electric field and the other under a heterogeneous electric field.

3.2.1 Homogeneous Electric Field

Typically, for assembling an EHD setup a thin homogenous film of an insulating polymer, between 100nm to 500nm, is spin coated on to the bottom

conducting electrode. This is then opposed by a planar conducting top electrode with a small air gap in the range between 100nm to 800nm.

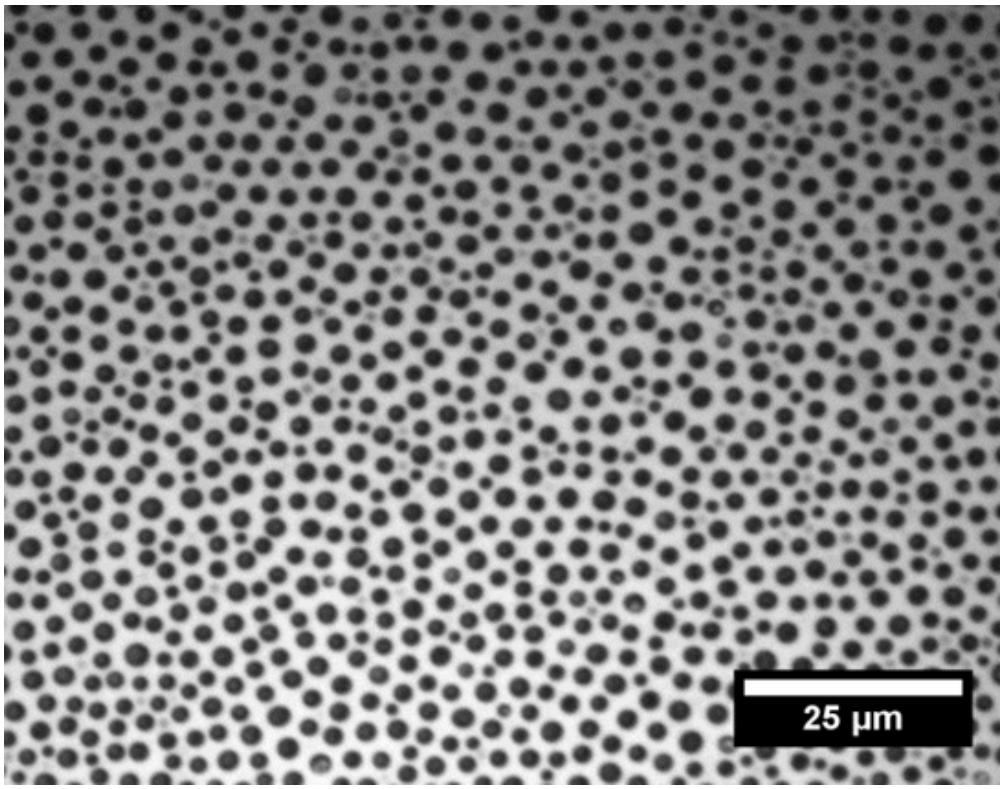

Figure 3.3: Optical micrograph of polystyrene pillars made using Electrohydrodynamic patterning with a planar top electrode. A thin film of polystyrene in the range of 100nm to 500nm was spin coated onto a silicon bottom substrate. Placed on top of this thin film is another silicon top substrate with a small air gap in the range of 100nm to 800nm. The whole setup was placed in an oven and a voltage applied between the two electrodes, between 20V to 100V depending on the air gap. The whole setup is then heated above the glass transition temperature of the polystyrene, 120°C, to turn the polystyrene into a viscous liquid. As time progresses the viscous polystyrene moves to try and minimize the electrostatic pressure build up, caused by the electric field. The polystyrene produces pillars with a hexagonal spacing pattern as this allows the minimum electrostatic pressure. The whole setup is then cooled to room temperature and the voltage removed. The top substrate is then removed revealing the pillar structures on the bottom substrate. This pillar pattern is what is predicted by the theory which shows that smaller pattern features can be made by using a thinner initial film, a smaller spacing between the electrodes or using a polymer with a lower surface tension and a stronger electric field.

Subsequently, the thin film is annealed above the glass transition temperature of the polymer, by placing the whole setup in an oven, and an external voltage is applied

across the two electrodes, in the range of 20V to 100V depending on the air gap size, creating a high homogenous electric field in the region of 10^8 Vm^{-1}. In this assembly there are two opposing forces acting in the system, the destabilizing electrostatic pressure versus the stabilizing surface tension of the polymer film. The dielectric instability generated at the interface between the polymer film and the air gap gives rise to a redistribution of the material into a more energetically favorable configuration. This is typically characterized by the formation of pillars with a local hexagonal spacing symmetry (Figure 3.3). Because of an inevitable slight misalignment, a few um per cm, various stages of the instability can be observed on the same sample, laterally sweeping across the surface. This can be a problem if the misalignment is large but a small angle of misalignment is not a problem as the height difference of the pillars will then be very small.

3.2.2 Heterogeneous Electric Field

To create specific structures and patterns using EHD we need to replace the top planar electrode by a lithographically structured one, this induces a heterogeneous electric field in the capacitive setup. Since the electrostatic pressure is considerably higher under the protruding structures, creating a much smaller spacing, of the imposed electrode *i.e.* $\tau \propto d^6$, the thin film instabilities at these locations occur much faster. The fluid polymer film is guided towards the top electrode structures, faithfully reproducing the top mask features. Similarly, to the homogenous electric field case the initial stages of the EHL begin with the formation of cones reaching towards the top electrode, followed by the cones reaching the top and forming pillars with a flat top. With time, these pillars start to coalesce and

eventually merge into a faithful replication of the imposed structures (Figure 3.5). Electrohydrodynamic lithography enables high fidelity patterning and replication of a broad range of morphologies on a scale ranging from a few microns down to a sub one hundred nanometer dimensions (Figure 3.5). For a homogenous case scenario, electrohydrodynamnically patterned areas covering a few centimeters can be successfully generated, whilst for a heterogeneous electric field, the patterned area is determined by the size of the patterned top electrode. Typically, structured areas of 200x200um^2 have been successfully generated.

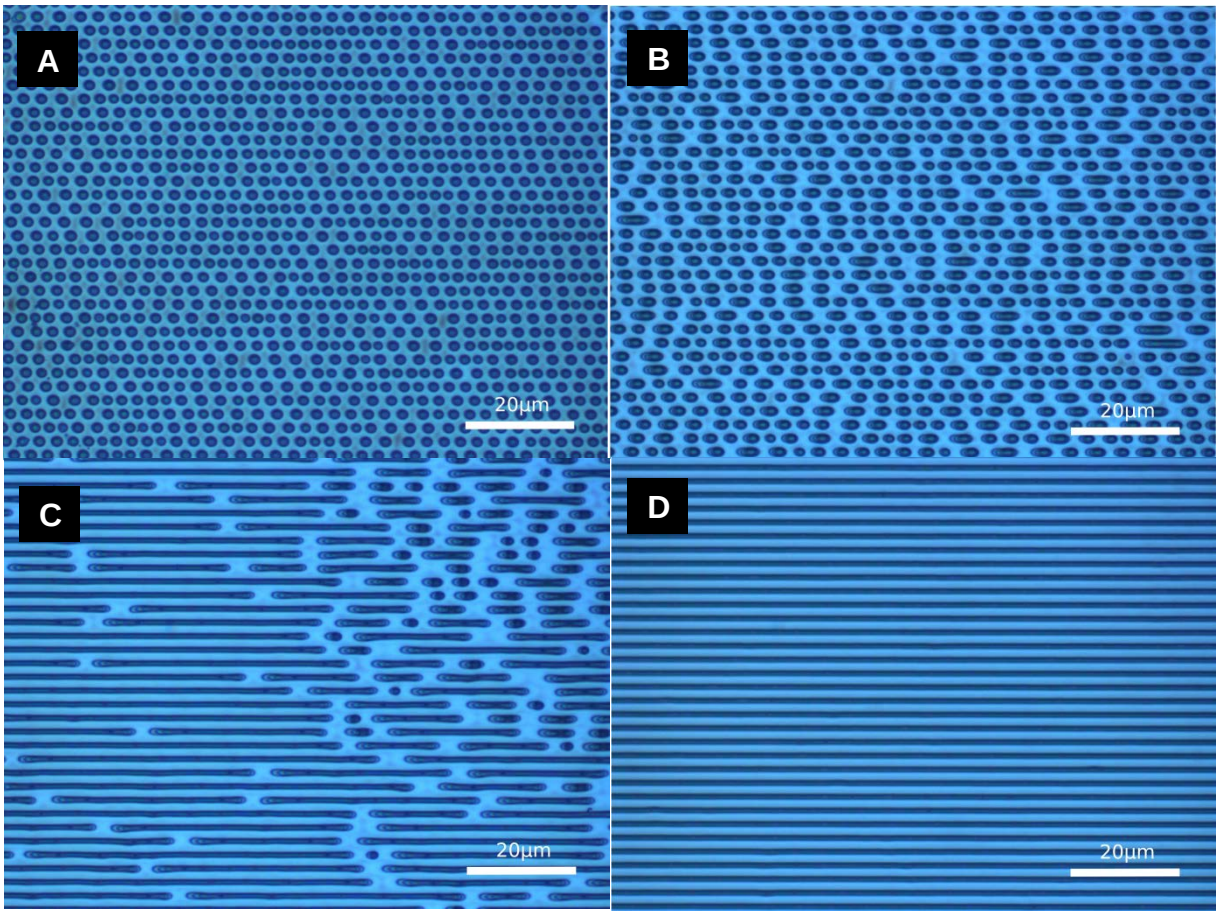

Figure 3.4: Optical micrographs of a time series of electrohydrodynamic lithographic patterning of a Polystyrene film. The top electrode is a pattern of lines yielding a heterogeneous electric field. (A) The patterning begins by forming pillars between the two electrodes. (B) as time continues the pillars begin to coalesce. (C) as even more time passes the pillars coalesce even more beginning to form lines. (D) finally the pillars all coalesce to reproduce the top electrode pattern, in this case lines.

The patterned top substrates can be used many times over to create patterned structures, but so far we have only used them up to 10 times, without any degradation being noted. The patterned substrates can be exploited for a broad range of applications, depending on the materials used for patterning, including for instance, field effect transistors and field emission devices, hybrid biochemical sensors, super hydrophobic surfaces and opto electronic micro devices. EHD substrates can be also used as surface enhanced Raman scattering substrates by covering the fabricated pillars with a thin layer of a noble metal, which could be tuned according to the desired molecules to be detected.

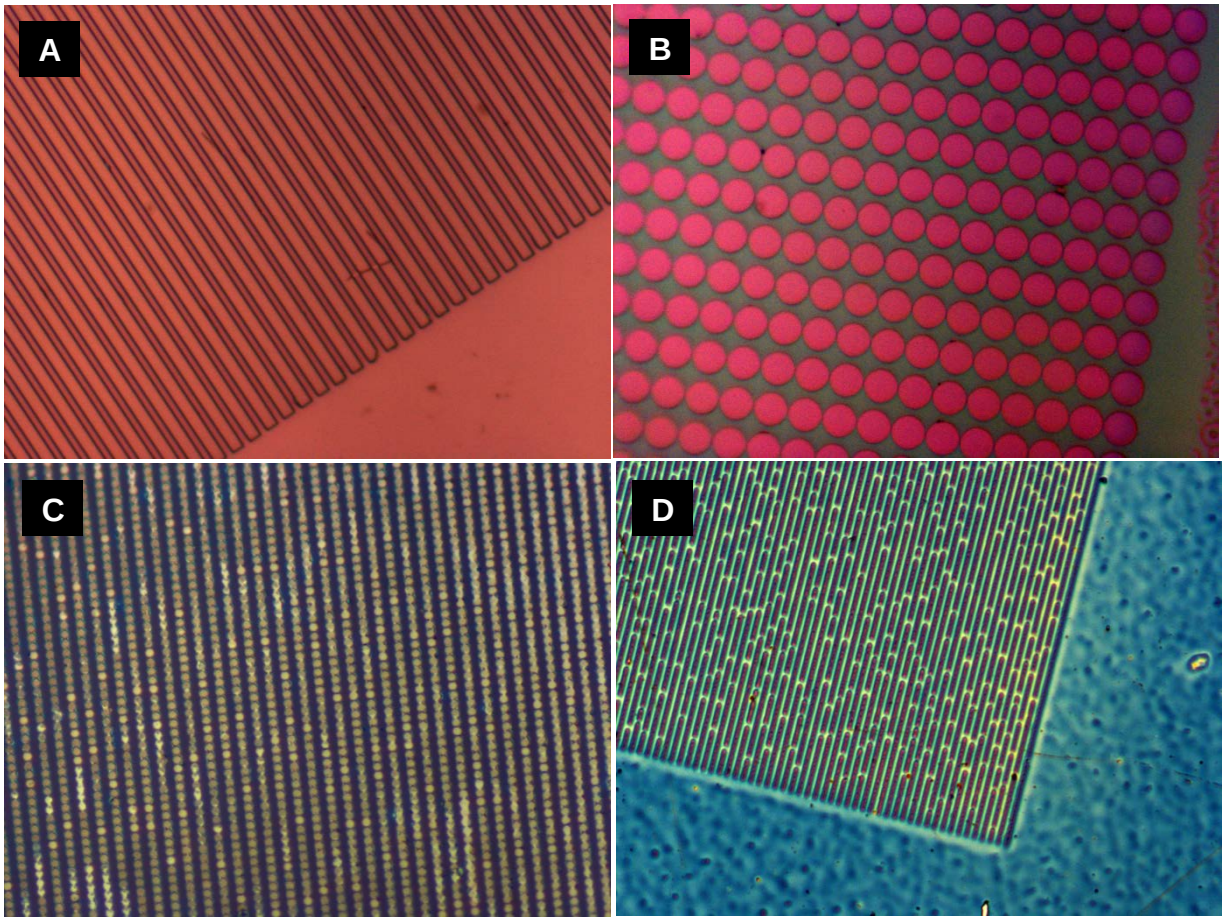

Figure 3.5: Micrographs of electrohydrodynamic patterned substrates created using patterned top silicon substrates from designs we had produced by the company X-lith Extreme Lithography. (A) Pattern of lines. (B) Large pillar pattern. (C) Small pillar pattern. (D) Pattern of lines which are not quite perfect also showing the area outside the top patterned substrate.

CHAPTER 4

Tuneable Nanopatterning of Conductive Polymers *via* Electrohydrodynamic Lithography

Many technologies require the manufacture of conductive structures over large areas with a broad range of dimensions, such as integrated circuits, large flat screen televisions, chemical sensors and large area electronics. We used an advanced yet, a relatively simple method for patterning conductive polymers directly on a substrate with high-fidelity using electrohydrodynamic lithography (EHL). This enabled us to introduce a robust, low-cost method of patterning thin polypyrrole films by exploiting instabilities induced by an external electric-field. We managed to produce well defined conductive structures over length scales ranging from tens of micrometres to a few hundred nanometres. By using a conductive polymer, free charges are suppressed within the polymer film, allowing the EHL based patterning of patterns down to the tens of nanometres. Furthermore, we demonstrate a proof-of-concept of using the fabricated polypyrrole structures for field-effect transistor devices. Employing the EHL patterning of conductive polymers may further allow us to produce patterned structures in the nano and micro ranges thus laying a platform towards various submicron devices such as, super capacitors, flexible efficient and low-cost photovoltaic cells and a range of flexible sensors and displays.

4.1 Introduction

Conductive polymers (CPs) have both the properties of polymers *e.g.,* flexible, soft and easy to mould combined with some of the properties of metals *e.g.,* conductive as well as optical properties. CPs are easy to process, similar to ordinary polymers, their optoelectronic properties can be tuned by doping to alter the conductivity or modified *via* molecular design. The most typical CPS used in the semiconductor industry include, poly(3,4-ethylenedioxythiophene), polyanilines, Poly(p-phenylene vinylene) and polypyrrole, with some being semiconducting and some exhibiting metallic conductivity. Certain CPs are already being used in commercial devices, with organic light emitting diodes (OLEDs) being the most prevalent since many mobile phones use OLED screens along with an increasing production of OLED based large flat screen televisions. Many further scientific studies are also concentrating on using CPs for chemical and biological sensors [95], electrochromic devices [96] and field effect transistors (FETs) [97 98].

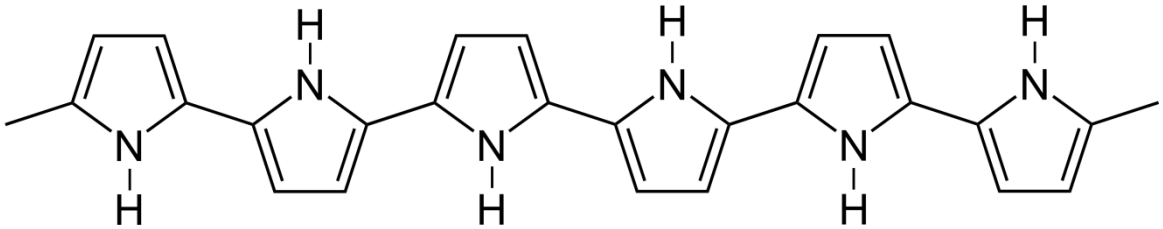

Figure 4.1: The structure of Polypyrrole

However, in order to make functional flexible organic electronic devices we need to be able to pattern over length scales from hundreds of microns down to a few tens of nanometres with a good and robust adhesion to the substrate [99]. Methods for

patterning CPs have been explored and the most successful technique so far is the vacuum thermal evaporation (VTE), which uses a mask to control which areas are coated by the evaporated polymer. However, there are many significant problems with the VTE method since Samsung announced, in 2015, that they would stop the production of the OLED televisions until they could make the processing of these more affordable, especially, given the many failures and artefacts in the existing production [100]. New techniques are constantly emerging to address this need including for instance, inkjet printing of CPs with an MIT spin off company 'Kateeva' having produced a large printer for OLED panels with a $200 million investment [101]. Furthermore, according to the Reuters News agency [102], LG are going to invest $13.5 billion to boost output of organic light-emitting diode screens over the next three years. All these show that there is a crucial need for cost effective and efficient patterning of CPs to further produce a range of novel advanced miniaturised devices. In this chapter, we introduce an elegant and at the same time, straightforward EHL technique for direct patterning of conductive polymers at high resolution. Theoretical studies addressing pattern generation have predicted electrohydrodynamic pattern formation in conducting liquids [103] [104] [105], yet, these have not been demonstrated to date. We use a versatile organic semiconductor, Polypyrrole (PPy) (Figure 4.1), film to generate micro to nano morphologies using the EHL technique and thus, enabling highly-ordered structures which can be further, easily assembled into functional devices. The method we use provides a single-step and cost-effective approach for direct patterning of conjugated polymers [106] [107] [108]. Patterning of thin films using electrohydrodynamic instabilities possesses many desired characteristics and has convincingly been used as a simple method to structure and replicate patterns of

nonconducting, dielectric polymers (*e.g.,* polystyrene (PS), poly(methyl methacrylate), polycaprolactone, nanocomposite carbon nanotubes integrated in PS [109]) on sub-micrometre length scales targeting various applications. However, the applicability of this technique to a new range of materials, *i.e.*, conductive polymers, has not been demonstrated yet. In this chapter, we show that EHL can provide a low-cost high-resolution patterning of functional *π*-conjugated polymers without compromising their properties and therefore, not only enables a tuneable method to fabricate and control the position and dimensions of the generated morphologies (by varying a number of experimental parameters, such as the initial film thickness, inter-electrode spacing, applied voltage, surface tension and lateral periodicity of the master electrode) at a low-cost but also, this technique opens up a new avenue for patterning CPs targeting various applications including FETs, light emitting diodes (LEDs), solar-cells, advanced sensors and microelectronics. Polypyrrole has been experimented with as a thin film for the *OLED's* emissive layers [110].

4.1.1 Principle of the Electrohydrodynamic Lithography of Leaky Dielectric Polymers

The EHL concept exploits an instability induced by an applied electric field across the liquefied polymer-air bilayer sandwiched between two-electrodes in a capacitor-like device. If we use a dielectric polymer when applying the electric field, a build-up of unfavourable displacement charges is generated at the interface between the polymer and the air. This in turn, forces the dielectric polymer to re-distribute in parallel to the electric field lines in order to reduce the electrostatic pressure. If the top electrode is planar *i.e.,* a homogeneous electric field, then this results in a pillar-

like structure spanning the two electrodes with a hexagonal spacing geometry. However, the use of a leaky dielectric polymer yields the reduction in the build-up of the displacement charges in the CP, meaning that the EHD patterning forces are concentrated in the air gap, E^1 [104] (Fig. 4.2a). With the build-up of pressure in the system, the liquid polymer is put in tension and since the only part that can flow is the liquid conductive polymer, aiming at reducing the electrostatic pressure, it consequently, moves parallel to the electric field lines, redistributing the polymer into pillars with a hexagonal spacing symmetry. To tailor the length scales of the resultant structures for technologically useful sizes the CP layer thickness and the air gap distance need to be adjusted to give sizes from 100's of microns to sub 100nm [104]. In order to create patterns on the length scales useful for electronic devices, we need to introduce a heterogeneous top substrate for the EHL patterning which will generate a heterogeneous electric field in the capacitor-like set-up, with variations smaller than the intrinsic wavelength in the pattern of the top substrate we can produce sub-nanometre structures [109].

4.2 Experimental

4.2.1 Materials

All the chemicals were purchased from Sigma-Aldrich. Polished silicon (Si) wafers, with <100> crystal orientation and *p*-doped were purchased from Wafernet Gmbh, with a 100 nm oxide layer were used as substrates. Patterned top substrates were silicon wafers which were purchased from X-lith eXtreme Lithography, Ulm, Germany. Chloroform was used as the main solvent.

4.2.2 Experimental Procedure

PPy which was modified to become soluble in organic solvents was synthesized, following the procedure described in [111]. Briefly, we took 10g of dry pyrrole monomer and added this to a solution which was comprised of 24.3g of dodecylbenzene sulfonic acid (DBSA) dissolved in 300 ml deionized water (DW). This was then stirred for 30 minutes. We then added 7.3g of ammonium persulfate to 100ml of deionized water and added this to the first solution and this was left to react while being stirred for 18 hours. 300ml of methanol was then added to the solution to stop the reaction. The solution was then filtered to leave black PPy powder. The PPy powder was washed several times with methanol and an excess of distilled water followed by further filtering, which gave roughly 70% PPY. The molecular weight of the PPy was 157 kg/mol and a glass transition temperature of 98 °C. Subsequently, thin films were generated by spin-coating from solution onto silicon wafer substrates, typical dimensions of 10x10 mm^2, using a Laurell WS-650-23 B spin coater at a speed of 2500 rpm. A solution was prepared using chloroform as the solvent with concentrations of 3% polymer by weight. The substrates were cleaned, prior to spin-coating, in a `Piranha' solution (3:1 H_2SO_4 (98\%):H_2O_2 (30\%)), and then rinsed with deionised water and dried with nitrogen. To prevent the attachment of the top electrode to the formed CP nanostructures, the electrode was coated with a hydrophobic monolayer of 1,1,1,2H-perfluorodecyltrichlorosilane. The top heterogeneous substrate, with the required pattern etched into it, was placed on top of the CP thin film, leaving a small air gap between the two electrodes (Figure 4.2).

The whole setup was then either heated above the glass transition temperature of the CP or exposed to a chloroform vapour atmosphere to liquefy the CP layer.

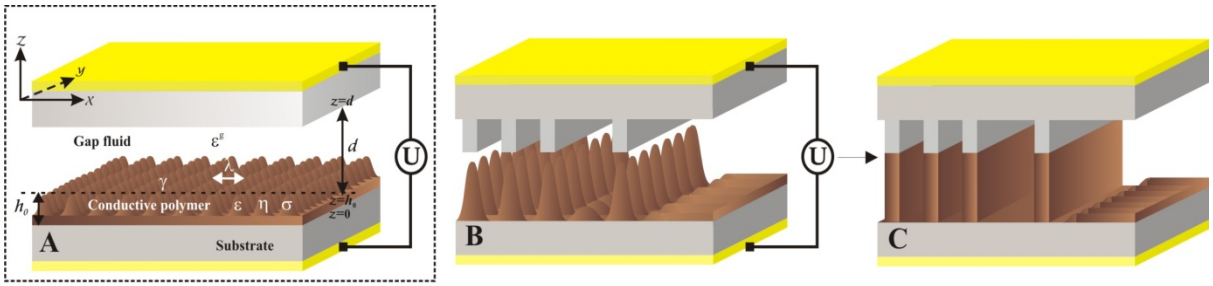

Figure 4.2: Schematic representation of electrically driven patterning set-up. (A) A thin film is liquefied and has characteristic undulations at $z=h_0$. A constant voltage, U, is applied across the electrodes. The potential difference between the substrates gives rise to an electric field, E_f that drives the flow. The dielectric of the film, ε and the gap ε^g moderate the electrical force from the applied voltage. The electrostatic force is initially balanced by the surface tension of the film, γ, giving a characteristic wavelength, λ, of the instability with viscosity η. (B) Heterogeneous top substrate directs the instability towards the protruding line structures where the electric field is strongest creating cones that reach up towards the top substrate and eventually forming pillars spanning the gap. This is followed by a coalescing of the pillars creating a positive replica of the top patterned substrate in (C) In the valleys of the top patterned substrate the film remains stable on a much longer time scale.

To soften the film by solvent vapour pressure we used a homemade apparatus which used Mass-flow controllers (MKS Instruments Model 1179A with a PR4000F readout) which regulated the flux of the carrier gas, N_2 through two lines (Figure 4.3). In one line, the N_2 was bubbled through a solvent-filled bottle resulting in a solvent-saturated gas stream. Both streams were mixed and passed through the sample chamber. The flow volumes per time were individually regulated to values between 1 and 20 cm^3 min^{-1}. The vapour pressure in the mixing chamber was estimated by the ratio of the saturated (p_{sat}) to dry gas (p) flow as determined by the flow-meter readout. All tubes and connectors were made from solvent-resistant

materials, glass and Teflon. The chamber and a regulated water bath containing the solvent bottle and the mixing chamber were held at the same temperature.

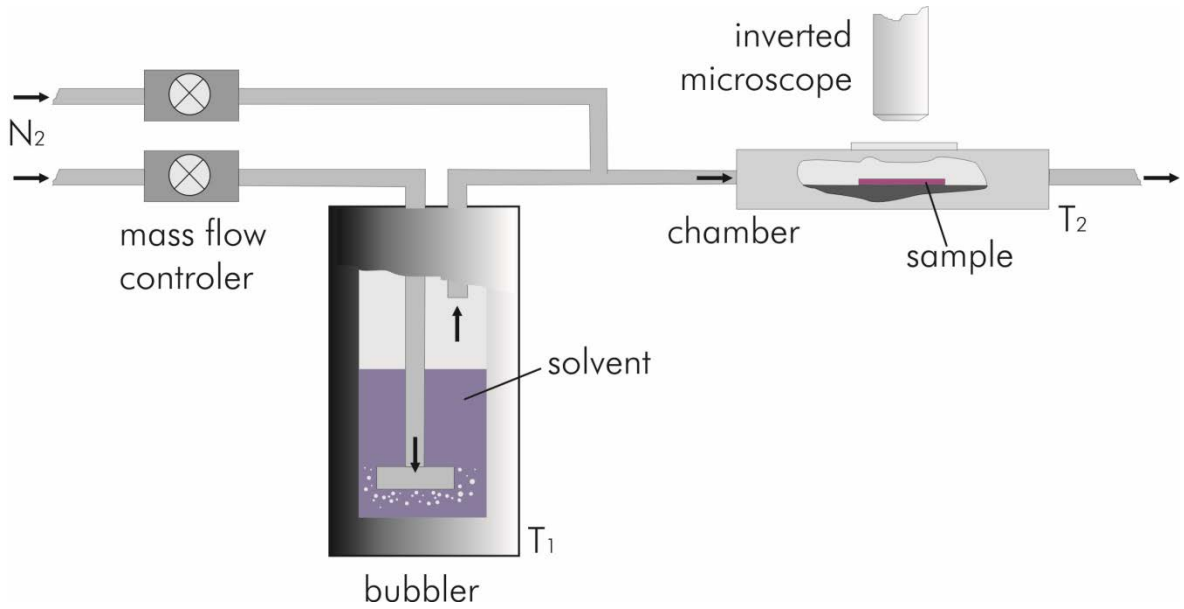

Figure 4.3: Schematic diagram of the solvent vapour pressure EHD setup showing the two flows of N_2 gas coming in with one being diverted through a bubbler chamber to add solvent, chloroform, to the gas flow. The flow rate of each flow is controlled by a mass flow controller to control the final mixed saturation required for the softening of the film. The final mixture of gas flows into the chamber where the sample setup is placed and the bias between the electrodes is applied. As time progresses the structures form to minimize the electrostatic pressure. Once the structures are formed the gas flow from the bubbler is stopped with just the pure N_2 allowed to flow to allow the structures to solidify. The bias can then be removed and the top electrode peeled off leaving the structures on the bottom substrate.

Typical values for the vapour pressures were p= 0.5 and p_{sat} = 0:7. The films were allowed to swell in the controlled solvent vapour atmosphere until they reached their equilibrium thickness after around 30 min. This condition was determined by experiments using a sample chamber lid with a window, providing optical access to the chamber. Using a light microscope in reflection mode the change in film thickness as function of time was qualitatively monitored. A voltage of between 45-80V was then applied between the bottom and top electrodes dependant of the size of the air

gap, with the larger gap requiring the higher voltage. Then cooling the sample to room temperature and removal of the solvent by passing dry nitrogen through the sample chamber solidified the polymer before the voltage was removed, terminating the patterning process and the upper electrode was removed. The sample topography was analysed by using optical microscopy and atomic force microscopy. An Olympus Optical Microscope GX61 was used for the experiments. Using white light reflected from the sample we were able to resolve sub-micrometer features. We were able to monitor electrohydrodynamic pattern formation in the thin films using a digital camera (Carl Zeiss VisioCam). We used a Nanoscope IV Dimension 3100 (Veeco Instruments Inc.) to measure the initial film thickness and the heights of the patterned structures and their diameters and spacing between the pillars. We used tapping mode with NSG 20 cantilevers using a resonance frequency of 260 kHz and a stiffness of 28 Nm^{-1}. The conductivity of the patterned film was measured using a micromanipulator (Micromanipulator Co., Serial No. 820243) with a 1 mm delicate probe and 487 PicoAmmeter/voltage source (Keithley). The electrical measurements of electrolyte gated transistors based on PPy structures in buffered aqueous media of KCl at room temperature under ambient condition were conducted by using a Keithley 2400 semiconductor source-meter and a Wonatech WBCS 3000 potentiostat.

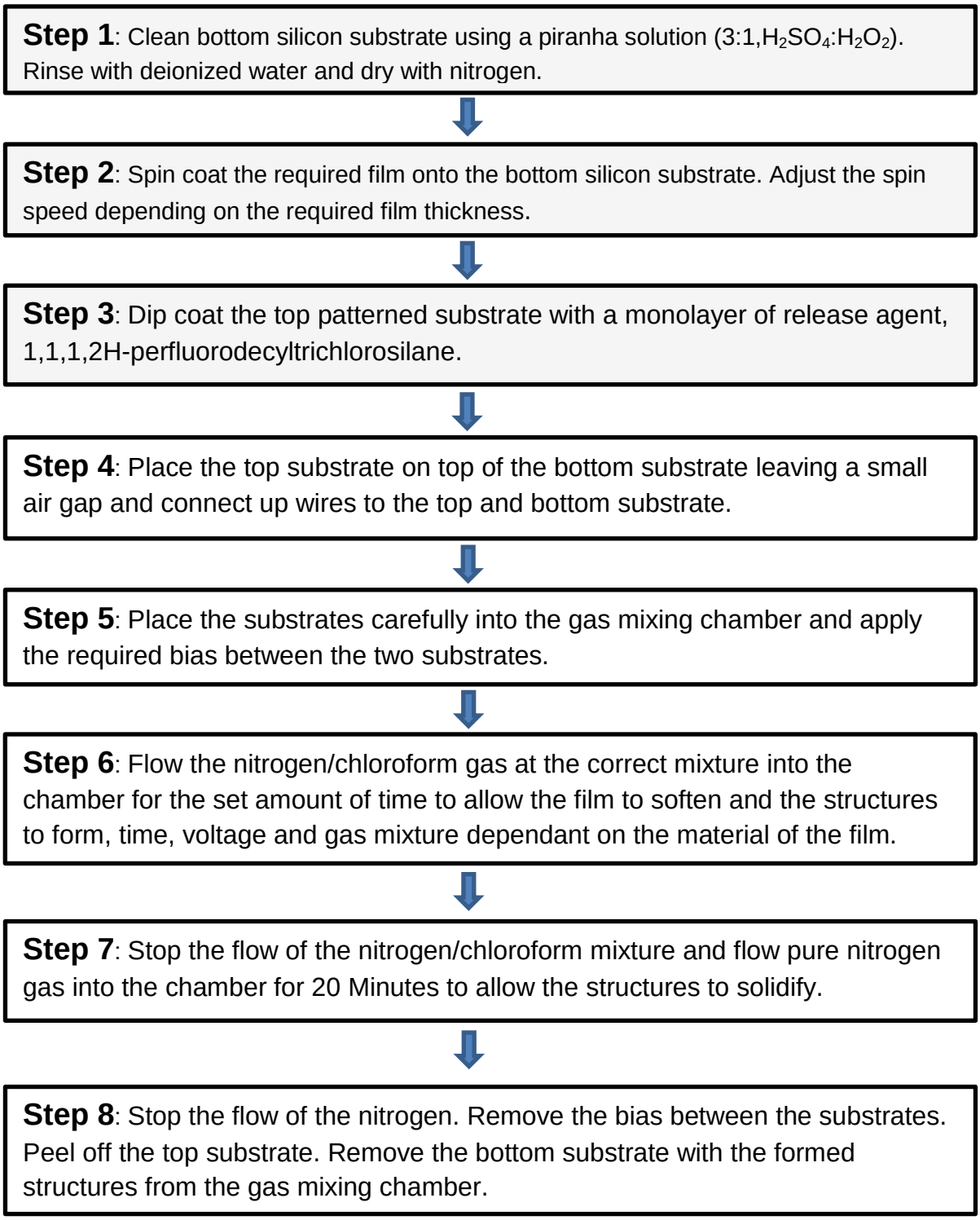

Figure 4.4: Flow diagram of the EHD process using vapour softening of the conductive polymer layer in a mixing chamber.

4.3 Theoretical Background of the EHL Patterning of Leaky Dielectric Polymers

The theory of the EHD process using a perfect dielectric is well understood (see chapter 3) [112] [113]. However, replacing the dielectric polymer with a conductive polymer results in a somewhat different principle of the EHL process where the free chargers in the polymer film modify the electric field distribution in the film-air layer. [104] [105]. The EHL instabilities that cause the pattern formation can be explained in terms of a linear stability analysis for an incompressible Newtonian fluid and assuming a non-slip boundary condition at the substrate (Figure 4.2A). When a voltage, *U* is applied across the bottom and top substrate a destabilising electrostatic pressure, *p* builds up and this pressure scales with the square of the applied voltage.

$$p = -\frac{1}{2}\frac{\varepsilon^g \varepsilon_0 U^2}{(d-h_0)^2} \qquad \text{[Eq. 4.1]}$$

The setup acts like a capacitor with a substrate spacing, *d*, the dielectric permittivity of free space, ε_0 and the dielectric constant of the gap fluid ε^g, the air between the top substrate and the polymer film, *i.e.,* $\varepsilon^g = \varepsilon_1$) Because the polymer film is conductive it is free of a net charge. Thus, the electric field will drive the flow by acting on polarization and free charges at the air/polymer interface. Therefore, it is these boundary conditions that are the driving force for the instability and the coupling between the electrostatic and hydrodynamic fields. Both free and polarization charges are at the interface. This yields the dimensionless conductivity,

$\sum$ representing the ratio of a time scale for free charge conduction to the process time scale

$$\sum = \frac{\sigma\eta\gamma(dh-h_0)h^3}{(\varepsilon_1)^3\varepsilon_0^3U^4} \quad \text{[Eq. 4.2]}$$

where, γ is a surface tension, σ is a conductivity, *d* is the distance between the electrodes, *h* is the height of the film and η is the viscosity of the polymer. With the limit of $\sum$ >> 1, in our process E_f is in the order of 10^8 V/m. Therefore, the most dominant wavelength is given by the balance between the destabilizing electrostatic

$$\lambda = \frac{(2\sqrt{2})\pi}{U}\sqrt{\frac{\gamma(d-h_0)^3}{\varepsilon_0}} \quad \text{[Eq. 4.3]}$$

pressure from the field in the gap acting on the polymer-air interface with respect to the interfacial height, h_0 and the surface tension, γ, acting against the electrostatic pressure to minimise the surface area suppressing the height variations. The time constant for the instability is given by

$$\tau = \frac{12\gamma\eta(d-h_0)^6}{U^4h_0^3\varepsilon_0^2} \quad \text{[Eq. 4.4]}$$

The theory shows when you replace a dielectric material with a leaky one the characteristic wavelength spacing and the instability time constant are shorter showing we can make smaller features in a shorter time leading to structures on useful length scales.

4.4 Results and Discussion

4.4.1 Preparation and Characterisation of PPy for EHL Applications

PPy polymer has been a subject of extensive research looking into its synthesis and applications [114] [115] [116] [117] [118]. PPy can be synthesized by two methods, *via* either chemical or electrochemical polymerization. The main limiting factor of PPy for various applications is its insolubility in many solvents due to very strong intermolecular bonds of the heterocyclic planar structure. Typically, electrochemical polymerization produces rough films which reduce the conductivity of the material and chemical polymerization yields an insoluble black powder. EHL lithography on the other hand, requires an initially thin homogeneous film for successful patterning process. Therefore, we modified the synthesis of PPy [111] to produce conductive PPy which is soluble in various solvents and in particular, in chloroform so we could further spin coat it onto silicon substrates to produce smooth homogenous films as well as use solvent and chloroform vapour softening of this film, both essential for the EHL process. The process, described previously in the experimental procedure, produced 71% pure PPy soluble in DMF, *m*-cresol, THF, and chloroform. Following the spin coating of the 200nm PPy films from chloroform, the measured conductivity was found to be 1.7 ± 0.5 S/*m.* The films were also spin coated onto indium tin oxide

coated glass which were used as bottom electrodes allowing us to to monitor the EHL process *in-situ* using an inverted optical microscope.

4.4.2 EHL Fabrication of Conductive Micro and Nanostructures

EHL patterning enables fabrication of a range of structures, as illustrated in Figure 4.2A-C. If we use a topographically patterned top electrode, it induces an inhomogeneous electric field in the capacitor gap. The Initial instabilities are coupled to the electric field variation and further focussed in the direction of the highest electrostatic force. The highest field is at the protruding parts of the top electrode and the instabilities are drawn towards these structures. Initially, cones are generated in the inter-capacitor gap and with time the cones turn to pillars with flat tops, while spanning the gap between the two electrodes (Figure 4.2B), as more time progresses the pillars merge together faithfully replicating the pattern of the imposed upper electrode (Figure 4.2C). The final height of the EHL fabricated polymer structures is dictated by the gap between the two capacitor electrodes. Despite the shorter destabilization time and faster growing modes of fully conducting material compared to a prefect dielectric, *i.e.,* minutes *vs.* hours [106] [119], smaller scale-sizes are accessible, *e.g.,* in the range of 100nm and below (Figures 4.5A and D). Micrometre arrays [106] [119] [120] and greater aspect ratios are possible, 0.83 as shown in Figure. 4.5. The pattern formation process of Figure 4.2 is reminiscent of the well-studied case of generic polymers, [112] [113] [121] thus, confirming the same underlying physical mechanism. To note, EHL patterning has successfully taken place when using a

heterogeneous electric field, *i.e.*, structured, rather than planar, top electrode. While for homogenous E_f, patterning of CP was somewhat limited, by using a topographically structured top electrode, it was possible to successfully modulate the electric field, decrease the characteristic wavelength and increase the aspect ratio of the structures without causing the electrical breakdown of the capacitor patterning device due to needing to use high external voltages. In the capacitor device the electrostatic pressure is inversely proportional to the square of the distance between the two electrodes, thus wherever the top electrode pattern protrudes down, the gap is reduced and thus, the electrostatic pressure is considerably higher than at the locations with a bigger gap. Figure 4.5 shows optical images with insets of AFM images.

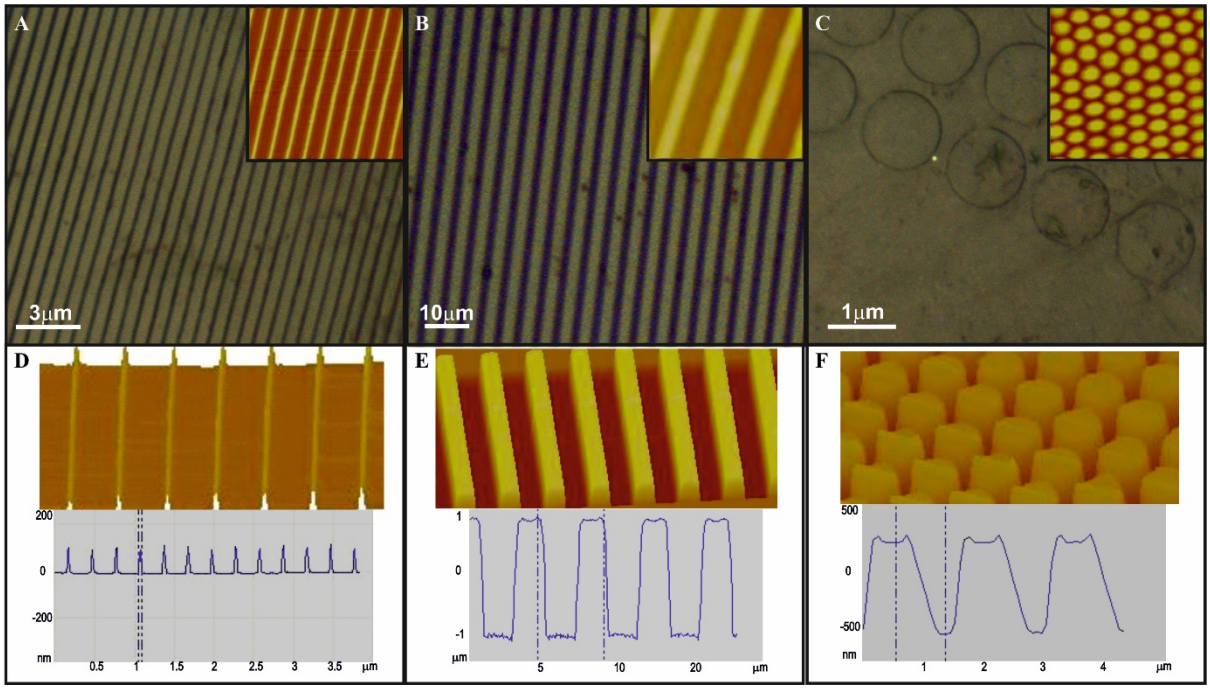

Figure 4.5. EHL replication of line and column patterns. Optical microscopy images with AFM images (inset) and three dimensional AFM micrographs with cross sections showing electrohydrodynamic lithography reproduced PPy structures using different patterned structure top electrodes: (A) and (D) show 120 nm wide lines with a height of 100 nm; (B) and (E) show lines of 2.5μm with a height of 2.0 μm: (C) and (F) show pillars of 700 nm in height, 1.2 μm in diameter and a pitch of 0.5 μm.

section heights of the lines and pillars. The optical micrographs show large areas comprised of conductive PPy patterns with a range of dimensions, successfully fabricated *via* the EHL technique. For instance, the cross-sectional AFM image of line structures in Figure 4.5B reveals a height of 2.0 μm and a width of 2.5 μm. We also patterned ordered columns from a patterned top electrode with the application of 55 V between the electrodes, fabricating structures with a height of 700 nm, a diameter of 1.2 μm and a periodicity of 2 μm (Figure 4.5C). Subsequently, we reduced the topographical feature size and increased the externally applied electrical potential to 75 V, which in turn yielded sub-micron lines of 100 nm in height and 120 nm width (Figure 4.5A). The pattern of the top electrodes were predominantly replicated with high fidelity over the entire area of the top electrode which was typically 200x200 μm^2. Dimensions of a semiconducting channel are known to have a direct impact on the device performance [122] [123]. We can tune the parameters to achieve the required pattern morphology. The rate of pattern formation, the height and the structures width and spacing of the generated patterns can be controlled *via* the adjustment of the applied voltage, the initial film thickness, the inter-electrode spacing and the surface tension of the material to be patterned. As the patterning starts in the initial stages the surface undulation of the polymer is sinusoidal. But as the patterning progresses the surface undulations change towards the downwards protruding structures of the top patterned substrate. The polymer will reach up towards the protruding structures as cones with a wavelength set by the lateral periodicity of the pattern of the structures, the initial film thickness and the applied voltage across the electrodes, top and bottom substrates. In the later stages the replication of the pattern will be formed by the cones coalescing to replicate the top substrate pattern.

4.4.3 Feasibility of the EHL Fabricated Polypyrrole-Based Structures for Field-Effect Transistor Devices

Vertical FETs hold the potential to combine good performance with high device density. The application of vertical transistors in memory devices is especially sought after, due to its potential in shrinking individual devices and capability of multilevel memory structures three-dimensionally. In order to evaluate our EHD produced ppy pillar structures as vertical FETs we created a setup to test them using a liquid electrolyte as the gate surrounding the vertical pillars. As a proof of concept an EHL-generated structure array of PPy pillars was fabricated with a gate length, height, of 700 nm and a pitch of 500 nm as schematically shown in Figure 4.6 A and in Figure 4.3B,i. Liquid-ion gate FET geometry was constructed using a potassium chloride (KCl) solution and a tungsten needle as a contacting electrode (Figure 4.6 A) to the top of a pillar.

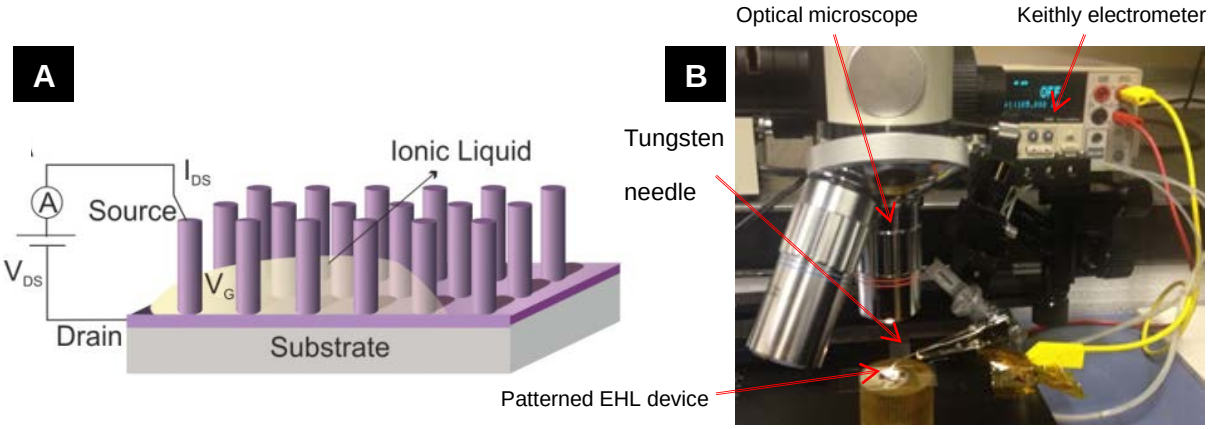

Figure 4.6: (A) Schematic diagram of a liquid-ion gate vertical FET setup to test EHL generated polypyrrole pillars on top of a silicon substrate showing a voltage source between the bottom of the substrate and the top of a pillar. A bias voltage is applied to an ionic liquid to create a field surrounding the pillar to control the flow of current through the pillar. (B) Photograph of test setup showing the tungsten needle in a micro manipulator touching the top of a pillar. An optical microscope with ultra-long working distance lenses is used to aid positioning of the micromanipulator needle on top of a pillar. A Keithley 2400 electrometer was used to measure the current flow through the pillar.

The electrical drain to source current (I_{ds}) *versus* drain voltage (V_{ds}) characteristics of the device as a function of different gate voltages (V_g) are shown in Figure 4.7. The graph in Figure 4.8 presents the transfer characteristics of source-drain current *versus* gate voltage, I_{ds}-V_g at a constant drain-source voltage (a representative value of V_{ds} = 4V). The positive gate voltages decrease the current and the values of I_{ds} increase upon raising the positive V_g at a negative V_{ds} indicating that the device exhibits *p*-type FET behaviour with the holes being the major charge carriers. This current modulation due to the modulation of carrier density in the PPy structures along with the onset of the saturation of drain-source voltage at approximately 9V is consistent with the measurements previously performed on other PPy-based transistors [124 125].

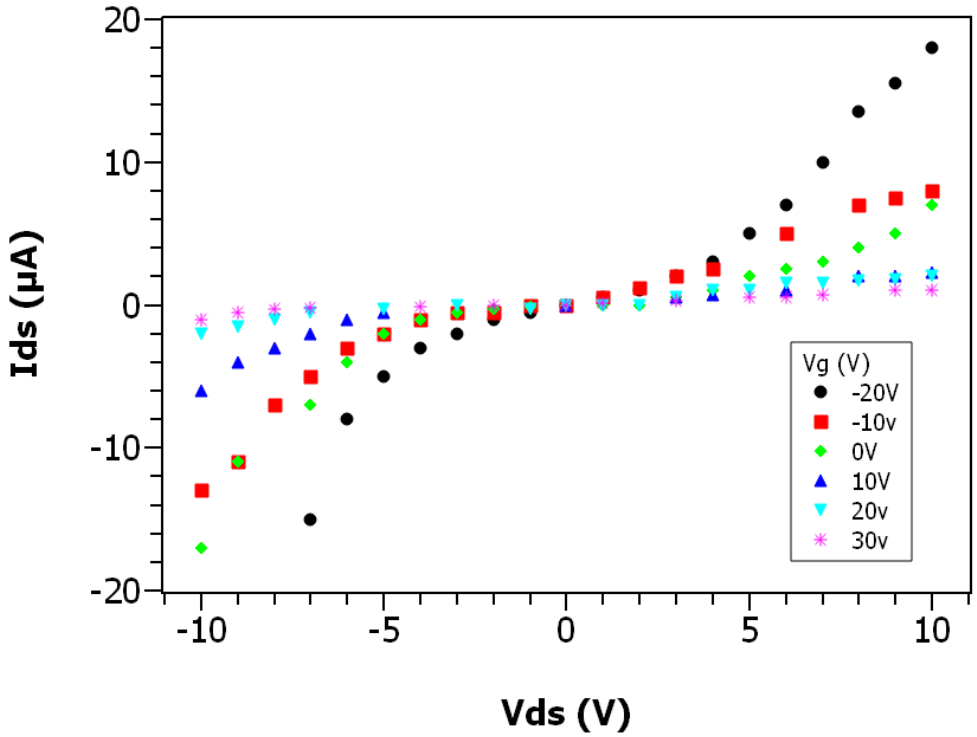

Figure 4.7: Graph of drain to source current *versus* drain to source voltage characteristics at different gate voltages of PPY electrolyte-gated vertical field effect transistor based on EHL fabricated pillars. The graph is asymmetric showing that current flows more easily from source to drain than from drain to source.

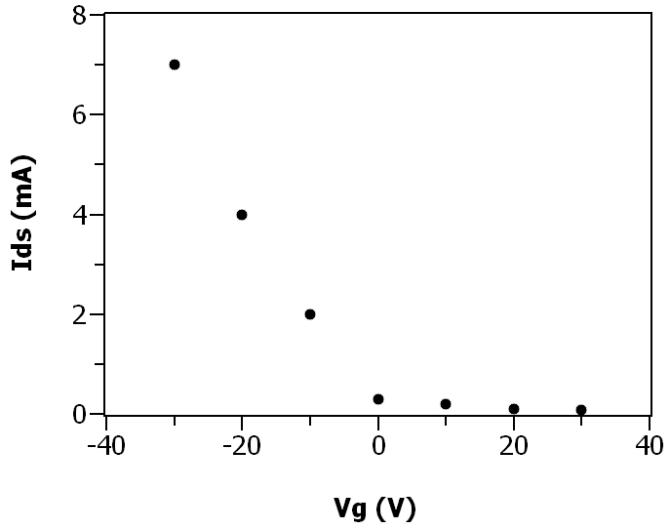

Figure 4.8: Graph showing the transfer characteristics of source to drain current *versus* gate voltage at a constant drain to source voltage of 4V.

The maximum value of I_{sd} of the transistor was 20mA in the 0.01M KCl solution at V_g=20V. Furthermore, structured conductive polymer based substrates exhibit an increased electrochemically accessible surface area along with the high electrical conductivity. Functionalization along the longitudinal axis of the structures can further enable generation of well-defined electrical contacts and may provide a route for incorporating chemical functions. This is potentially useful for the development of rapid-response biochemical sensors which are selective for targeted chemical and biological molecules. Further optimisation of the EHL fabricated electro-conductive micro and nanostructures will enable miniaturised device technologies which can be exploited directly as arrays of electrodes to fabricate all plastic FETs and sensors. Along with promising electrical transistor characteristics, the use of low-cost lithographic technology and simple gate definition process steps could make such devices suitable candidates for next generation technology nodes.

4.5 Conclusions

In conclusion, it is feasible to use electrohydrodynamic lithography for patterning conductive polymers directly on silicon substrates which yields high fidelity structures with a wide range of feature sizes. The patterning of PPy provides a *proof-of-concept*, showing the versatility of the EHL method which can be further applied to a variety of CPs. As yet the device has no uses but was tested as a proof of concept to show that EHD generated PPy pillars could function as vertical FETs. We only used one geometry as a proof of concept to show the feasibility. It should be possible to produce sub 100nm patterns over large areas if the correct setup parameters are chosen, ultra-thin CP layers and a suitable top patterned electrode. Conducting polymers, when patterned on the sub micrometre scale, have improved performance compared to structures on a larger scale and the bulk material which could allow the development of sensors, displays, and microelectronics. For example, high density electrically conducting microstructures can be directly used as miniaturized sensors. We can extend the EHL technique further to create complex hierarchical structures consisting of bi-layers or a larger number of different materials with different conductivities. This is the first time that a conductive polymer has been patterned using the EHL technique and shown to make structures that can work as vertical field effect transistors. This method provides a promising route for a simple, cost effective and large area patterning of CPs, showing many opportunities for high resolution structures with applications in the nano and bio-technology fields for devices. The cost could be considerably lower than the traditional silicon electronics manufacture presently used with an advantage of flexible electronics. A solid electrolyte gate

system will need to be found to make the flexible, cheap PPy electronics feasible. In this test setup the performance is not comparable to today's silicon technology, but with more development and smaller structures it may be possible to create useable, flexible and cheap electronics that could compete.

Chapter 5

Development of a Miniaturised Portable Raman Set-Up

To be able to identify unknown materials is of major importance for a broad range of applications including for instance, homeland security or water pollution. In particular, detecting disease indicative biomarkers at very low levels in human biofluids for correct diagnosis and treatment of various conditions is a priority as we progress through the 21st century.

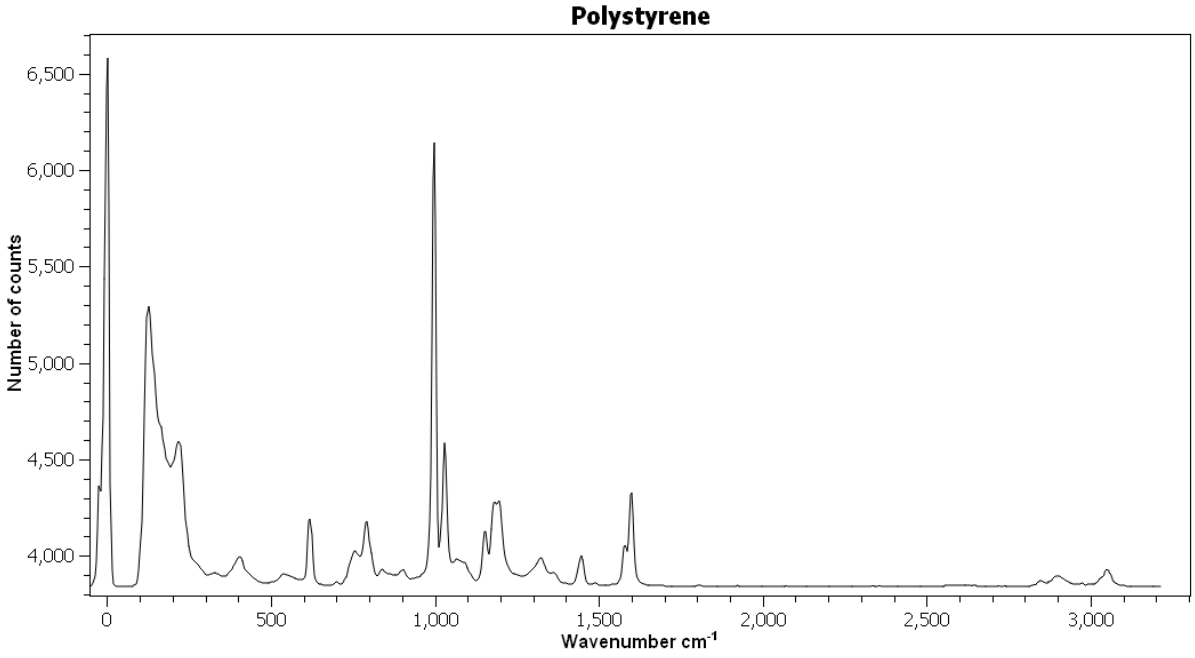

Figure 5.1: A typical Raman spectrum of polystyrene showing the representative peaks at given wavenumber versus the number of photons collected. Only Stokes shifted wavelengths are shown representing light that has lost energy. Collected using an In-Via Reneshaw Raman spectrometer using a 785nm laser.

5.1 From Raman to SERS

Raman spectroscopy with its narrow peaks of identification of bonds has the potential to tackle these challenges. When a monochromatic light is shone upon a substance, it is scattered by the bonds and atoms within the material, changing the frequency of a small number of the photons that have been scattered. This Raman scattered light contains information about the molecules that it has interacted with, giving specific fingerprint peaks in the collected spectrum to specifically identify the material and bonds comprising it (Figure 5.1). Samples analysed *via* Raman can be solid, liquid or gas as well as in a hot or cold states. The photons of light can interact with the material by scattering at the same frequency, by gaining or losing some energy or by passing straight through with no interaction.

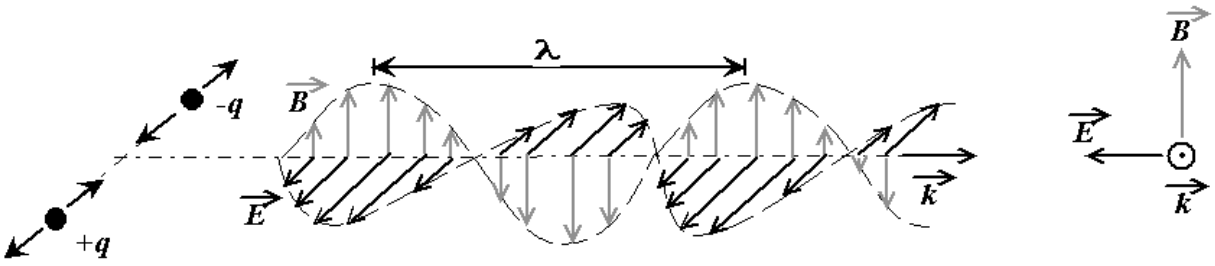

Figure 5.2: A light wave of electromagnetic radiation (EMR) can be viewed as a self-propagating transverse oscillating wave of electric and magnetic fields. A plane, linearly polarized wave is depicted propagating from left to right (X axis). The electric field is in a vertical plane (Z axis) and the magnetic field is in a horizontal plane (Y axis). The electric and magnetic fields in EMR waves are always in phase and at 90 degrees to each other [127].

Light is comprised of electromagnetic radiation comprised of waves of an electric field and a magnetic field that are perpendicular to each other (Figure 5.2).

Optical Raman spectroscopy is typically performed over a range of wavelengths between 266nm [129] to 1064nm [130]. When this light is shone upon molecules most of it is elastically scattered however, while its direction of travel is changed, its frequency remains the same, known as *Rayleigh Scattering*. However a very small proportion, roughly $1x10^{-6}$, of the photons of light interact with the molecules or atoms, either gaining or losing some energy, inelastically scattered, changing the direction and frequency of those photons. Since the frequency, F, of light equals the number of waves that pass a certain point in 1 second and the speed of light, C, is $3x10^{10}$ cm/s, dividing it by the wavelength, λ, yields the frequency relation to the wavelength Equation [51].

$$F = \frac{C}{\lambda} \quad [51]$$

Using Raman spectroscopy we measure the peaks in the spectra as a function of changes in energy rather than the exact frequency number. Therefore, we can generate similar looking spectra, independent of the exact wavelength of the incident monochromatic light used. Thus, we use wavenumber, $\tilde{\nu}$, which is inversely proportional to the wavelength and measured in cm^{-1} as given in Equation [52].

$$\tilde{\nu} = \frac{1}{\lambda} \quad [52]$$

A monochromatic light source, generated by a laser is typically used for Raman spectroscopy. This single frequency of radiation irradiates the sample and it is the radiation scattered from the molecule with a difference in vibrational energy from the incident beam which yields the Raman signal. Raman scattering does not require the

incident radiation to match the energy difference between the ground and the excited energy states. In Raman spectroscopy, the chromatic light interacts with the molecule, distorts and polarizes, the cloud of electrons around the nuclei of the molecule or atom to form a short-lived virtual state, which is not stable, and the photon is rapidly re-radiated. If no energy is lost or gained in this process, elastic scattering, then the photon is re-emitted in a different direction but with the same energy, *i.e.,* Rayleigh scattered. If the incident photon distorts the electron cloud, then energy can be given to the photon or taken from it. This scattered photon is known as Raman photon. The amount of Raman scattering depends on the polarizability, *i.e.,* how easily can it be distorted, of the electron cloud of the molecule, which is the ability of the oscillating electric field of the photons of monochromatic laser light to induce a dipole moment in the electron cloud of the molecule. These distortions and vibrations of the electron cloud are not linear and they happen in specific steps of quanta, which mean that when we collect the different frequencies of the scattered Raman light, we obtain certain frequencies which are not random but correspond to certain bonds within the given material. Since at room temperature most molecules will be in the lowest vibrational level, the Rayleigh scattering will be the most intense as the majority of the photons scatter this way and there is no energy change with the light being emitted at the same energy level. The photons that have lost energy are known as ‘Stokes’ shifted and the photons that have gained energy are known as ‘anti-Stokes’ shifted. At room temperature, the anti-Stokes lines will have a lower intensity than the Stokes lines due to the majority of the molecules starting at the lowest energy level. However, to get an anti-Stokes scattered photon, the molecule must start at an excited energy state and return to a lower energy level,

being able to give energy to the incoming photon. Therefore, there will be less anti-Stokes scattering compared to the Stokes scattering. Using classical theory we can explain most of the Raman band intensities. The electric field of the incident photon must be able to induce a dipole moment to enable scattering. The dipole moment of the molecule,P, caused by an external electric field, E, can be given by Equation [53]

$$P = \alpha E \qquad [53]$$

The polarizability, α, describes how easily the electron cloud around a molecule or atom can be distorted. The polarizability must always change during the vibration to yield the Raman scattering. Polarizability of the molecules also depends on the orientation due to the molecule's symmetry. Raman scattering can occur with a change in rotational, vibrational or electronic energy (Figure 5.3).

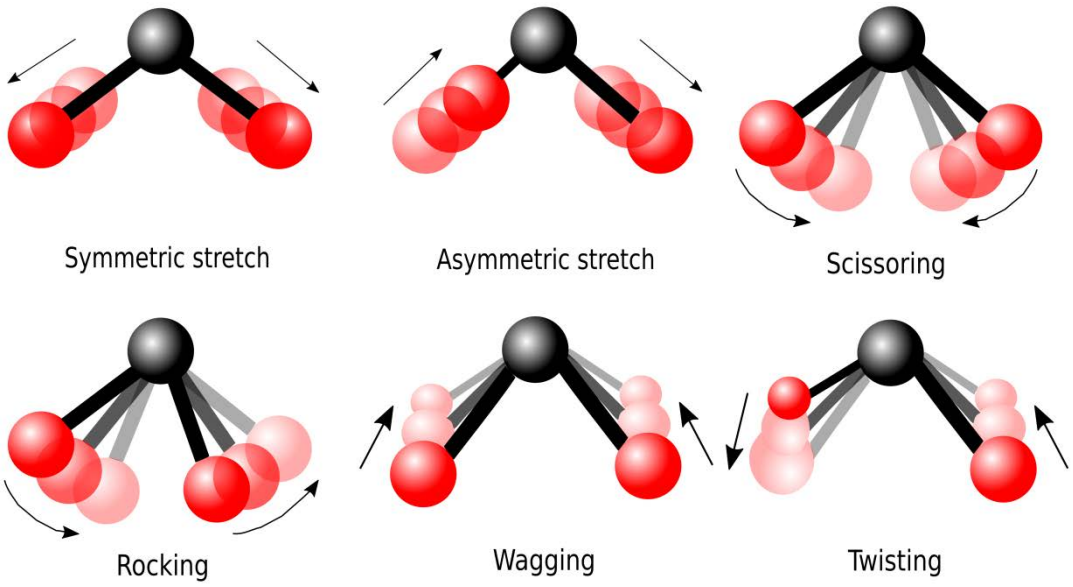

Figure 5.3: Molecular bending and stretching vibrations.

All vibrational movements of the molecule can be described as linear combinations of vibrational normal modes. A molecule has a total of 3N degrees of freedom, where N is the number of atoms in the molecule. This is because each atom in a molecule can move in three different directions (x, y, and z) (Figure 5.3) [131]. There are three movements when all the atoms in the molecule move in x, y or z direction at the same time and there are three rotational possibilities around x, y or the z-axis. Linear molecules have two axes that are perpendicular to the molecular axis that are the same. The rest of the movements are vibrational. Therefore, for linear molecules there are 3N – 5 variations and for non-linear molecules there are 3N – 6 variations [131].

For the Raman scattering to occur, the derivative of polarizability over the normal position coordinate, *Q*, must not equal zero Equation [54]

$$\frac{\partial \alpha}{\partial Q} \neq 0 \qquad [54]$$

Equation [55] describes the polarizability at equilibrium, α_0, at a distance ΔQ away from the molecules' equilibrium geometry

$$\alpha = \alpha_0 + \left(\frac{\partial \alpha}{\partial Q}\right) \Delta Q \qquad [55]$$

The derivative equals the change in polarizability as a function of the position. If the molecule is vibrating or rotating in a sinusoidal way, then ΔQ can be written as Equation [56] with the frequency of the vibration as v, time as t and Q_{max} representing the maximum vibrational amplitude

$$\Delta Q = Q_{max}\, Cos(2\pi vt) \quad [56]$$

The incident light, V_{inc} , induces an electric field,E, which is also sinusoidal with E_{max} being the maximum electric field frequency

$$E = E_{max} COS(2\pi V_{inc}\, t) \quad [57]$$

We can now substitute Equation [57] into Equation [53] yielding,

$$P = \alpha_0 E_{max}\, COS(2\pi V_{inc}\, t) + E_{max} Q_{max} \left(\frac{\partial \alpha}{\partial Q}\right) Cos(2\pi vt) COS(2\pi V_{inc}\, t) \quad [58]$$

Using the product of two different cosines as we have in the second term of Equation [58], we can further substitute the second term in Equation [58] to yield,

$$P = \alpha_0 E_{max}\, COS(2\pi V_{inc}\, t) + \frac{E_{max} Q_{max}}{2} \left(\frac{\partial \alpha}{\partial Q}\right) (Cos(2\pi t(V_{inc} + v\,)) COS(2\pi t(V_{inc} - v\,))). \quad [59]$$

Looking at the terms in Equation [59], it is clear that in the second term there are two cosines, the one with $V_{inc} + v$, showing the outgoing scattered photon which increases in frequency by v which is the frequency of the molecular motion of the anti-Stokes scattering and the second cosine, which has $V_{inc} - v$ showing a scattered photon losing a certain frequency v of the Stokes scattering. Therefore, if the integral $\left(\frac{\partial \alpha}{\partial Q}\right)$ equals zero, then the whole second term also equals zero and thus, there will be no Raman scattering. However, when the integral of polarizability does not equal zero, there will either be a loss or gain in the frequency of the scattered photon, yielding the Raman scattering.

Large atoms like Radon are strongly polarizable as their electron clouds are far away compared for instance, to Helium, which has a low polarizability, due to the

electrons being close to the nucleus and thus making it harder to distort the electron field. Polarizability of individual atoms is isotropic, *i.e.,* it is the same in all directions. Scattering intensity is proportional to the square of the polarizability derivative. If the polarizability derivative is close to zero, then the intensity of the Raman band will be low. On the other hand, if the scattered photon loses some energy, then the difference in wavelength from the incident photon is designated as Stokes shifted, named after Sir George Stokes who explained the occurrence of fluorescence [132]. If the scattered photon gains energy, then the difference in wavelength is designated as an anti-Stokes shift (Figure 5.4).

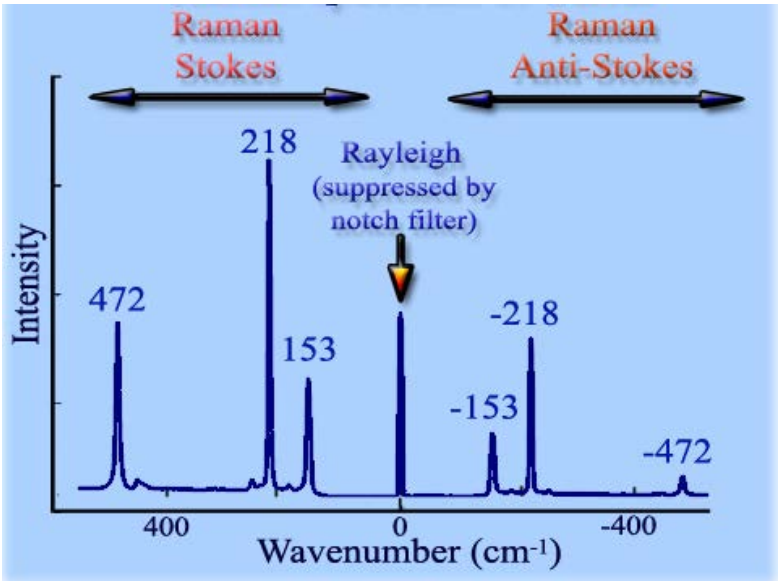

Figure 5.4: Raman spectrum of sulphur at room temperature showing the Stokes lines and the Anti-Stokes lines. It is clear that the Stokes lines have a higher intensity compared to the Anti-Stokes ones. Adopted from reference [126]. The peaks plus and minus at 472 represent the S-S bond stretching and the plus and minus 218 and 153 are both S_8 crystal bending indicating that sulphur is a type of rhombic crystal [128].

However, the classical theory cannot explain the differences between the intensities of the Stokes and Anti-Stokes lines and therefore, Quantum Theory is required. We use electronic and vibrational energy states to explain the differences in

intensities. The majority of the molecules at room temperature are at the ground state and since the molecules are required to be in an excited state to get to the Anti-Stokes lines, a considerable lower proportion of the Anti-Stokes scattered photons is observed in comparison to the Stokes scattered ones (Figure 5.5). The intensities of the Raman lines represent the proportion of the Raman active molecules in each sample. Importantly, since the Raman Effect depends on the polarizability of the molecule, it can yield Raman scattering from a molecule that has no net dipole moment.

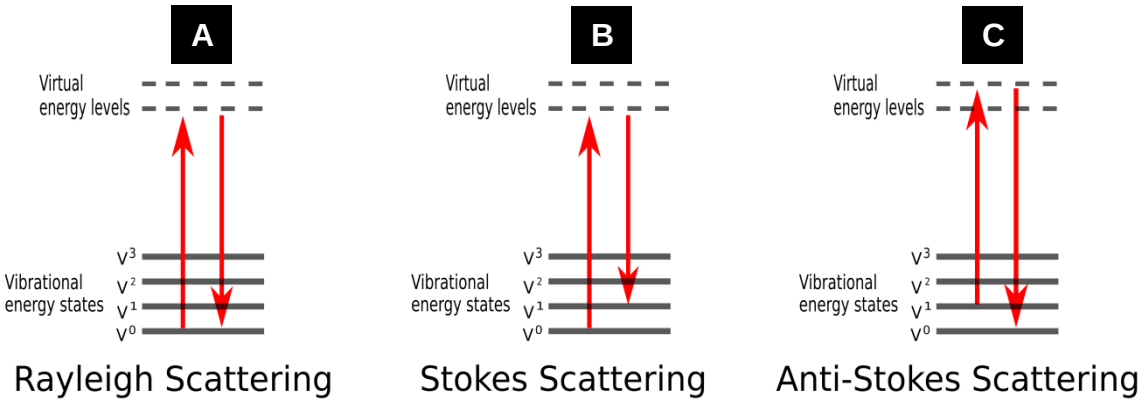

Figure 5.5: Schematic diagram showing the molecular bond energy levels are quantised and thus, (A) the incident photon lifts the energy state of the molecule to a high virtual energy level and immediately radiates a photon with the same energy as the incoming photon, known as Rayleigh scattering. (B) The incoming photon raises the energy level of the molecule to a high virtual energy level and then the molecule emits a photon with less energy than the incoming photon, leaving the molecule at a higher energy state than before the interaction, and the emitted photon has a lower frequency, *i.e.,* Stokes shifted. (C) The molecule is already above the ground state and the incoming photon raises the molecule to a higher virtual energy state. The molecule emits a photon and goes to the ground state, giving additional energy to the exiting photon providing it with a higher frequency. Photons with the higher energy are known as Anti-Stokes shifted.

For a scattering event to happen the energy of the incident photon does not need to be equal to a discreet energy level of a molecule. Yet, as the energy level of the incident photon approaches the discreet energy levels above the ground state of the molecule, the intensity of the scattered light increases as resonance occurs.

5.2 Theoretical Background of Surface Enhanced Raman Scattering (SERS)

The surface enhancement of the Raman signal was first discovered in 1973, however, it was not properly understood and was predominantly hypothesised that the enhancement was due to having a larger surface area [133]. In 1977, two competing explanations were proposed for the enhancement showing that the dominant factor was not the larger surface area but it was due to the true enhancement of the Raman scattering signal. The first explanation put forward was the 'Chemical Theory' proposed by Grant Albrecht and Alan Creighton [134]. Their theory suggested the formation of charge-transfer complexes which only happen for molecules that have formed a chemical bond with the surface. But it could not explain the observed signal enhancement for molecules at a distance from the surface. Such enhancements could be possibly explained by the second theory, the 'Electromagnetic Theory', proposed by David Jeanmaire and Richard van Duyne [135]. According to this theory, when the photons of light from the laser hit the metal surface they excite surface plasmons which in turn, can enhance the electric field of the photons. The enhancement is the largest when the wavelength of the incident photons is in resonance with the plasmon frequency. The exact reason for metals to yield such a high enhancement of the Raman signal is complex and is still a matter of debate and continually investigated [136] [137]. However, it is agreed that the main effect of the enhancement arises due to three reasons: It is an electromagnetic effect of (1) resonance with surface plasmons between the molecule and the metal surface, (2) from molecular resonance within the molecule and (3) from charge transfer

resonances between the molecule and the metal. These are the main effects that couple together to give the Raman enhancement [138]. To achieve a good surface Raman enhancement a noble metal nano-structured surface or nanoparticles are required. There are currently three main types of SERS substrates. The first is metal nanoparticles in a suspension, the second is metal nanoparticles immobilized on a substrate and finally, nano-structured surfaces, either directly fabricated on a metal substrate or initially made from a non-metallic material and then coated with a thin layer of a noble metal. The most common metals to use for SERS substrates are gold [139], silver [140] and copper [141]. However, there are inherent problems with using nanoparticles as SERS active platforms, whether in suspension or immobilized on a substrate, in the fact that the areas of high enhancement, known as 'hot spots', generated between two adjacent nanoparticles are random and irreproducible and thus, making it highly challenging to get a consistent enhancement, rendering these nanoparticles not suitable for bio-diagnostic tests. In contrast, homogeneous, reproducible lithographically structured surfaces can yield a considerably more consistent enhancement, are easier to integrate within microfluidic devices and more robust, rendering them more suitable candidates for SERS-based biomedical diagnostics. The high-enhancement of the Raman signal can be achieved by using consistent metallic substrates, substantially improving the signal, exhibiting low-sample detection variability, no aggregation and an excellent batch-to-batch repeatability.

5.3 Towards a Novel, Advanced and Portable SERS System for PoC Diagnostics

For the development of a small portable point-of-care technology to be integrated with our novel microfluidic SERS active lab-on-a-chip, a bespoke Raman spectrometer device is required. This following part is focussed on the development, iteration and optimisation stages of our innovative, miniaturised optical set-up.

Initially, an Inphotonics Inc InPhochelle spectrometer was purchased, which has a high resolution of 2cm^{-1} across the full spectral range of 200-3500cm^{-1}. The spectrometer is also a relatively small size. The supplied Raman probe from Inphotonics Inc was exploited for integration with our optofluidic chip by being integrated into a collection box with a narrow webcam microscope built in to monitor the beam position and focus as shown in Figure 5.6.

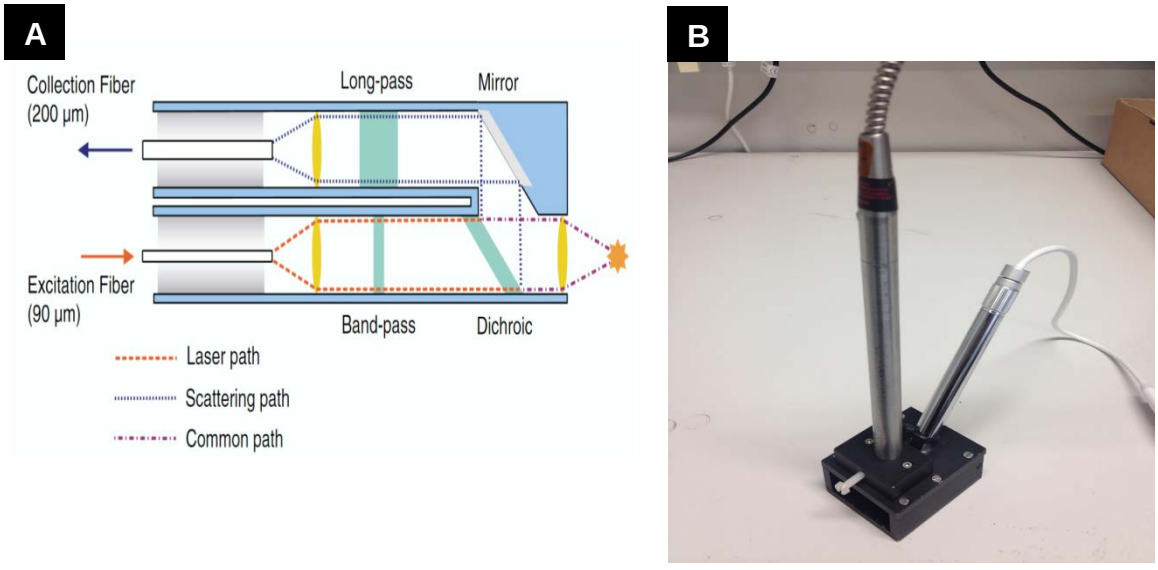

Figure 5.6: (A) Schematics of Inphotonics Inc. Raman probe design. Adopted from http://www.inphotonics.com/technote13.pdf (B) Photograph of our first iteration with the Inphotonics probe mounted in a collection box with a narrow webcam microscope.

Unfortunately however, the laser probe size was too large to work optimally with our Reproducible electrohydrodynamically surface enhanced Raman substrates (RED SERS). Consequently, the collection part of the spectrometer set-up had to be custom designed and fabricated in order to match up with the requirements of our SERS substrate which is incorporated within a microfluidic chip. The initial idea of this second iteration was to use a microprobe fibre optic design. In this design, we exploited a 50µm fibre, purchased from Edmund Optics Ltd, to deliver the laser beam to the sample. The laser fibre was surrounded by five 200µm collection fibres, also purchased from Edmund Optics Ltd, I encased all these in a stainless steel tube with a 1.5mm inside diameter (Figure 5.7) and hand polished the front surface using fibre optic polishing paper, purchased from Premier Farnell Limited.

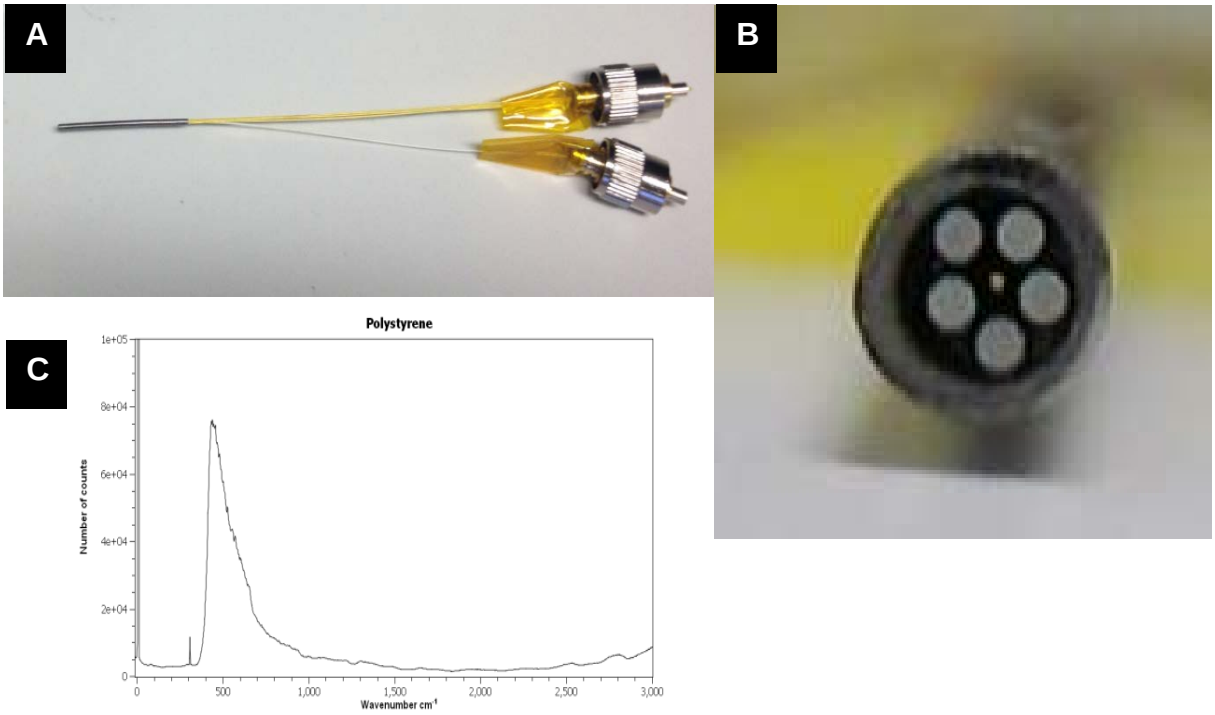

Figure 5.7: (A) Photograph of the fibre optic probe including the metal tube with five collection fibres connecting to an FC fibre optic connector and a single laser in fibre also connected though an FC connector. (B) A photograph of the front of the probe with a single 50 micron fibre which delivers the laser to the sample surrounded by five 200µm collection fibres encased by epoxy inside the metal tube. (C) A Raman spectrum of polystyrene with the Raman signal from the walls of the fibres overwhelming the signal from the polystyrene sample, making this setup unusable for Raman detection of samples.

The optical fibres were glued into optic FC connectors, purchased from Premier Farnell Limited, and I polished the ends using fibre polishing paper. The FC connectors allowing connection to the laser diode box and for the collection fibres to be connected to a notch filter unit, which blocks the Rayleigh scattered signal yet, allows the Raman scattered, Stokes, light into the spectrometer.

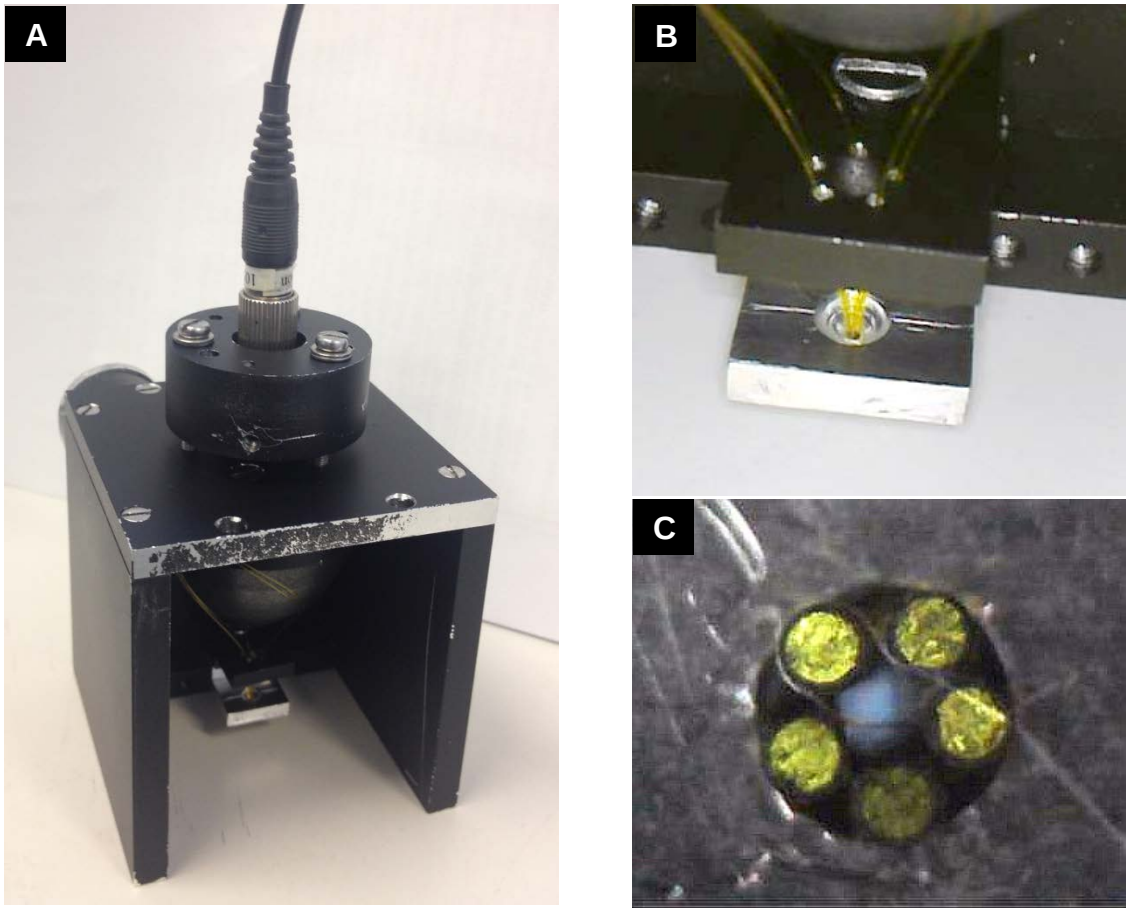

Figure 5.8: (A) Raman collection setup with laser coming in at the top enabling position adjustment. The laser passes through a lens and then a band pass filter housed in the laser exit cone to clean up the laser signal removing any Raman signal generated in the connecting fibre. (B) Photograph of the collection fibres housed through a supporting bar which holds the fibres in position. The fibres are then held in a hole with a particular size which allows only one configuration that the fibres can be located, which is around the edge of the hole leaving a small gap for the laser beam. (C) A photograph showing the fibres organised around the edge of the hole leaving a small gap in the middle.

While this setup was producing a reasonable output, there was no space to fit a band pass filter on the laser exit fibre, meaning that by the time the laser hit the sample it has also picked-up a significant amount of Raman signal from the fibre itself. Subsequently, the signal from the fibre swamps the signal from the sample making the setup unusable (Figure 5.7C).

The next iteration of Raman collection setup exploited a smaller amount of optical fibres to reduce the amount of Raman signal from the fibres themselves. Since the highest Raman signal from the fibres arises due to the high power of the laser in the fibre which delivers the laser to the sample, it was logical to remove this fibre and instead use lenses to focus the laser beam directly onto the sample (Figure 5.8). The laser remains connected to the setup *via* a fibre but housed in the cone that the laser beam passes through is a lens to focus the beam onto the sample and a 785nm band pass filter that removes any Raman signal generated in the connecting fibre, yielding a 'clean' 785nm light. The cleaned up focussed laser beam then passes through a gap in the middle of the five collection fibres, which are arranged in a pentagon shape, dictated by the size of the hole that the collection fibres sit in allowing only this configuration for the fibres (Figures 5.8 B and C).

The sample is located underneath this assembly and the reflected Raman signal is collected by the five, 200µm collection fibres which then direct the collected light back to ,and through, a 785nm notch filter, eliminating the Rayleigh scattered signal yet allowing the Raman signal to pass through (Figure 5.9 A). The light subsequently is directed through an FC connector straight into the spectrometer. Unfortunately, holding the fibres in the correct position with a clear hole in the middle proved very difficult to fabricate and thus, a further modification was applied to the

setup (Figure 5.9 B and C). This time, the optical fibres were held in place by a holding bar with a 300µm hole in the middle for the laser beam to pass through, surrounded by five 300µm holes to hold the collection fibres. Nevertheless, it was highly challenging to drill these 300µm holes at the exact required position. A very small, dedicated, drill was used for this purpose spinning at a very high speed combined with a microscope bolted onto the side to be able to observe the movements of the drill *in-situ* (Figure 5.10 B). It is important to note, that the 300µm drills are extremely flexible and thus they wander when trying to drill in a specific spot and also even the slightest pressure would bend or break them.

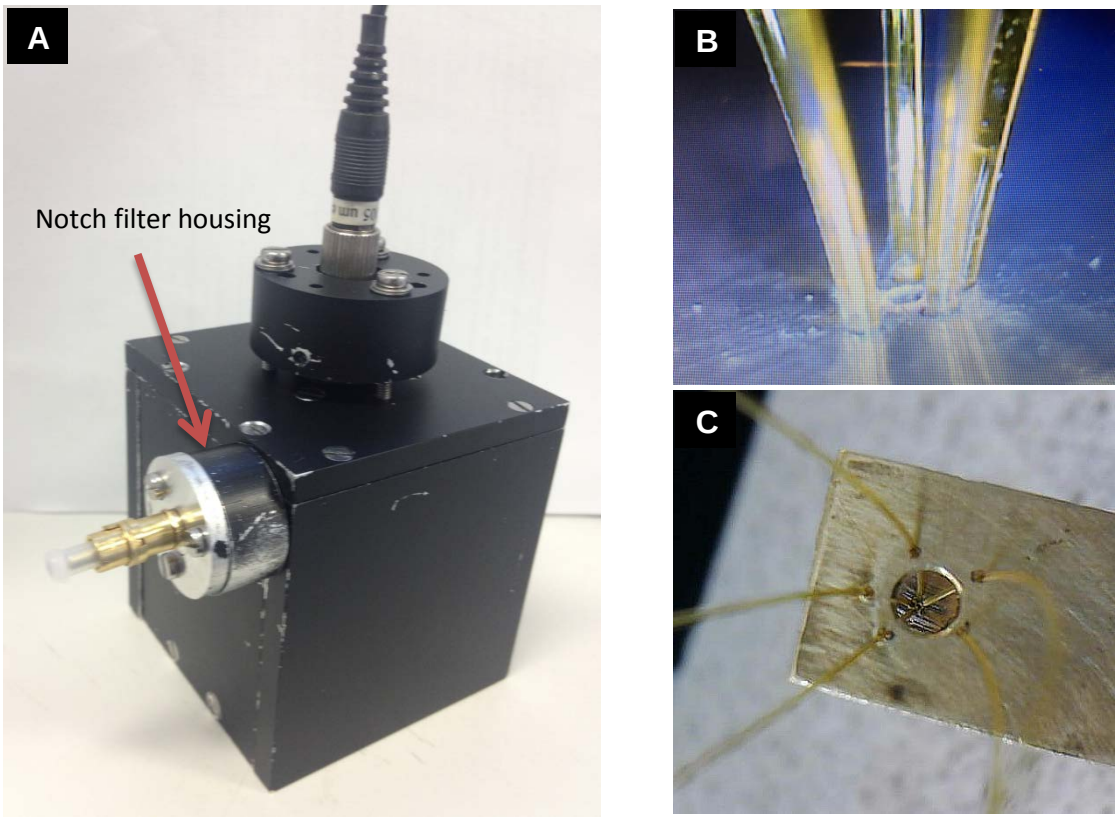

Figure 5.9: Photographs of: (A) of the back of the Raman collection setup showing the FC connector that plugs directly into the spectrometer. The arrow indicates the notch filter housing. (B) the modified fibre holding bar with a 300µm hole in the middle surrounded by five 300µm holes to hold the collection fibres in position and (C) top-view through the holding bar into the collection bar with five fibres going through 5 holes and a centre hole of 300µm for the laser beam.

However, despite the described modifications, this optical set-up did not yield the desired outcome either. The covering of the collection optical fibres was damaged by the sharp edges of the 300µm holes. Also, since the five collection holes were not all at the same distance from the central laser hole, there was no consistent collection angle of the reflected scattered light (Figure 5.10 C). Moreover, in this arrangement there was still quite a large Raman signal from the collection fibres, due to the intensity of the scattered Rayleigh light creating fibre Raman signal in the collection fibre.

Figure 5.10: Photographs of (A) the fibre optic arrangement with a top bar supporting the fibres coming in and allowing the laser beam through without any fibres getting in the way; (B) the fibres coming through the 300µm holes in the exit bar and also demonstrating the damaging of the outer covering of the fibres by the sharp edges of the holes and (C) the polished fibres where the five collection holes are not perfect in distance from the centre laser hole, resulting in a non-consistent collection angle.

To make this setup functional, the notch filter would need to be placed right under the collection fibres with a small hole drilled in the middle of the filter to allow the incoming laser through, which is a highly challenging task to achieve without damaging the filter. It was therefore, decided to almost completely re-design the set-up in order to overcome the above described issues (Figure 5.11).

In our most recent design, in order to collect the Raman spectra from whole human blood, I milled and turned an optical Raman collection setup from aluminium to host the filters and mirrors and these parts were further integrated with 12mm lens tubes (Thorlabs) used to connect the parts together and house the lenses.

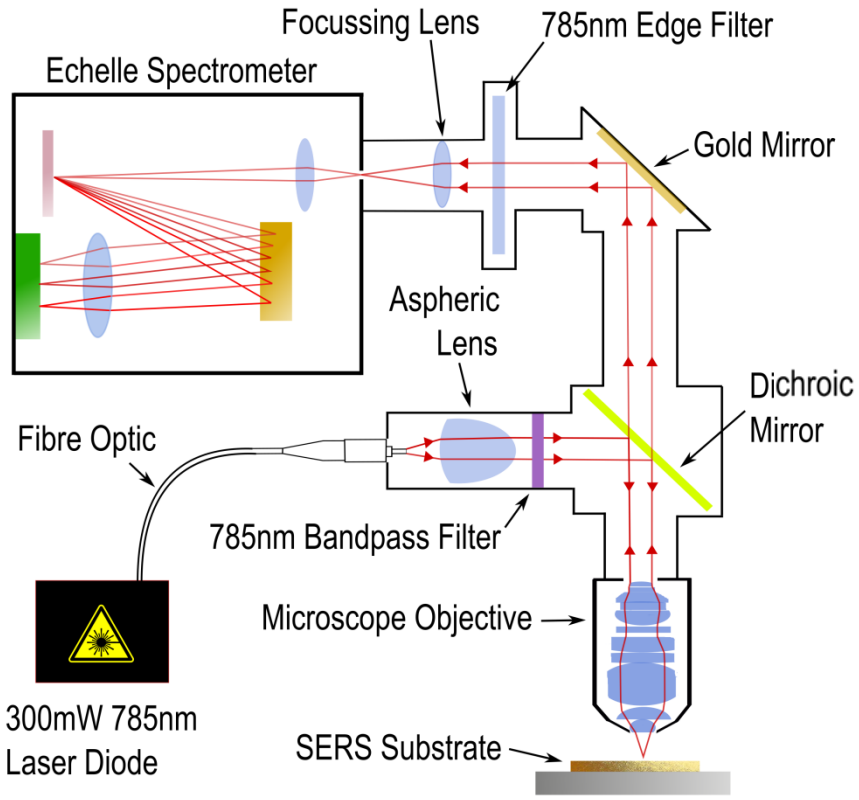

Figure 5.11: Schematic diagram of the final Raman collection setup. The 300mW diode laser is connected to a lens tube via a fibre optic. The beam is collimated by an aspheric lens and passes through a 785nm bandpass filter. The beam is then reflected down by a dichroic mirror and through a microscope objective lens which focuses the laser beam onto the sample. The reflected light is then collected by the objective lens and the collimated beam is then reflected towards the spectrometer by a gold mirror at 45°. The beam then passes through a 785nm edge filter to block the Rayleigh and anti-Stokes signal. The beam is then focussed into the spectrometer by a long focal length lens. microscope objective lens which focuses the laser beam onto the sample. The reflected light is then collected by the objective lens and the collimated beam is subsequently, reflected towards the spectrometer by a gold mirror at 45°. The beam then passes through a 785nm edge filter to block the Rayleigh and anti-Stokes signal and finally, focussed into the spectrometer by a long focal length lens.

A 300mW 785nm LML series laser diode unit (PD-LD Inc) was then connected to a lens tube *via* a fibre optic cable. The laser light from the end of the fibre optic was focused to a collimated beam by an aspheric lens (Thorlabs). This collimated beam is reflected downwards by a 785nm dichroic mirror, (Semrock Inc) and subsequently then focused to a spot on the RED-SERS substrate within the microfluidic chip by an Olympus 20x microscope objective lens which has a fixed focus distance of 1.2mm. The beam interacts with the sample, with the majority of the light being scattered with the same frequency as the incoming light, *i.e.,* Rayleigh scattered. A small proportion of the incoming photons of light, roughly 1 in 10 million, interact with the electron clouds of the molecules and give up or receive a certain amount of energy, changing the frequency of the scattered photons, *i.e.,* Raman scattered light.

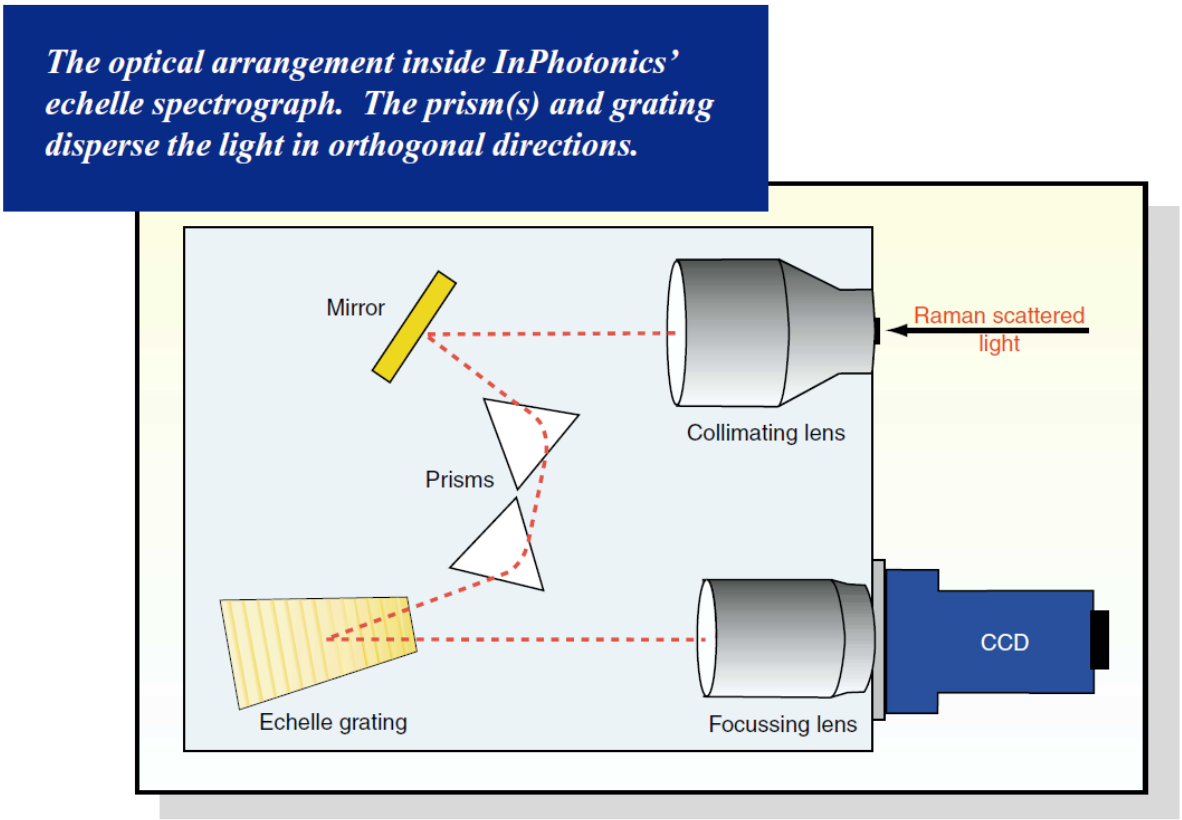

Figure 5.12: Schematic diagram of Inphotonics Inphochelle spectrometer, from Inphotonics Inc, demonstrating prisms splitting the light followed by the echelle grating splitting the light once again into a ladder format onto the 2D CCD.

This reflected scattered light is collected by the microscope objective lens and collimated. The light then travels back through the dichroic mirror until it is reflected towards the spectrometer by a gold mirror. The beam is subsequently focussed by another lens, with a long working distance, into the spectrometer. Before the light beam reaches the spectrometer, it is passed through an edge filter to block wavelengths of 785nm and shorter, removing the Rayleigh scattered light signal and the anti-Stokes shifted light while allowing the Stokes shifted Raman signal to pass. The focused light enters the Inphotonics InPhochelle spectrometer, where the different frequencies of the Raman light are spread apart and collected onto a CCD detector. The echelle spectrometer has explicit advantages over other types of spectrometer in particular, enabling a high resolution over a full spectral range, with the spectrometer having a small footprint.

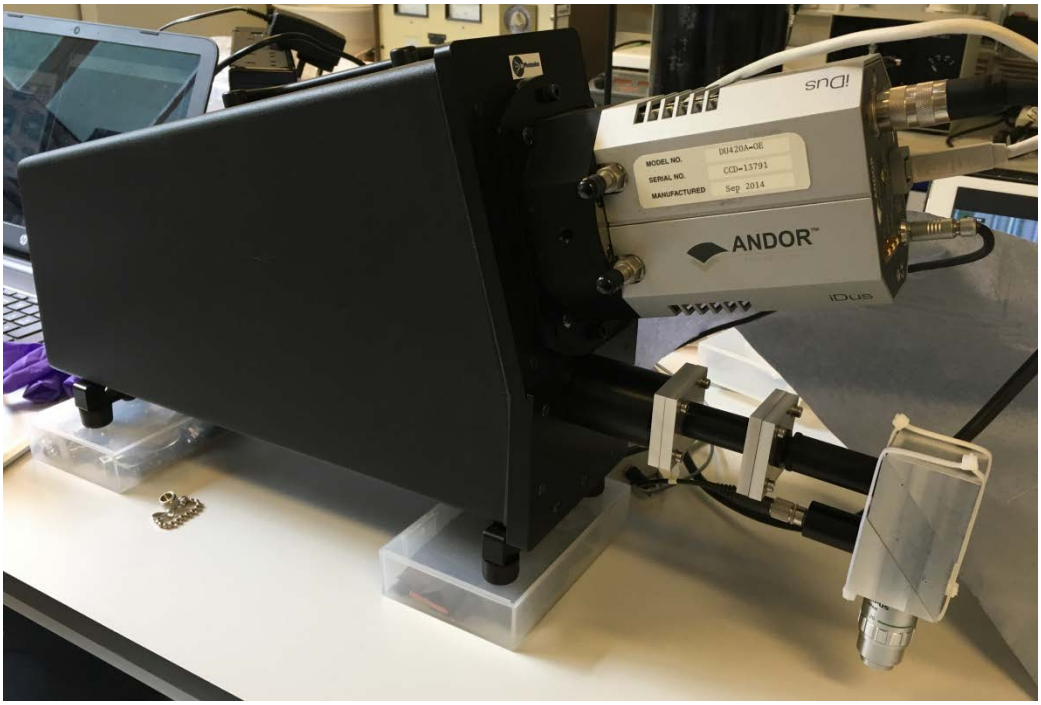

Figure 5.13: Photograph of the overall Raman setup. The echelle spectrometer is on the left hand side with the Raman collection setup machined from aluminium on the right hand side. The Andor cooled CCD is visible in the top right hand corner.

The principal of this is based on using a lens to collimate the incoming beam, passing it through a prism to disperse the different light frequencies and then, dispersing the light further using an echelle grating. This consequently, has the effect of breaking-up the light spectrum into parts and stacking, spreading the highly dispersed light in a ladder type manner over a 2D CCD detector, and therefore yielding a high resolution over a large spectral range, down to 2 cm^{-1} across the full spectral range 200-3500cm^{-1} (Figure 5.12).

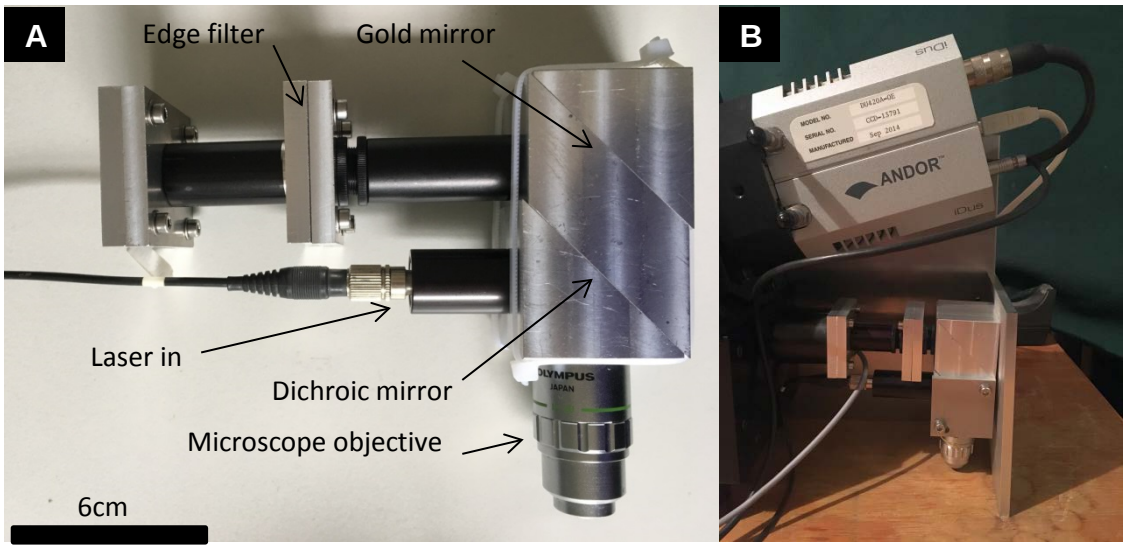

Figure 5.14: (A) A photograph of our novel miniaturised Raman prototype collection head with arrows indicating the positions of the dichroic mirror, the gold mirror and the edge filter. (B) Photograph of the developed and engineered Raman collection head connected to the echelle spectrometer.

In summary, through several iterations of the portable Raman, described in this chapter, designed and engineered specifically for the applications in point-of-care biodiagnostics, we have developed a prototype of miniaturized Raman system aimed for multiplexed and high-throughput analyses of disease indicative biomarkers. Our most-up-to-date system currently uses a 785nm diode laser, fed down an optical fibre and passed through a collimating lens and subsequently, the beam is reflected from

a dichroic mirror down through a 20x microscope objective onto the SERS active substrate which will be described in details in Chapter 6. The scattered beam is reflected back up through the microscope objective lens and passes through the dichroic mirror and onto a gold coated mirror that reflects it through a lens and focuses the beam onto the slit of the spectrometer. In between the spectrometer slit and the focusing lens a 785nm edge filter is located to block the 785nm Rayleigh scattered light yet, allow the longer wavelength light through. The different wavelengths of light are then spread apart within the echelle spectrometer and collected on the cooled CCD detector with the information being sent to laptop to display the collected spectra.

The acquired SERS spectra, using the prototype system, which are broadly presented and thoroughly discussed in Chapter 6, can be rapidly compared to the pre-established finger prints of the biomarkers pool, acquired with the commercial lab-based Raman system (Renishaw Plc.), enabling identifying the presence of disease indicative biomarkers. Further optimisation steps, envisioned for our portable Raman system are outlined and discussed in Chapter 7.

CHAPTER 6

Micro-optofluidic Engineered Device Technology for Biodiagnostics of Traumatic Brain Injury

We have produced a label-free, high-throughput miniaturised device technology for the detection of neurological biomarkers as representative of TBI and related neuro-pathophysiological processes in blood plasma at trace-level concentrations. Our development combines advanced, controllable and reproducible electrohydrodynamically (RED) fabricated optofluidic lab-on-a-chip engineered for multiplexed-SERS detection with superior sensitivity to achieve a fully integrated miniaturised sensor for timely diagnosis enabling treatment of TBI scenarios. Detection of TBI-indicative biomarkers *via* MEDTech in conjunction with clinical evaluation can provide critical information for the stratification of patients and enable a sophisticated assessment of the primary TBI severity at a much lower cost than a CT-scan, while reducing the cost and radiation exposure. It can also provide monitoring of brain-injury and risk of neurological deterioration that would help avoid long-term deficits and morbidity, from just a pin prick of blood.

6.1 Introduction

Healthcare is in the middle of revolutionising technologies transforming point-of-care (PoC) medical diagnostics. More and more often, diagnosis is taken out of the medical laboratories and happens at the point-of-interest *i.e.,* at a location of the patient. The tests are simple and quick and typically, exploit advanced and miniaturized devices that can be used at a doctors' surgery, at a roadside accident, on the sporting field, in the hospital or even at home. A number of common PoC diagnostic tests are already in use including for instance, urine pregnancy test [143], blood glucose tests for diabetics [144] and heart rate monitors for cardiovascular diseases [145]. Nevertheless, there is still an unmet clinical need for more quick and accurate diagnosis of many diseases and conditions at PoC to allow the correct rapid treatment and disease management to be chosen for the patient in need, while saving thousands of lives per year, time and money as well as reducing expenses and burden on the national health care system (NHS). With this in mind, in this study, we have designed and developed an innovative PoC test based on advanced surfaced enhanced Raman scattering substrates embedded within a microfluidic chip for timely and cost-effective diagnosis of traumatic brain injury.

The aim of this research was to create a miniaturised, portable device technology that will use just a pin prick of blood inserted into a microfluidic chip to split the blood into several constituent parts and pass these over special SERS-active substrates located within the optofluidic lab-on-a-chip. The microfluidic chip is then inserted into a compact Raman device, development of which is described in Chapter 5, where a laser beam excites the substrates yielding the Raman surface

enhancing of the signal from the molecules present in the sample. The Raman scattered light is then collected in a spectrometer and the spectra are analysed with an appropriate software yielding an indicative parameter of whether the patient has sustained traumatic brain injury and how severe the brain trauma is, allowing the correct treatment to be chosen for the patient, all achieved in only a few minutes.

Traumatic brain injury (TBI) is a leading cause of morbidity and mortality worldwide with neuro-disabilities requiring long-term care. While critical decisions affecting prognosis and treatment efficacy must be made rapidly, TBI is notoriously hard to diagnose pre-hospital and still very challenging at hospital, resulting in incorrect patient management and triaging. Timely assessment of injury severity is a priority in the management of TBI patients as every minute counts if outcomes are to be successful. However, this is poorly supported by current technologies, which fall short in the point-of-care (PoC) diagnostic needs, exhibiting poor-sensitivity, special-handling requirements and complicated, costly procedures. Previous studies have shown brain concentrations of N-acetylasparate (NAA) to be a sensitive predictor of mortality and rise in intracranial pressure in TBI [146, 147]. In this chapter we demonstrate a miniaturised platform technology for timely, sensitive and rapid PoC diagnostics of TBI indicative biomarkers, and in particular NAA. The Micro-engineered device technology (MEDTech) is based on label-free reproducible electrohydrodynamically (RED) fabricated surfaces for enhanced Raman scattering active platforms enabling versatile, tuneable, nanostructures to match the laser-excitation wavelengths to yield high signal enhancements. These, further integrated with a carefully designed microfluidic-chip to process whole blood into plasma and direct the plasma onto the SERS surfaces provide a highly sensitive, cost-effective

portable devices for direct detection of miniscule concentrations of biomarkers from biofluids, whole human blood at the moment, offering a useful clinical test that is simple, rapid and minimally invasive while being state-of-the-art to a point where biodiagnostics is feasible.

In emergency-care practice, life-critical decisions must be made within a period of minutes which influence patients' prognosis and the efficacy of treatment. Currently, over half of major brain trauma patients are over-triaged, straining healthcare resources and third are under-triaged, missing significant trauma [148] [149]. The roadside assessment of TBI is the biggest issue due to confounders *e.g.,* hypotension/hypoxia, alcohol or early intubation. The diagnosis of TBI is confirmed radiologically after admission to hospital or clinically, when sedation is stopped several days later, thus missing a critical window for early intervention [150] [151]. Stratification of TBI relies heavily on neurological imaging and invasive neuromonitoring, which are typically applied to support diagnosis and therapy. Computerised tomography (CT) scan is the current 'gold standard' for imaging, whilst magnetic resonance imaging (MRI) and its advanced applications, such as (H)-magnetic resonance spectroscopy (H^1-MRI) and diffusion tensor imaging, can provide additional information about the injury and potential for recovery [152] [153] [154]. However, these methods are not only resource-intensive, but also only feasible in a hospital setting and once the patient has been stabilised. But currently there is no biomarker test for TBI in clinical use. Therefore, there is a growing interest in TBI biomarkers to guide clinical decision making, particularly focussing on the early stages, when timely treatment is critical [155] [156]. A range of known central nervous system biomarkers are present in the cerebrospinal fluid (CSF), the composition of

which reflects biochemical changes that occur in the brain [157]. CSF however, has to be collected by a lumbar puncture, which is often unsafe in TBI patients and total unsuitable for PoC testing. While the challenges of accurate diagnosis and monitoring of TBI have created an urgent need for rapid, sensitive PoC detection of the TBI-associated biomarkers, no technology currently exists to timely diagnose neurological damage with sufficient accuracy to enable stratification of patients at risk of deterioration in the acute setting.

The use of biofluid-based diagnostic methods as representative of neuro-pathophysiological processes can offer clear advantages for the PoC diagnosis since the collection of blood samples is a standard procedure in routine clinical practise and for our setup all we require is a pin prick of blood from a finger, a very simple, quick and easy procedure. While some molecules are highly expressed in the central nervous system, key challenges associated with the use of blood-biomarkers for TBI diagnostics, include considerably lower concentrations than in CSF due to their dilution in the blood volume, the effect of the blood-brain-barrier and the effect of clearance of certain molecules from blood *via* the liver or kidneys. Over the last decade, several candidate biomarkers have emerged for clinical manifestations of TBI which have been shown to correlate with severity of neurotrauma in the hospital care environment *e.g.,* lipoproteins, glial-astrofibrillary protein (GFAP), neuron-specific enolase (NSE) and S100B [158] [159] [160] [161], yet, their value is unclear in the earliest diagnosis, pre-hospital setting. While demonstrating correlation with trauma severity and holding potential diagnostic, prognostic and stratification value, these biomarkers are released into the body fluids in miniscule amounts and are undetectable at early stages with available biochemical techniques with sufficient

timeliness and sensitivity at an affordable cost. Analysis is predominantly carried out in specialised laboratories, using mainly high performance chromatography, mass spectrometry or ELISA, requiring expensive labels for each target biomarker with time-to-results in the range of several hours or even days and requiring complex equipment, not suitable for PoC. Optical methods on the other hand, provide a route to the miniaturisation of sensing devices. Surface enhanced Raman scattering (SERS) is a highly sensitive spectroscopic technique enabling detection down to single molecule level *via* enhancement of localized optical-fields on metallic sub-microstructures, which can be tuned by manipulation of the surface roughness and architecture at the sub-micron level [162] [163]. It offers distinct advantages over other spectroscopic methods for sensing including, immediate detection of analytes without complex time consuming sample-preparation. It is also capable of detecting multiple analytes simultaneously due to the narrow bandwidth of the spectral peaks reducing the spectral peak overlap [164] [165]. SERS is the only detection technique that can be deployed out of a laboratory setting without a significant loss in performance and is capable of rapid sensing with considerably lower detection limits than any currently exploited methods. This unique set of attributes makes it well suited to address the challenges associated with PoC diagnostics for practical and sensitive detection of biochemical markers. One of the key challenges of SERS however, is the fabrication of noble-metallic structures that are highly reproducible and sensitive to the target molecules. The substrate on which SERS is performed is often the critical component for successful detection [166] [167]. Reliable, cost-effective and consistent fabrication of highly-sensitive, tuneable, stable and reproducible SERS-active structures still remains a considerable challenge. Any imperfections in substrates have a significant

effect on the ultimate response. The high-enhancement of the Raman signal is usually achieved by using random metallic nanoparticles, from which only a minute fraction exhibit SERS-activity, substantially affecting the signal, exhibiting high-sample detection variability, aggregation and poor batch-to-batch repeatability. [168] Furthermore, not only are substrates with tuneable surface plasmon resonances matching the excitation lasers needed to gain the highest enhancement, a challenging task for lab-on-a-chip systems but also, optofluidic systems have been largely based on external, bulky components requiring alignment expertise to collect the signal, rendering these difficult to use, not portable, expensive and incapable of rapid-detection. In contrast, sub-micron structures on substrates can intrinsically overcome this problem for highly-stable SERS measurements.

6.2 Reproducible Electrohydrodynamically Fabricated (RED) SERS Substrates

We have developed a lithographically defined, optimised RED lab-on-a-chip which is considerably more stable than nanoparticle-based systems. This offers more degrees of freedom in the design and tuning of structural parameters, enabling reproducible, multiplex, high SERS enhancements, as a platform for reliable, real-time diagnostic technology for rapid detection of biomarkers at *pico*molar concentrations from blood plasma after whole blood has been separated by the microfluidic chip. RED microlithography encompasses induction of amplified instabilities in thin nanofilms (Figure 6.1). Assembling a microcapacitor-like device with a thin polymer layer on a bottom electrode opposed by a second electrode, with an applied voltage across the

electrodes which gives rise to a high electric field across the dielectric material and air gap.

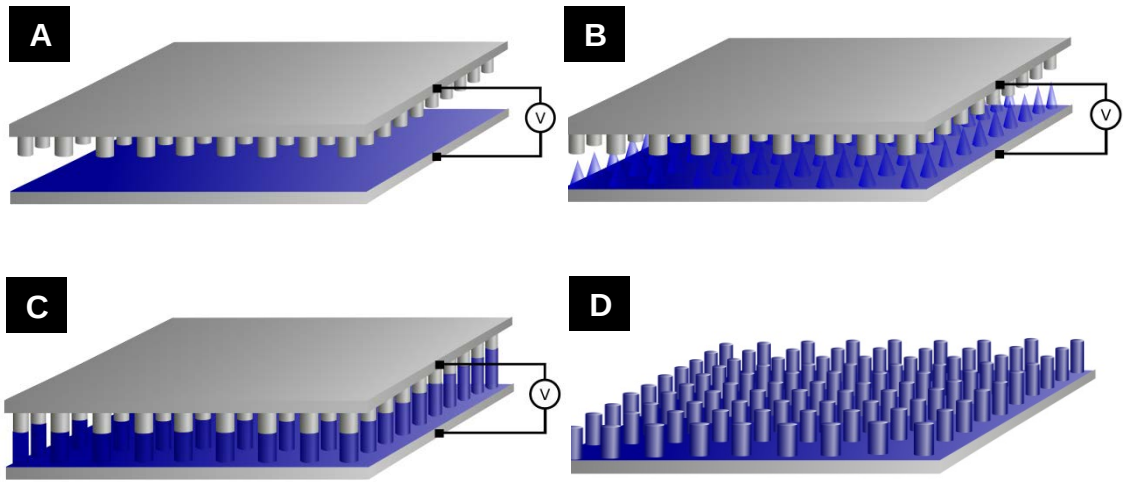

Figure 6.1: (A) Schematic diagram of the RED setup. A bottom silicon electrode is coated with a nano layer of polymer with a patterned silicon top electrode opposing. The temperature is raised above the glass transition temperature of the polymer and a bias is applied between the electrodes. (B) As time progresses the liquid polymer reaches up towards the protruding structures of the top electrode reducing the electrostatic pressure. (C) As further time progresses the liquid polymer reaches the top electrode protruding structures and replicates them. The whole setup is then cooled down to room temperature and the top electrode can then be removed (D).

The subsequent dielectric discontinuity at the interface in the capacitor triggers the formation of displacement charges, coupling to the electric field and causing a destabilizing electrostatic pressure, which eventually overcomes the stabilising forces of the *Laplace* pressure, yielding energetically more favourable configurations. Typically, the experimental set-up of the electrohydrodynamic patterning comprises a slight misalignment of the capacitor plates resulting in a wedge geometry with a variation in the electrode spacing. MEDTech is based on controllable RED sub-microstructures engineered for rapid-SERS detection. These RED-SERS active substrates are fabricated using an innovative rig combining a micromanipulator and a

piezo actuator for the finest adjustments enabling a highly parallel capacitor-like electrohydrodynamic patterning set-up for homogenous fabrication of submicron pillars (Figure 6.2).

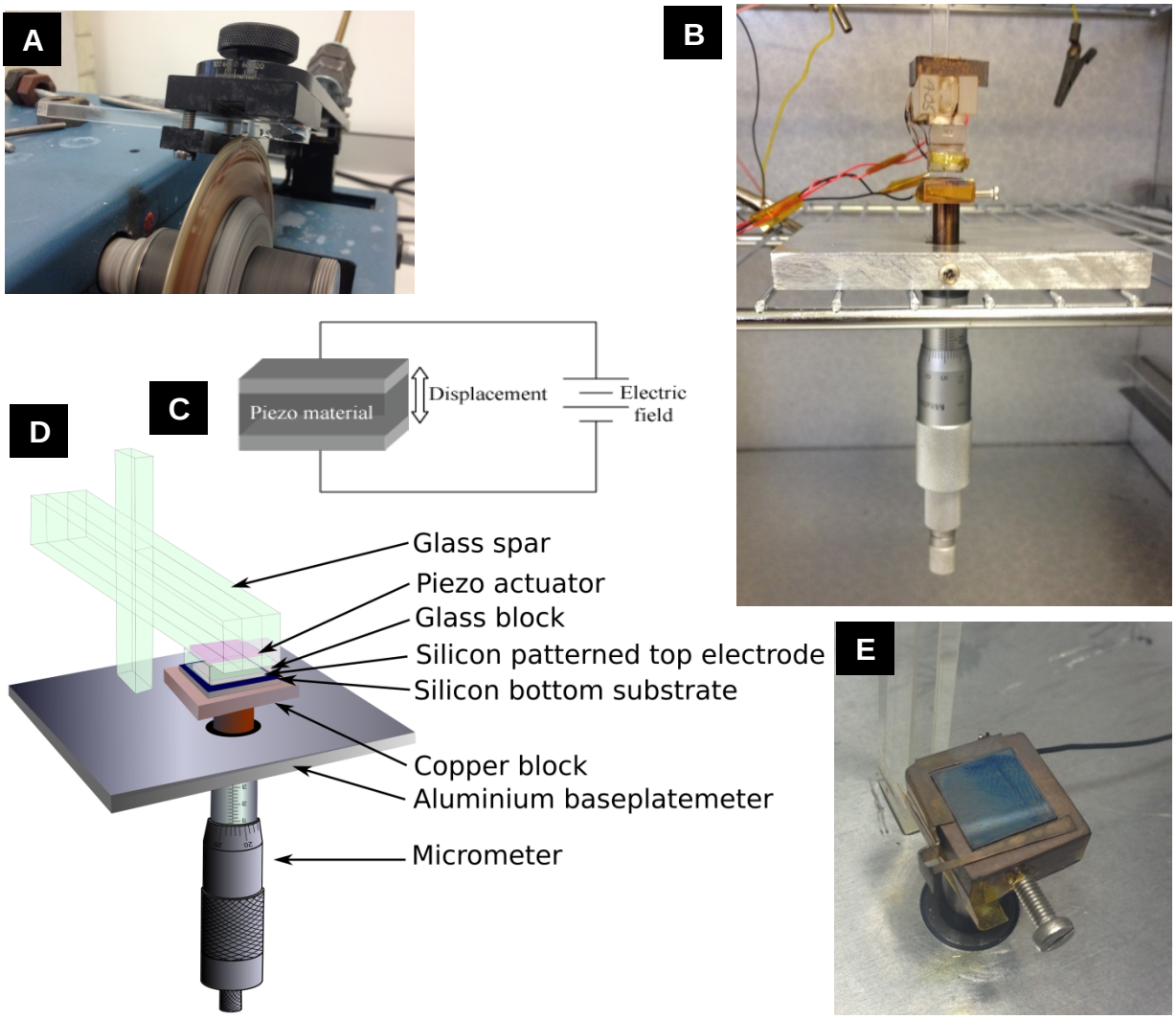

Figure 6.2: (A) Photograph of diamond saw which was used to cut the rectangular glass rods. (B) Photograph of the RED rig sitting inside the oven. (C) schematic of a piezo actuator showing that when you apply a voltage across a piezo material then a deformation happens, expanding the material in one direction and shrinking in another, allowing very fine movement. (D) Schematic diagram of the RED rig showing the micrometer with non-rotating head mounted through an aluminium baseplate. A copper block is attached on to the micrometer with the bottom substrate clamped on top of the copper block. Above the bottom substrate is an air gap and then a patterned top substrate attached to a glass block which has a piezo actuator glued to it which is glued to a glass spar which is clamped to a glass rod. (E) Photograph of the copper block showing the silicon bottom substrate with a polymer nanometre layer on top which is clamped with a beryllium copper clamp which is thinner than the silicon substrate.

The RED micro-lithographic set-up allows well-aligned parallel positioning of the top and bottom electrodes, yielding the integrity and accuracy of the inter-capacitor distance down to the nanometre scale, and thus fabrication of very accurate and highly-reproducible SERS-active substrates at temperatures up to 200°C. The rig was designed to allow for several degrees of freedom of movement and therefore, well-aligned positioning of the top electrode parallel to the bottom thin film. The rig was constructed with a rectangular aluminium base and protruding through the base is a micrometer with a non-rotating head. A copper block was placed on top of the non-rotating head acting as the bottom substrate support. A vertical glass bar pillar was glued, using high temperature epoxy, to the aluminium base-plate, over which a glass arm was clamped using a beryllium copper spring clamp. At the end of the arm, which is above the copper bottom substrate support, a rectangular piezo actuator with two microns of movement was also glued, using high temperature epoxy, with a glass block glued under the actuator. On both the bottom and top substrate supports, beryllium copper spring clamps, thinner than the height of the silicon substrates were glued to hold the silicon on the edges and allow a bias voltage to be applied across the top and bottom substrates. To allow the substrates to be as parallel as possible the two substrates were brought together by adjusting the micrometer until the substrates were pressed together and subsequently, the copper block was then secured in place by a screw clamp onto the micrometer head. Therefore, once the micrometer was backed away from the top, the gap was precisely parallel, which is proven by the fact that the substrates are replicated accurately over a large area which would not happen if the plates were not precisely parallel. Glass was chosen for the supporting pillar parts as it is an insulator and has a low coefficient of thermal

expansion. Once the whole device has been heated up to the required temperature, the gap could be coarsely adjusted by turning the micrometer followed by very fine adjustment by using the piezo actuator. The gap distance was gauged by measuring the current being drawn between the top and bottom substrates and subsequently, adjusted using the piezo actuator. This gave the gap integrity accuracy down to the nanometre scale. We have recently filed a patent describing this novel set-up (Reference: 1701182.6 [169].)

We have established that the highest enhancement factor of the SERS active pillars is achieved when the aspect ratio is 0.8 [170]. We have subsequently, designed and fabricated a dedicated top electrode with protruding pillars of 625nm in diameter. Since, such a top electrode in a RED capacitor-like device generates a laterally varying electric field, the redistributing material is drawn towards the protrusions, where the electrostatic pressure is the highest and the electrohydrodynamic destabilisation process is the fastest, thus faithfully reproducing the imposed structure (Figure 6.3)

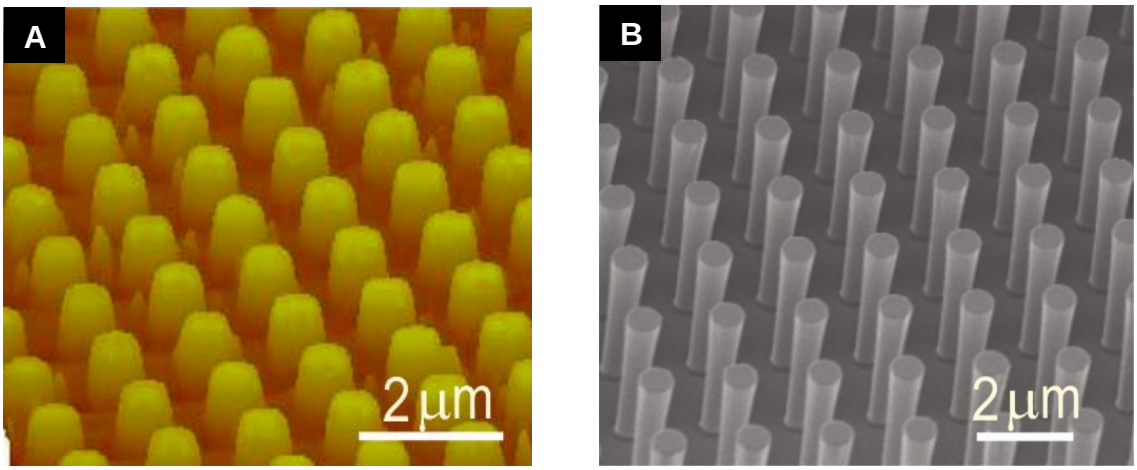

Figure 6.3: (A) AFM 3D image of RED fabricated pillars. (B) SEM image of RED fabricated pillars showing pillars generated under a patterned top substrate with the features tuned by adjusting the inter-electrode spacing, the electric field and the initial film thickness combined with the patterned top substrate.

6.3 Calculation of the Enhancement Factor of RED Fabricated SERS Substrates

To calculate the SERS enhancement, how much extra Raman signal we achieve, from our produced SERS substrates we compared the Raman signal from pure benzenethiol liquid and benzenethiol absorbed on our RED substrates using an In-Via Reneshaw Raman spectrometer. Representative SERS spectra of benzenethiol molecules on RED substrates across several indiscriminate areas on each substrate demonstrate reliable signal and substrate consistency (Figure 6.4 A).

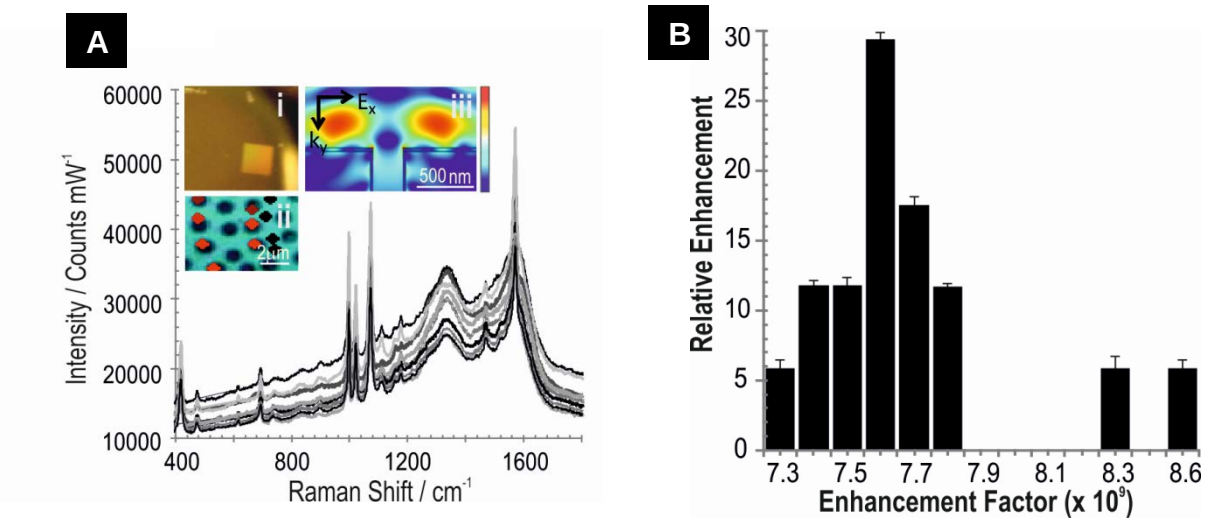

Figure 6.4: (A) Reproducible spectra of benzenethiol on RED-SERS substrates across a number of areas reveal consistent signal and substrate regularity. Insets: (i) A photograph of the gold coated RED-SERS platform with an active area at the bottom right corner. (ii) A representative SERS map overlaid on top of the corresponding optical image reveals that the SERS signal (red) comes exclusively from the RED pillars. No SERS signal is observed from the flat gold or in between the pillars. (iii) FTDT (Finite-difference time-domain) simulation shows the enhanced electromagnetic fields tightly confined on top of periodic pillar surface, maximizing the detection sensitivity. (B) Histogram of the measured electromagnetic enhancement factors of the RED-SERS substrates (n=17) shows a narrow distribution with an average enhancement on the scale of $8x10^9$.

Measuring at three random locations on each substrate, fabricated individually using the dedicated RED rig. The reproducibility coefficient was found to be such that the absolute difference between any three future measurements made on a particular substrate are estimated to be no greater than 4.3% on 95% of occasions. Furthermore, the correlated RED-SERS based enhancement factor (EF) calculation results show that 89% of values are narrowly distributed around the average of $7.73\times10^9 \pm 2.94\times10^9$ (Figure 6.4). We therefore, expect that the difference in the EF as measured between the different substrates to lie between 7.30×10^9 and 7.80×10^9 for 95% of the future measurements. The enhancement factor is normalized by the spot size and since the SERS activity is localized at the surface structure, it stems only from a small fraction of the sample area. The RED-SERS active substrate reproducibly offers a very robust platform for high SERS detection. The SERS enhancement factor was calculated by comparing the intensities of the unenhanced Raman scattering, I_{Raman} peak at 1070 cm^{-1} of pure benzenethiol liquid obtained by focusing the laser into a quartz cell and the corresponding SERS signals, I_{SERS} obtained from the RED-SERS substrates. The detection volume of the solution-phase benzenethiol sample, V_f was calculated using the following relation: V_f = (depth of focus) x (focus area) = $(1.4n\lambda/NA^2) \times \pi(0.4\lambda/2NA)^2$. The surface density of the adsorbed benzenethiol molecules on the structured surface was taken as ρ_s = 3.3 molecules/nm^2 and the enhanced area, *A,* was defined as the diffraction limited spot size = $(\pi(0.4\lambda/2NA)^2)$. The enhancement factor (EF), the amount of photon counts larger than if we had no enhancement, was therefore calculated using the relation: $EF = [I_{SERS}/(\rho_s A)]/[I_{Raman}/(\rho_v V_f)$.

6.4 Fingerprinting Raman Spectra of Biomarkers Using RED Substrates

The RED SERS detection platforms were further used to characterise the fingerprint spectra and to determine the lowest detectable concentrations of three representative biomarkers which are signposted to correlate with TBI including, NAA, S100B and GFAP (Figure 6.5).

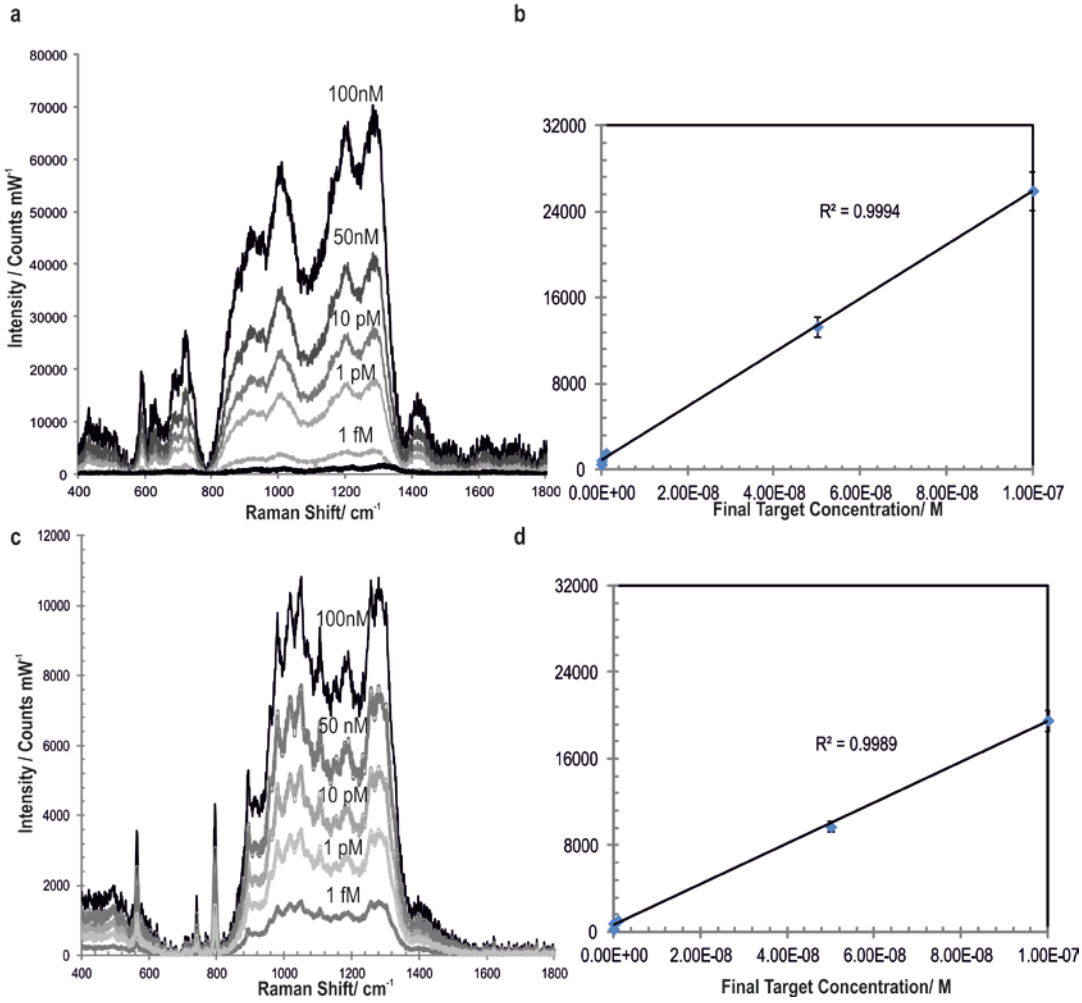

Figure 6.5: Limit of detection and finger print SERS spectra of representative TBI biomarkers. RED-SERS substrates were used as an assay to perform dilutions using the specified concentration range for each biomarker. SERS spectra of **(a)** NAA and **(c)** S100B detected from 100nM to1fM concentrations at identical integration times and laser power of 10mW and the corresponding calibration curves used to calculate the limits of detection, which is three times the standard deviation of the blank divided by the gradient of the linear curve, for **(b)** NAA and **(d)** S100B obtained from the dilution experiments.

The characteristic peaks of each biomarker were monitored and a linear relationship was observed with a very good correlation between biomarker concentrations (100nM to 1fM) and Raman intensity for all the biomarkers, with R^2=0.9994, 0.9989 and 0.9755, for NAA, S100B and GFAP, respectively (Figure 6.6 A). The calculated limits of detection were established to be 1.2x 10^{-13}M (0.021 pg/L) for NAA, 1.9x 10^{-13}M for S100B and 6.7x 10^{-14}M for the GFAP and the limit of quantification (LoQ) for the NAA was found to be 3.8x10^{-13}M. Performing the multivariate analysis on the multiplex biomarker set reveals principal component loadings with clearly separated clusters that recapitulate the fine spectral differences of the molecular fingerprinting spectra, effectively discriminating the three TBI indicative biomarkers (Figure 6.6 inset).

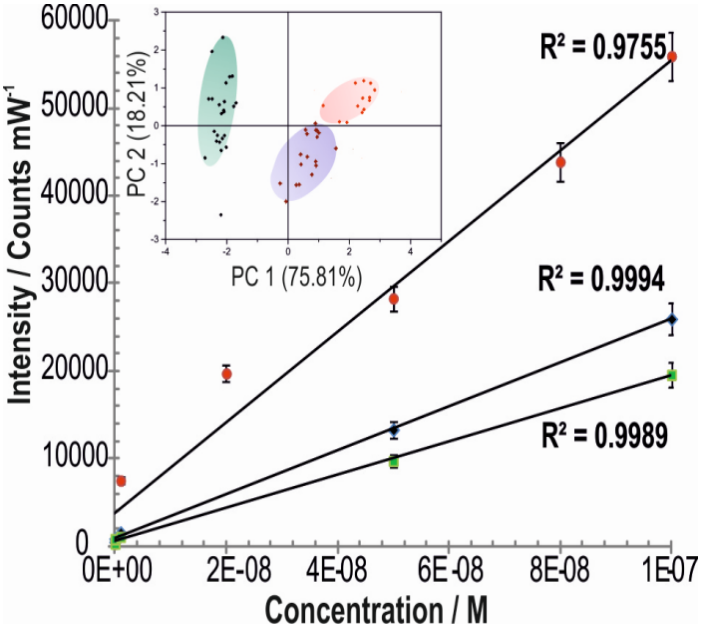

Figure 6.6: The assay was performed for each biomarker using the specified concentration range yielding calibration curves of SERS spectra acquired with an excitation laser of 785nm and a laser power of 50mW with each point representing an average of five measurements of each concentration ±STEDV used to calculate the LoD and LoQ of 1420cm^{-1} for the NAA, 1070cm^{-1} for S100B and 1150cm^{-1} for the GFAP. Inset: PCA score plots of PC1 and PC2 show the relationship between the multiplex spectra of the three single biomarkers. The green cluster is the NAA spectra, the purple cluster represents the S100B and the red is the GFAP.

MEDTech has further been exploited to analyse clinically relevant samples. The biomarkers were measured in clinical blood plasma, collected as part of the Golden-Hour (GH) study (Ethics Ref. 13/WA/0399), providing blood samples from TBI and non-TBI patients. The first blood sample collection was carried out by the ambulance team at the roadside within minutes from the point of injury and further samples were collected at various time points post TBI: 4-12h, 48-72h and 6 months. Overall, a total of 221 measurements were collected using the MEDTech from blood plasma samples of 25 healthy volunteers (HV) as a control group (ReCoS Study, Ethics Ref. 11-0429AP28) and 35 severe TBI (sTBI) subjects including, the sTBI combined with extracranial injury (EC), here defined as the sTBI+EC sub-group and with EC only. The clinical samples study participants were recruited through the [redacted] as part of the RECOS (Ethics Ref. *11-0429AP28*) and the Golden Hour studies (Ethics Ref. *13/WA/0399*). Written informed consents were received from participants or valid proxy (family or a professional not directly involved in the study) prior to inclusion in the study. The study was approved by the National Research Ethics Service (Research Ethics Committee reference *13/WA/0399*, Integrated Research Application System ID *125988*). Both RECOS and Golden Hour studies comply with the guidelines of the Declaration of Helsinki. Initial clinical predictors included age, pupil reactivity, Glasgow Coma Scale (GCS), CT characteristics (Marshall CT classification) and extracranial injury (EC). Patients were categorised into HV, EC, sTBI and sTBI+EC. EC injury patients had radiographically or clinically-confirmed injuries, no history or signs of head trauma, and no current clinically significant infection, individuals with a history of neurological or psychiatric

disorders were excluded. Isolated sTBI patients and sTBI with EC patients were all classified with the severe TBI on the basis of GCS≤8. All patients were gender and age matched to HVs. Patient demographics are shown in Table 6.1. Blood samples from patients in each category were obtained at different time points post injury: *t*=0 (Golden Hour, at the point-o-care, within less than an hour from injury), *t*=4-12h (8h), *t*=48h. Peripheral blood samples were taken at the point-of-care study, *i.e.,* Golden Hour patients by pre-hospital clinicians following initial intravenous access at the scene of injury. Further peripheral blood samples were taken from the same patients during subsequent hospital admission between 4-12h and 48h following the trauma. Once collected, blood samples were left at room temperature for 30 minutes prior to centrifugation at 3000rpm for 10 minutes at 4°C. Serum aliquots were stored at -80°C until analysis. All samples were processed within two hours of venepuncture. Each sample volume was roughly 500µl but only a drop was used to collect the spectra.

6.5 Spike-and-Recovery of the Samples

Following the molecular peak signatures corresponding to specific structural and composition information, we spiked the blood plasma samples of healthy patients with the TBI-indicative biomarkers (Figure 6.7). Samples were assessed by adding 50µl of blood sample and 10µl of spike stock NAA solution calculated to yield the intended 0 and 50 pg/ml spike concentrations. Values reported for spiked samples reflected subtraction of the endogenous (no-spike) value. Recoveries for spiked test samples were calculated by comparison to the measured recovery of spiked diluent control. Diluent for the diluent control and preparation of spike stock solutions was

the same as the standard diluent. All values represent the average of three replicates. 95.5±3.4%recovery of NAA within the spiked samples was observed.

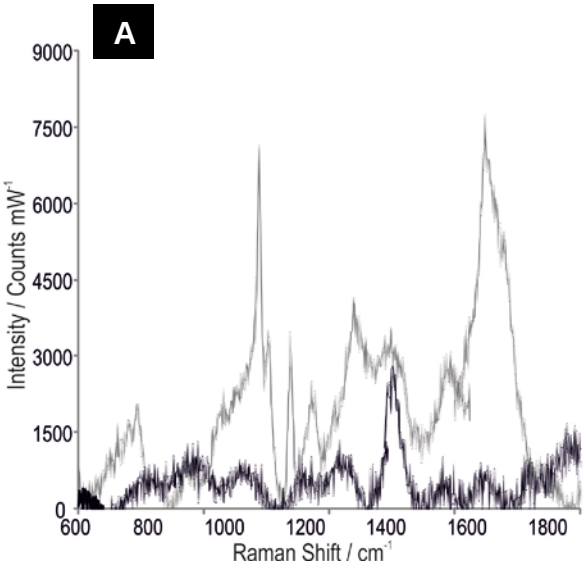

B

Sample	No spike (0 pg.mL)	Spiked (~50 pg/mL)
Control (diluent)	0	53
1	0	51.5
2	0.7	48.9
3	0	51.7
4	0	47.1
5	0	50.9
6	0.7	49.3
7	0.5	52.8
8	2.3	51.5
9	0	49.8
10	0.3	53
Average		50.65
		0.044339623
Mean Recovery %		95.56603774
(+/- S.D.)		(+/-3.4%)

Figure 6.7: Spiked blood with TBI-indicative biomarkers. (A). Spike-and-recovery was used for validating and assessing the MEDTech and to establish whether there is a difference between the diluent used to prepare the standard curve and the biological sample matrix. SERS spectra of the spiked blood (grey) in comparison to the normal, non-spiked blood (black). (B). 10µL of analyte was spiked into the test sample matrix (50µL) and its response was recovered in the assay by comparison to an identical spike in the standard diluent. 95.5±3.4% recovery of NAA within the spiked samples was observed.

Since the recovery observed for the spike was nearly identical to the recovery obtained for the analyte prepared in standard diluent, the clinical blood samples were considered as valid for the assay system. The samples were then analysed with and without the spiked biomarker to test the recovery. Recovery observed for the spike is nearly identical, within the experimental error, to the recovery obtained for the analyte prepared in standard diluents, validating the sample matrices for the detection assay.

Table 6.1. Clinical characteristic and patient demographics of the studied subjects and TBI diagnosis. Patients were recruited from the Golden Hour and ReCoS studies. Patients were categorised into Healthy Volunteer (HV), Extra Cranial (EC), Severe Traumatic Brain Injury (sTBI) and sTBI+EC. EC injury patients had radiographically or clinically-confirmed injuries, no history or signs of head trauma and no current clinically significant infection. Individuals with a history of neurological or psychiatric disorders were excluded. Isolated sTBI patients and sTBI with EC groups included patients with GCS≤8. All patients were gender and age matched to HVs.

Characteristics	Traumatic Brain Injury Patients		EC Patients	Healthy Controls
	sTBI+EC	sTBI		
	$n_{patients}$ =24 $n_{samples}$= 75	$n_{patients}$ =11 $n_{samples}$=37	$n_{patients}$ =8 $n_{samples}$=27	$n_{patients}$ = 25 $n_{samples}$=82
Age				
Mean ±SD (Range)	47±18.8 (21-83)	40.1±16.6 (22-58)	43.6±20.6 (26-79)	42.0±15.2 (18-77)
Gender				
Male/Female	15/9	7/4	8/0	17/8
Race/Ethnicity				
White/Asian	19/5	10/1	5/3	18/7
Mechanism of Injury				
Assault/Fall	4/10	0/2	0/3	-
Penetrating/Road Traffic Accident	1/9	0/9	2/3	-
Death				
	4	1	0	-
CT Findings [a]				
Visual pathology: (-) No/(+) Yes	7/17	2/9	-	-
Clinical Diagnosis				
Marshall Grade				
Mean ±SD	3.5 ±2.1	3.1 ±1.9	-	-
Glasgow Coma Scale (GCS)				
Mean ±SD (Range)	3.8 ±1.4 (3-8)	4.9 ±2 (3-8)	-	-
MEDTech				
Median, *pg*/mL ±IQR	6.73 ±4.05	6.03 ±0.52	0.85 ±0.27	1.22 ±0.45

6.6 Statistical and Computational Analyses

SERS spectra were analysed for biomarker levels using the software MATLAB® (Natick, MA). All patient data and biomarker spectra were interpolated onto equal-spaced grids using the cubic approximating spline routine ‘csaps’ (with smoothing

parameter set to zero, i.e. no smoothing). The projection of a spectrum $(x_j)_{j=1}^{n}$ against the kth biomarker $(b_j^k)_{j=1}^{n}$ was computed *via* dot products, *i.e.*, $P^k(x_j) = \frac{\sum_{j=1}^{n} x_j b_j^k}{\sum_{j=1}^{n}(b_j^k)^2}$. Projections for control and patient spectra were compared for each biomarker in turn using the Wilcoxon rank sum/Mann-Whitney U test. We used the full spectrum, 3189 data points, of the patients' blood against the individual spectra from each biomarker to calculate the Wilcoxon rank sum/Mann-Whitney U test. Correlation analysis between each set of projections was carried out with the MATLAB® routine 'corrcoef'. Logistic regression was performed with the MATLAB® routine 'fitglm' sequentially on models consisting of each possible combination of 1, 2 and all 3 projections P^k as predictors of HV or GH group.

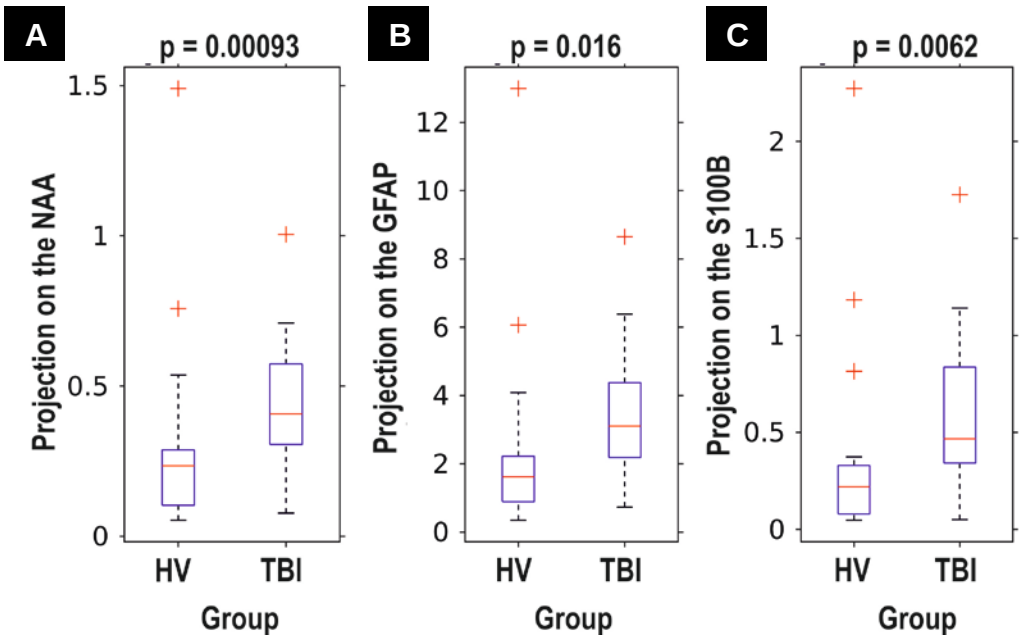

Figure 6.8: Box-and-whisker plots. Projections of spectra onto TBI-indicative biomarkers. *p*-values calculated *via* Wilcoxon Rank Sum/Mann-Whitney U test.

Principal components analysis was performed with OriginPro 9.0 and MATLAB R2015b (The MathWorks, Inc.) with advanced chemometric software, PLS Toolbox 8.2 (Eigenvector Inc.) with R statistical software equipped with root mean square package. The Wilcoxon rank sum/Mann-Whitney U test of TBI biomarkers for healthy control group, HV and TBI patients yielded significantly different spectra between the sTBI and HV groups when analysed for each biomarker (Figure 6.8). With the difference between the GH and HV groups being the most significant for the NAA biomarker, (Figure 6.8) specifically differentiating between TBI and non-TBI patients, we have further predominantly focussed on studying and detecting the NAA as a primary TBI biomarker.

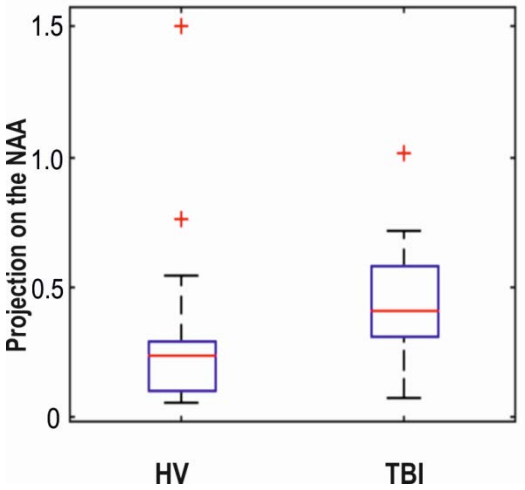

Figure 6.9: Wilcoxon rank sum/Mann-Whitney U test projections on the NAA biomarker reveal a significant difference between the sTBI and HV groups ($p<0.001$).

NAA is one of the most abundant molecules present in the central nervous system which, due to its exclusive localization in neurons, reflecting the functional status of neurons and axons in the brain. It is considered as a marker for neuronal health and viability, highly specific to the central nervous system and not released by other organs and thus, is a very sensitive measure of neuronal compromise. This has been

observed in the brain of patients with TBI, among others by *in-vivo* H^1-MRI or by post-mortem histopathological evidence, [171] signposting NAA as a simple biomarker for detecting early TBI onset, monitoring its progression and identifying possible therapies. However, while NAA was previously detected from serum in pathological conditions of *Canavan*, its detection was only possible due to the very high concentration accumulated in the brain and followed by a substantial excretion into the blood [172]. Clinical evidence suggests that high NAA levels found in CSF provide a very sensitive predictor of neuronal damage and mortality.

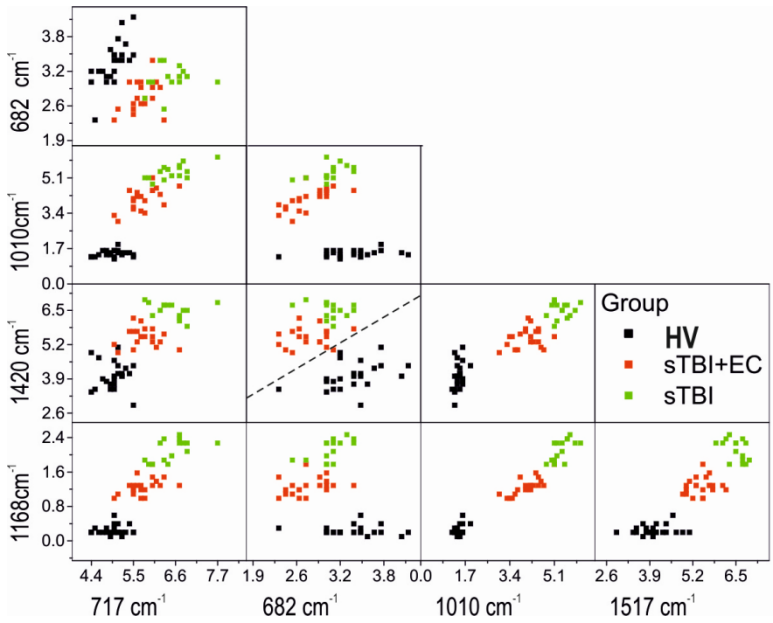

Figure 6.10: Classification matrices of the feature selection of subset of relevant features, used to establish the important peaks and their correlations reveals decision boundaries of multi-layer perception with distribution of the selected peaks with clear separation at each subset between the sTBI and the HV patients

To acquire a classification of the SERS data, a feature selection of an optimal subset of relevant features was used to establish the important peaks and their correlations

and thus, it contains the least number of features, discarding the unimportant ones [173]. Firstly, by calculating the highest *a posteriori* probability (maximum *a posterior* method), according to the classification rule of: "select the class, w_i, in the maximum *a posterior* classifier that maximised the *posterior* probability, $P(\mathbf{x} \mid w_i)$, and if $P(\mathbf{x} \mid w_i) \geq P(\mathbf{x} \mid w_{i+1})$", then primary significant peaks yielding the most discriminality from the pre-processed spectrum were chosen as the feature candidates for classification with the most discriminating peak selected as a reference feature at 1420cm^{-1}. Consequently, the ratio of intensity of all primary peaks yields the extended feature set. This was followed by computing the correlation coefficients between the reference peak and each chosen peak and finally, the highly correlated features *i.e.,*

Band Shift (cm^{-1})	Correlation Coefficient	Classification Rate (%)
682	0.0918	61.3
717	0.1614	75.5
904	0.4185	61.9
930	0.1227	63.3
1010	0.2513	67.7
1168	0.2733	70.9
1207	0.8975	63.7
1292	0.5865	63.4
1420	1.0000	79.8
1517	0.0791	73.5
1623	0.3701	61.1
1735	0.3124	67.7

Table 6.2: Initially, the primary significant peaks from the pre-processed spectrum were chosen as the feature candidates for classification with the most discriminating peak selected as a reference feature at 1420cm^{-1}. Subsequently, the correlation coefficients have been computed between the reference peak and each chosen peak and finally, the highly correlated features (with correlation coefficient above 0.35) have been discarded.

with correlation coefficients >0.35, had been discarded. Since both the ratio of peaks intensities as well as the intensity itself of various peaks can be used for SERS classification, the feature set included the optimal possible combinations of primary peaks and ratios. Table 6.2 summarises the classification rates of the primary peaks and the correlation coefficients. Ranking the classification performance and examining the features of the top ten percent of the cases, the most frequently appearing features included, intensity and the ratio of the peaks at 1420 cm^{-1} and 1517 cm^{-1} and 682, 717, 930, 1010, 1168 cm^{-1}. The multi-layer perception classifier with the selected features enabled a consideration of all possible variables within the SERS spectra set and of their significance for the discrimination between classes. The models' unit operation equation is given by the activation function, $f()$ and the input to the unit, net_k: $\mathbf{o}_k = f(net_k)$ using the back-propagation algorithm, these were trained to output (+1) for HVs group and (-1) for sTBI group. These variables were taken into a consideration due the reduction of the original SERS spectra to subsets of wave-numbers, simplifying the spectral dataset for the possible identification of meaningful information. The Raman bands that yielded the best results for internal cross validation were identified from the most informative spectral regions. These regions and bands represent spectroscopic markers for the datasets in the study. They may relate to excretion of NAA into the blood circulation, where the levels are considerably diluted, following increased metabolite from damaged neurons and in physiological conditions low serum NAA levels might be related to its rapid filtration in the kidneys[174]. Subsequently, a feature selection method was employed to establish an optimal (in collaboration with D. Smith and M.J. Rowney, UoB), small subset of peaks allowing the discard of the least important features [173, 175]. Initially, all the

significant peaks of the NAA spectra were selected for classification and the calculated correlation coefficients between the reference peak (1420cm^{-1}) and every chosen feature allowed to reduce the number of feature candidates, selecting the most frequently appearing peaks (Table 6.2). Figure 6.9 shows the matrices of multilayer perceptions with distribution of the highest performed selected features of sTBI, sTBI+EC and HV with each axis corresponding to the intensity or ratio of maximum value at each selected peak, providing clear decision boundaries for the patients with and without TBI.

6.7 NAA SERS Finger-print Barcode

Raman Band cm^{-1}	Peak Assigenment
682 m	γ(C=O) τ(O-H) in N-acetyl bending mode of C=O-O
717 m	σ (CαC), def(O-H)
930 s	υ(C-C) and N-C symmetric stretching
1010 w	Out of plane ρ(CH_3), τ (CH_2) and γ(C=O) amides
1168 m	γ(C=O) and δ(C-OH)
1420 m	σ (COO-), acetylamide in the CH_3-NH-C=O of the N-acetyl asymmetric *def*(C_tH_3) and δs(CH_3)
1517 s	δ(N-H) in (NH-C=O-CH_3) group

Table 6.3: The assignments of major SERS peaks of NAA on RED substrates. σ, stretching vibration, δ, bending vibration, δ_s-symmetric bending vibration, ρ-rocking, in-plane bending, γ-wagging, ν-breathing, τ-twisting; Raman intensity: *s*-strong, *m*-medium, *w*-weak.

SERS spectra of the blood plasma taken from patients diagnosed with sTBI and sTBI+EC at *t*=0 in comparison to the healthy control group reveal distinct spectral

features including, the increase in the intensity ratio of peaks at 717cm^{-1} and 1010cm^{-1} and the appearance of new peaks or increase in their intensity at 682, 930, 1168,1292, 1420, 1517 and 1623cm^{-1} (Table 6.3). Specific differences of certain selected features originate from biochemical variations in blood plasma post TBI are reflected in the SERS spectra indicating the molecular composition changes (Figure 6.11).

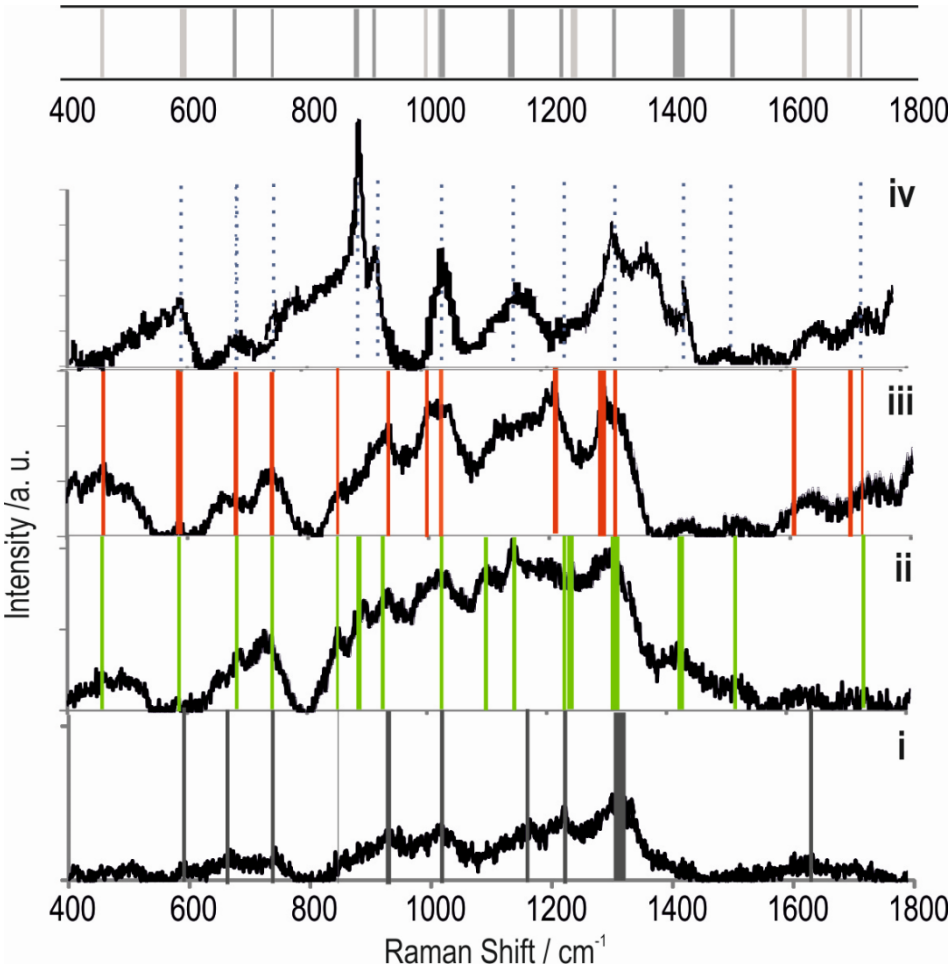

Figure 6.11: Average SERS spectrum of (i) HVs excited at 785nm are compared to the SERS spectrum of (ii) sTBI only and (iii) sTBI+EC and to the finger print spectrum of the (iv) NAA with the representative significant peaks highlighted with vertical (i) grey, (ii) green, (iii) red and (iv) doted lines, accordingly, highlighting the correspondence or the absence of the NAA peaks with some vibrational frequencies of the bands being unchanged in SERS spectra whereas several are not evident in the HVs spectrum. At the top an averaged barcode derived from SERS spectra shown for sTBI diagnostics.

The intensity of the peak at 682cm^{-1} is attributed to the wagging of C=O and twisting of –OH bonds in *N*-acetyl groups whereas, the peak at 717cm^{-1} originates from the stretching of C=C bonds as well as the deformation of the O-H groups. The peaks at and between 1010cm^{-1}, 1168cm^{-1} are assigned to the out of plane rocking mode of the CH_3, twisting of the CH_2 and the wagging on the C=O amides and the N-H vibrations in the NH-C=O-CH_3 group at 1517cm^{-1} are characteristic of N-acetyl groups, which are significantly elevated in the blood plasma samples derived from sTBI patients and absent or at considerably lower concentration in the healthy control samples. Additionally, the intensity of the peak at 1420cm^{-1} originates from the acetylamide in the CH_3-NH-C=O of the *N*-acetyl asymmetric *vib* CH_3 deformations. The selected feature bands closely reflect the NAA molecular structure and its variations associated with the biochemical changes in the brain at the earliest stages of TBI (Figure 6.11).

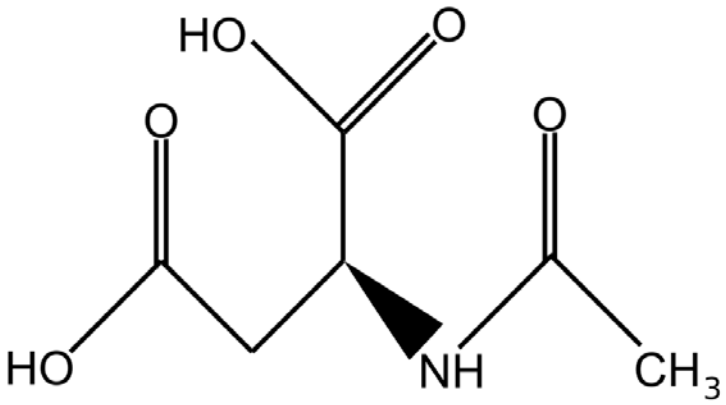

Figure 6.12: The chemical structure of N-acetylaspartic acid (NAA) [142]

At the t_{TBI}=0, peaks originating from NAA become more pronounced in the SERS spectra, indicating that in the earliest stages post TBI, the concentration of NAA

increases in blood plasma providing a pre-diagnostic value to the histopathological outcomes. SERS vibrational signatures of blood plasma in Figure 6.11 i-iii from the healthy cohort, sTBI clinical samples and sTBI with EC show prominent variability between sTBI and the non-TBI patients. The characteristic peaks from sTBI and sTBI+EC spectra are then compared with the fingerprint SERS spectra of the NAA (Figure 6.11, iv) with selected features of five peak ratios and three peak intensities (highlighted as dotted lines) form the multilayer perception classification yielding the SERS barcode for TBI detection *via* a specific TBI-indicative biomarker.

6.8 SERS Monitoring of the Temporal Evolution of TBI

Next, we carried out NAA profiling to monitor clinical progression of TBI for more targeted management of secondary brain injury events, which could be linked to episodes of resulting deterioration such as raised intracranial pressure [176]. With our test being cheap, quick and easy it should have a major impact on monitoring of TBI over time to catch when intracranial pressure is raising, which currently is very expensive and time consuming to diagnose as requires CT scans, which may still not show the increase in pressure build up. Time-dependent SERS spectra of NAA show dynamic fluctuations of neurochemical marker levels over the course of time (Figure 6.13) as the NAA is continuously effluxed from neurons into the blood circulation and thus, builds up temporal profiles of extracellular activity during the various phases of TBI. The I_{1420}/I_{1517} ratio may be used not only for the differentiation of the sTBI but also to monitor the progress post injury as the ratio of the peaks decreases with time depending on the pathological status. Therefore, temporal evolution of blood plasma

using MEDTech enables quick, direct, early, more sensitive and easy detection of neuromarkers than CT or H^1-MRI for instance. It is also very easy to do successive tests to assess the state of the brain which is a very costly and time consuming process using CT or H^1-MRI. We observed a temporal correlation to the mean levels of the NAA which were more than

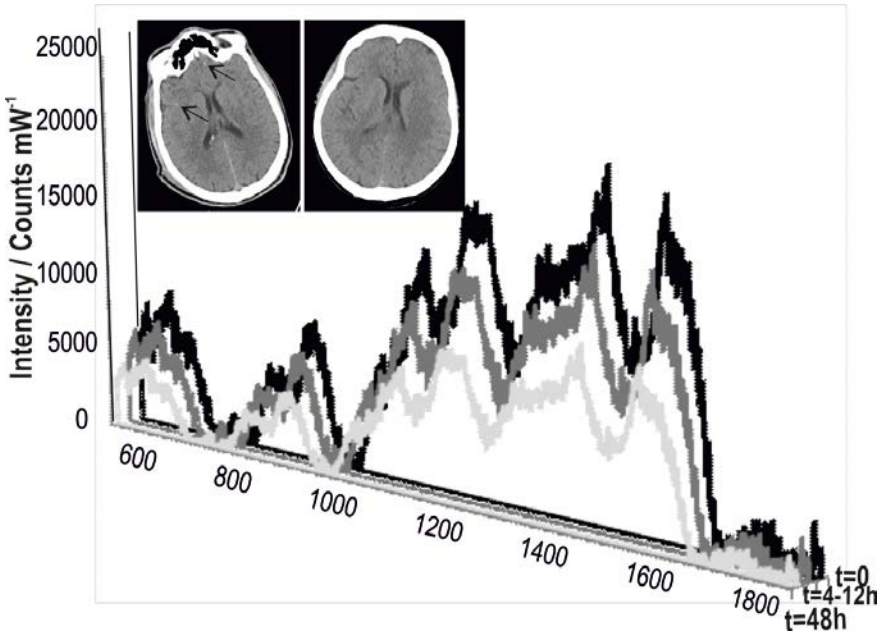

Figure 6.13: SERS spectra show decreasing levels of the biomarker NAA as a function of time from *t*=0 through *t*=8h (4-12h) and to *t*=48h following sTBI. Inset: CT scans of the positive sTBI (left) with typical lesions indicated by arrows and the negative sTBI (right) for clinical diagnoses

five times higher in sTBI patients at *t*=0 than in the control group which gradually decreased over the course of 48 hours (Figure 6.14). NAA levels were significantly elevated in patients with sTBI after the injury (median: 6.03pg/mL, IQR: 0.52pg/mL, range: 4.51-14.77pg/mL, $p<0.0010$) compared with the control cohort (median:

1.22pg/mL, IQR: 0.45pg/mL, range: 0.71-2.74pg/mL) and the EC group (median: 0.85pg/mL, IQR: 0.27pg/mL, range: 0.12-1.67pg/mL) (Table 6.1).

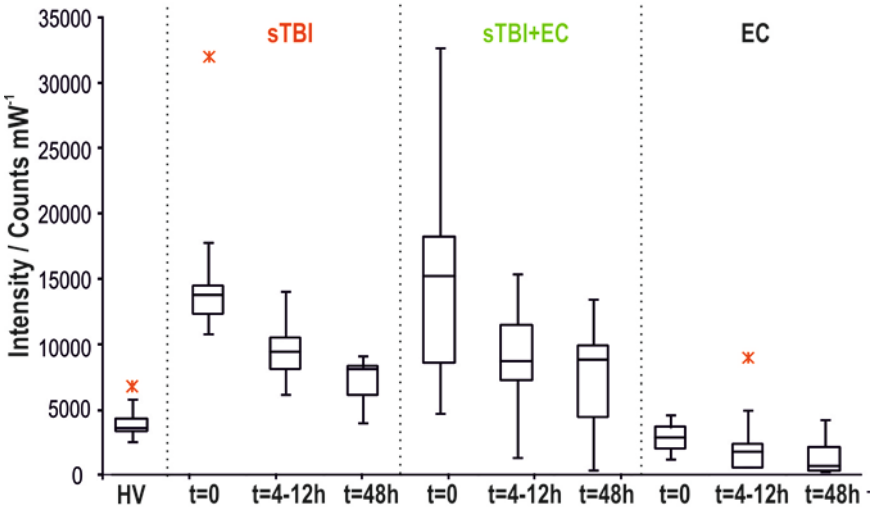

Figure 6.14: Box and whisker plots represent the median in *p*g/mL and interquartile ranges, comparing the NAA levels within plasma tested within *t*=0 to *t*=48h in patients with severe traumatic injury versus healthy volunteer (HV) and extracranial (EC) controls. In all three groups the NAA levels have increased at *t*=0 and subsequently, decreased incrementally with time.

6.9 Receiver Operating Characteristic Curves for Profiling Data and Analysing the Ability of NAA to Differentiate sTBI Patients

For the clustering analyses, R Project for Statistical Computing package was used and the groups (sTBI, sTBI+EC, EC only and HVs) were clustered using Pearson correlation coefficient, P(1 – P) as the distance metric. ROC curves were generated from patient profiling data for different cut-off points [177] . Each point in the ROC curve represents a sensitivity/specificity pair corresponding to a particular decision

threshold and the diagnostic values of sensitivity, specificity, and accuracy were calculated using standard equations. A test with perfect discrimination (no overlap in the two distributions) had a ROC curve that passed through the upper left corner (100% sensitivity, 100% specificity). Therefore the closer the ROC curve is to the upper left corner, the higher was the overall accuracy of the test. Box plots were generated using the Vertex42 LLC software where each of the series is an X-Y chart used to represent the quartiles and allows the data to include negative values.

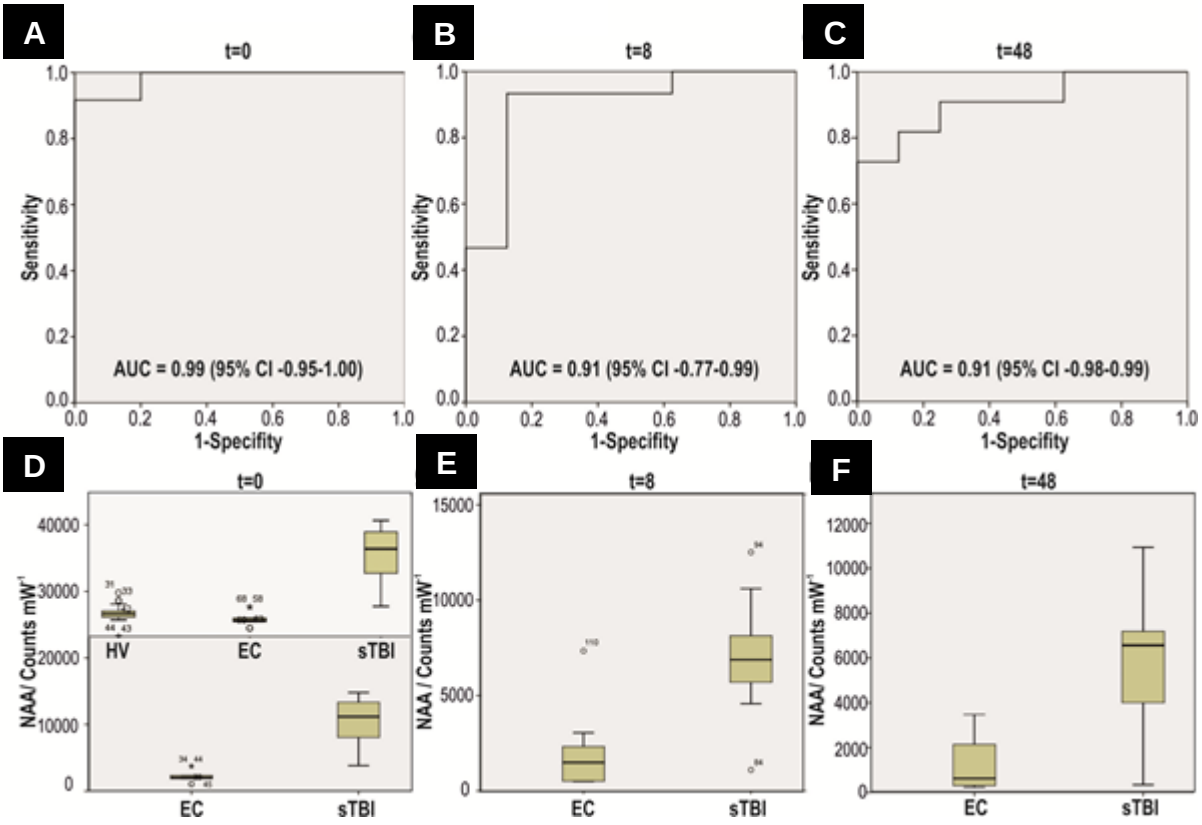

Figure 6.15: ROC plots representing the sensitivity *versus* 1-specifity derived from three time points following the sTBI applied to determine the success of the MEDTech for classifying the sTBI, EC only and HV groups at **(c)** *t*=0 **(d)** *t*=8h and **(e)** *t*=48h . The AUC indicates that the change in the NAA levels following the sTBI is a valuable marker to discriminate sTBI from the EC with the NAA showing an excellent performance with AUC=0.99 (p<0.0001) at *t*=0 and AUC=0.91 at *t*=48h post sTBI. (f-h). Box plots of the plasma NAA levels in EC group and in patients with sTBI, representing the 25th and 75th quarties, range and whiskers and the median (p<0.001) with normal based, two-sided 95% confidence interval of less than ±5% for each class.

The median is represented with an "*x*" marker and horizontal markers are used for Q1 and Q3 without requiring of shifting the data. The mean levels of the TBI patients' group in comparison to healthy volunteers control group were performed using two-sided normal-based 95% CIs t-test. Classification sensitivity, accuracy and specificity were determined on the basis of sTBI detection results: Sensitivity=(TP)/(TP+FN), Specifity=(TN)/(TN+FP) and the Accuracy= (TP+TN)/(TP+TN+FN+FP) with TP being 'true positive', TN 'true negative', FP and FN 'false positive' and 'false negative', accordingly. We used the receiver operating characteristic (ROC) curves to assess the patients profiling data and analyse the ability of NAA to differentiate sTBI patients at various time points after the injury by calculating the area under the curve (AUC) at each time point post TBI plotting the true positive *versus* the false negative rates (Figure 6.15 A-B). From the ROC curves we determined the intrinsic classification accuracy of 98.7% for the NAA at *t*=0 (Figure 6.16), 90.9% at *t*=8h (Figure 6.15 B) and 91.0% at *t*=48h (Figure 6.15 C), clearly discriminating between sTBI and HV groups and sTBI *versus* EC patients, which is crucial for classifying traumatic head injuries versus injuries occurring elsewhere in the body. Molecular fingerprinting based on RED SERS-active technology is highly sensitive and specific and can rapidly detect the indicative biomarkers at the earliest point of interest (Table 6.4) enabling an important diagnostic platform from both therapeutic and prognostic viewpoints. Stratified plasma NAA levels based on the median values were higher in sTBI cases than in EC group (Mann-Whitney test) at all three time points with a particularly significant difference at *t*=0 where NAA concentrations are seven times higher in sTBI *versus* the extracranial injury cases with no overlap in the outliers of

the 95% confidence interval of the non-parametric quarter range in comparison to a low number of overlaps with the outliers in the HV group (Figure 6.15 D-F).

Biomarker	AUC	Cohort	Condition	N	Controls	Reference	Timing	Comment
S100B	0.87	TBI all severity	TBI *vs* non-TBI	50	50	Borg K et al., 2012	Within 6h	Non-specific
S100B	0.68	mTBI	Ice hockey *vs* pre-season	28	28	Shahim P, 2014	Within 1h	Poor performance
Neuron-specific enolase	0.82	TBI all severity	TBI *vs* non-TBI	50	50	Borg K et al., 2012	Within 6h	Non-specific
Neuron-specific enolase	0.54	mTBI	Ice hockey *vs* pre-season	28	28	Shahim P, 2014	Within 1h	Poor performance
Neuron-specific enolase	0.64	mTBI	Clinically important injury	25	82	Wolf H, 2013	Day 1	Non-specific
Myelin-basic protein	0.66	TBI all severity	TBI *vs* non-TBI	50	50	Borg K et al., 2012	Within 6h	Poor performance
Cleaved tau	0.74	mTBI	Injury *vs* preseason	28	25	Siman R, 2015	At 36h	Late
Total Tau	0.80	mTBI	Ice hockey *vs* pre-season	28	28	Shahim P, 2014	Within 1h	Promising
Glial fibrillary acidic protein	0.84	mild-moderate TBI	Positive CT	209	188	Papa L et al, 2014	At 4h	Limited sensitivity
Ubiquitin C-terminal hydrolase	0.87	mTBI	GCS 15 *vs* controls	86	199	Papa L, 2012	Within 1h	Promising
Ubiquitin C-terminal hydrolase	0.73	TBI	Positive CT	N/A	199	Papa L, 2012	Within 1h	Promising
Amyloid-beta (1-42)	N/A	sTBI	TBI *vs* controls	12	20	Mondello S, 2014	D1	Poor sensitivity
αII-spectrin break-down products	0.76	mTBI	Injury *vs* preseason	25	25	Siman R, 2015	At 36h	Late

Table 6.4: Representative area under the curve (AUC) values of TBI indicative biomarkers for severe and mild traumatic brain injury, sTBI and mTBI, accordingly.

MEDTech enables detection at *p*M concentrations indicating a sharp increase in the NAA levels in blood plasma post TBI, followed by a gradual decrease of the metabolic marker levels, without reaching the corresponding control group values

after 48 hours. Our data thus, indicates that following acute neuro-damage, in particular, at the earliest trauma stages, sTBI events are characterized by a leakage of NAA into the blood stream, highlighting the possibility of detection and diagnosis at the PoC. The time course of NAA in TBI observed in our experiments, with five times higher biomarker levels compared to the healthy controls and patients with EC trauma at the early stages post injury, indicates a direct correlation to the neuronal damage, implying NAA efflux to the blood stream.

6.10 RED Integration within a Microfluidic Chip for Realtime Human Blood Separation

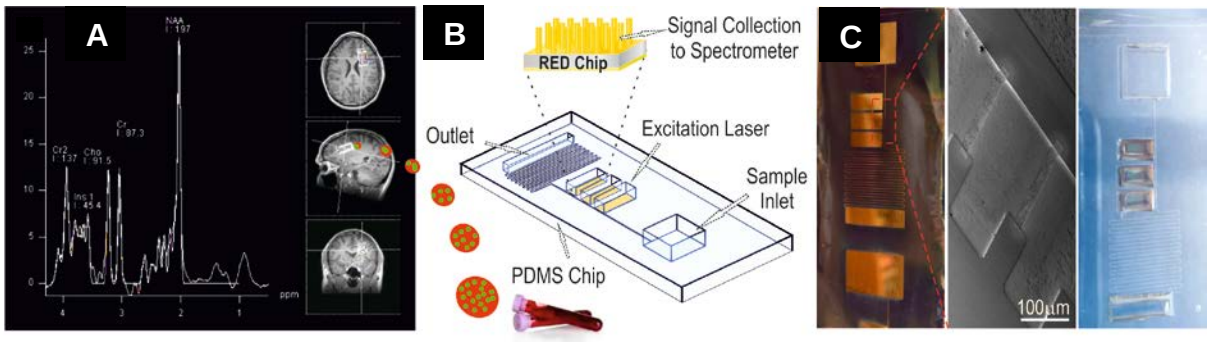

Figure 6.16: Rapid, PoC MEDTech based TBI bodiagnostics **.** (A) Neurological imaging using H^1-MRI provides stratification of TBI in a hospital environment. In the early stages post TBI, the brain leaks neuro biomarkers at *miniscule* concentrations into the CSF and blood stream. A small volume of blood is collected *via* a finger prick and placed into the (B) optofluidic lab-on-a-chip for a rapid plasma separation schematically shown. (C) an optical image of the copper master used for fabrication of the PDMS along with a zoomed-in SEM image of the micro-channel filters and reservoirs of the fabricated PDMS microfluidic chip integrated with RED substrates , photographed on the right hand-side, functional with an input of 1-2 drops (10-20µL) of whole human blood (extracted by a standard pin-prick tool) to output blood plasma with an operation time on the scale of 1-2 minutes and is based on the capillary motion and comb filter separation approach. The microfluidics platform is ensuring a seamless integration of RED-SERS substrate in the fluid flow creating a thin layer of blood plasma over the SERS active substrates.

We established a quantitative assay which provides discriminative sensitivity to detect target biomarkers with trace level analyte concentrations. Consistent RED sub-microstructures are highly uniform, easily synthesised in a single step process and exhibit high SERS signal enhancement, making the MEDTech well suited for label-free real-time bio-diagnostic applications as well as for fundamental studies of biochemical mechanisms involving the detected analytes. Optofluidic RED-based SERS substrates were further integrated within a microfluidic chip combined with miniaturized Raman optics, (Figure 6.16) providing distinct advantages in delivering affordable, portable, non-invasive and highly-sensitive neurotrauma-indicative sensing platforms. Early PoC detection of TBI in plasma could be used for a reliable rapid triage of neurological damage for continued monitoring and subsequent treatment steps.

The initial designs of the blood separating microfluidic chip with integrated SERS substrates failed due to common faults in the design (Figure 6.17).

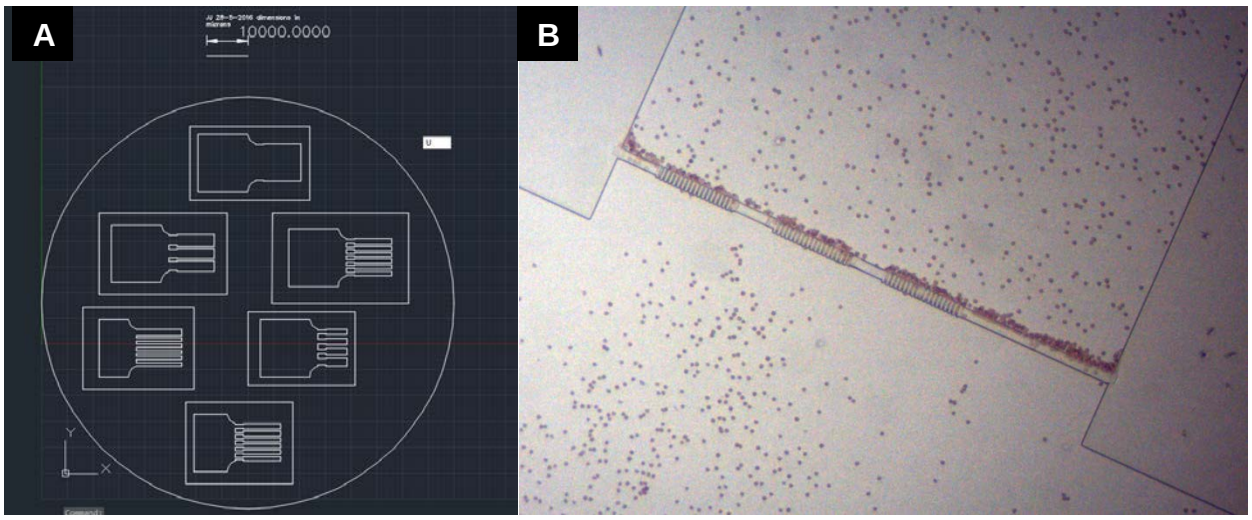

Figure 6.17: A) Initial cad designs of the microfluidic chip all with the same major flaw with the flow of the blood directly at the comb filter with the red blood cells then blocking up the filter. B) Micrograph showing the filter blocked by the red blood cells and also showing the filter had not sealed properly allowing some red blood cells through.

The main fault was having the flow of the blood towards the filter combs and thus the red blood cells block the filter, not allowing enough plasma into the collection area. Also the filter comb design was to narrow which meant that it did not seal properly, allowing some red blood cells through. The redesign of the microfluidic chip flows the blood past, perpendicular to, the filter thus reducing blocking of the filter comb by the red blood cells (Figure 6.18). The redesign also has a better collection area for the SERS substrates.

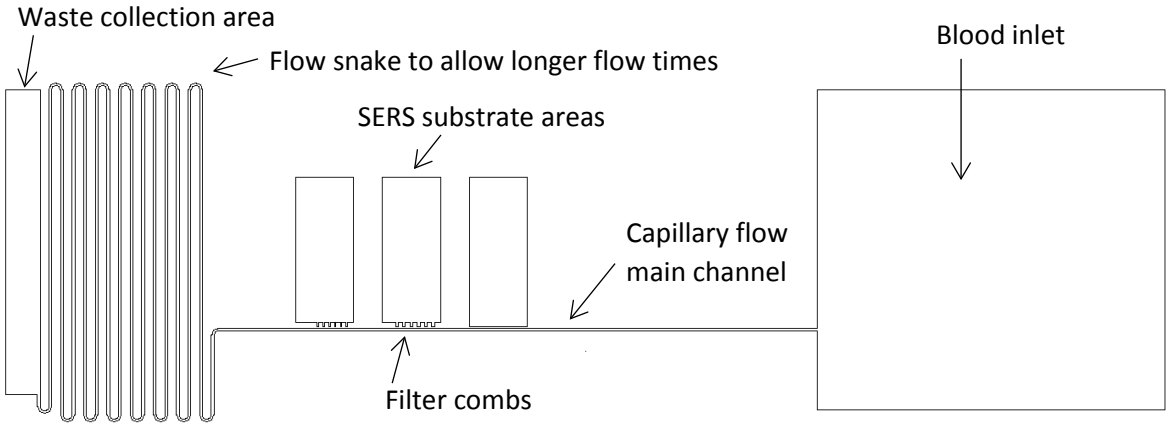

Figure 6.18 Cad drawing of the final microfluidic chip showing blood inlet, capillary flow main channel, filter combs, SERS substrate area, flow snake to allow longer times of flow and waste collection area.

Biofluid samples are easily introduced into the microfluidic channels, via the inlet box. Once the pin prick of blood has been dropped into the inlet box of the microfluidic chip then the whole human blood flows along the main capillary channel (100.0±2µm) by capillary forces only. Once the whole blood reaches the filter comb structures only the plasma can fit through the filter combs which have a size of 2.0±0.3µm into the collection region efficiently filtering out the red blood cells with the continuous flow down the main microchannel reducing the blocking of the filter combs.

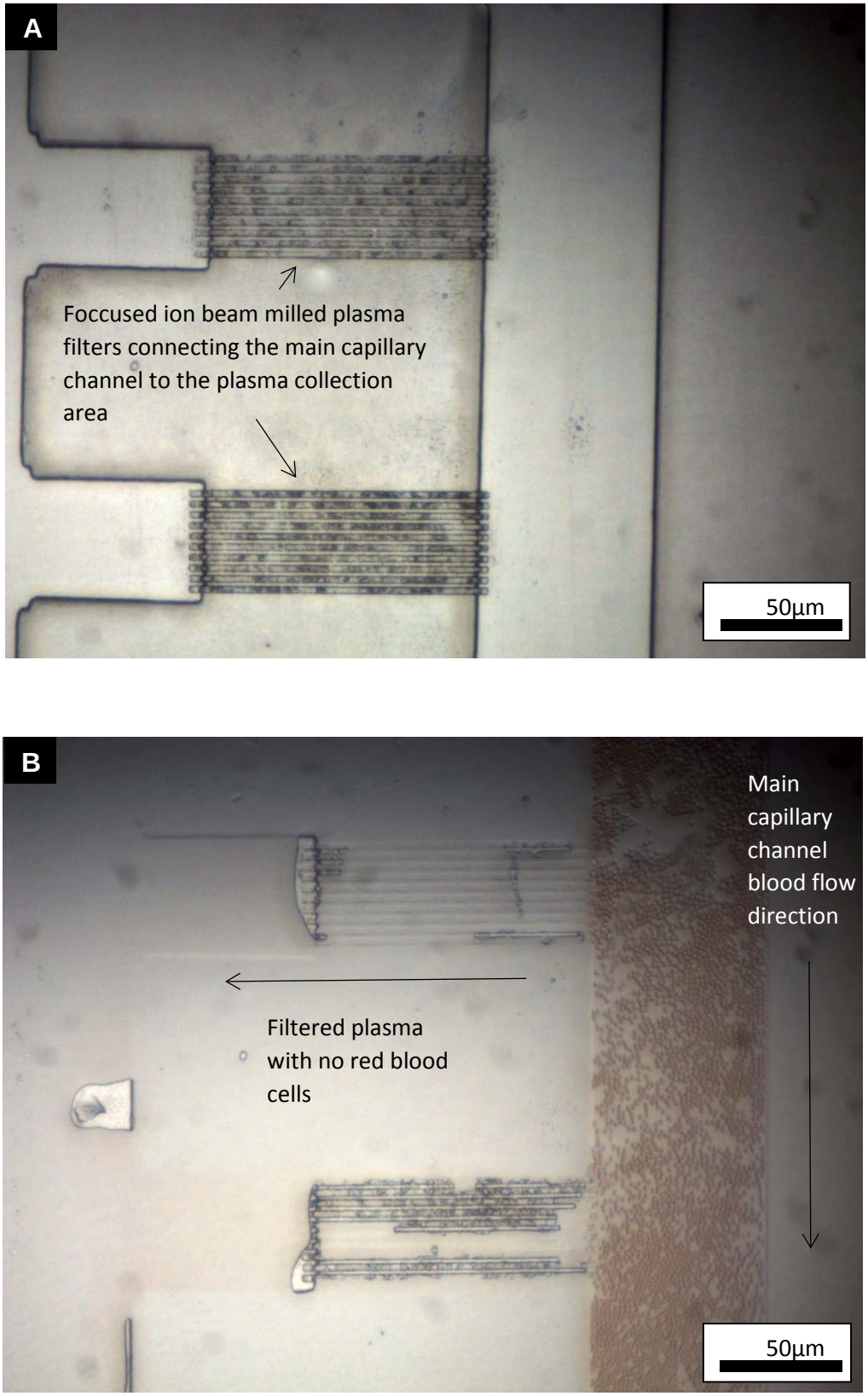

Figure 6.19: (A) Micrograph of filter combs within microfluidic chip prior to blood insertion, the main capillary channel is visible on the right hand side with 2 sets of filter combs branching off to the side and connected to the RED-SERS substrate collection area. (B) Micrograph of microfluidic chip once a drop of blood has been introduced into the inlet box, the plasma and red blood cells

are clearly visible in the main capillary channel with plasma clearly visible in the filter combs and in the RED-SERS collection boxes with 100% filtering out of the red blood cells. It can be seen in the bottom filter comb that some of the filters were blocked and never allowed plasma through but with several filter combs per collection area enough plasma is allowed through to the collection boxes.

MEDTech comprises a spectral detection assay with a disposable integrated optofluidic SERS unit, (Figure 6.20 C inset) a portable Raman system for PoC sample analyses, consisting of a 785nm laser, lenses, gold and diachroic mirrors and an echelle spectrometer (Figure 6.20 A) and a novel single use microfluidic chip to rapidly separate plasma from the whole human blood through capillary action and directly filter the plasma to the SERS detection region (Figure 6.19 A and B). The microfluidic chip enables that a drop of blood is sufficient as an input sample volume, enabling the use of the finger prick procedure for blood sampling in our system *versus* the alternative need of traditional vein-puncture for blood drawing. Therefore, the RED-SERS unit integrated into the optofluidic lab-on-a-chip yields a single platform for the whole process including processing of the blood sample and biomolecule detection. Tailor-made filter comb sizes can be made to allow the separating of different constituents of blood into each collection reservoir for SERS analysis. The high sensitivity of the detection technique combined with the small volumes of the microfluidic chip enables that only a drop of blood is sufficient as an input sample volume, enabling the use of the finger prick procedure for blood sampling in our system *versus* the alternative need of traditional vein-puncture for blood drawing. The Microfluidic chip is inserted into the Raman collection unit where the Raman spectra are acquired while the laser spot is focused on the RED pillar(s). Only *minute* volumes are required to obtain the spectrum for the identification of

infinitesimal concentrations within a few tens of seconds acquisition time. The acquired SERS are then rapidly compared to the pre-established database and the reference samples, determining the specificity. While a significant correlation between plasma NAA levels and TBI progression yields possible prognostic value in patients with TBI prior to secondary impairment, a selective diagnostic blood test can be created based on a comparison of the obtained spectroscopic changes in the blood of the patient under evaluation with a developed library of Raman spectroscopic signatures for TBI and other diseases. MEDTech exhibits unique attributes and key advantages according to the “ASSURED” criteria, [178] which define an ideal diagnostic test for PoC (Table 6.5).

Table 6.5. Summary of MEDTech attributes, according to the ASSURED criteria.

MEDTech Unique Attributes	Related MEDTech Key Advantages
Affordable: Target cost of £10/test (achievable upon high mass production). Key enablers are a low-cost fabrication processes for the SERS and the microfluidics platforms.	To promote that screening for early disease diagnosis becomes a routine process, using MEDTech as a first screening step./To enable its routine use for TBI triage, impacting on improved patient outcomes and decreasing current over-triage and unnecessary CTs.
Sensitive: SERS offers a very high sensitivity for the quantification of target molecules at very low concentrations (*pico* to *femto* Molar), achieved from an accurate control of SERS substrate geometry and (possible) functionalisation, the implementation of portable mapping Raman spectrometer and the refinement of quantification computational models.	To enable a simple routine process, using just a finger prick blood sample, as a reliable method that offers: i) new neurological diagnostic capabilities (*i.e.,* detection of previously undetectable biomarkers in blood); and ii) diagnosis at earlier stages of the disorder (*i.e.,* when biomarker concentrations are lower and at the accident location).
Specific: Recent major progress of research on in-blood neurological biomarkers has enabled to set a panel of target biomolecules which is highly disease-specific. SERS's excellent multiplexity capacity enables simultaneous detection of the multiple biomolecules in the panels.	To enable a process where the reliable detection and quantification of biomarker panels and their interpretation assisted by predictive models, offer a more specific diagnosis and prognosis (*i.e.,* differentiation between different neurological disorders).
User-friendly: Use of microfluidics for integration of the sample preparation steps. Implementation of refined predictive models for determining diagnosis criteria based on measured biomarkers concentration and existing clinical data for patient. Device user interface and connectivity designed to enhance simplicity.	*For the user:* Test is easy to perform, with minimal training. The system also delivers an interpretation of the detected biomarkers concentration, enabling preliminary screening/triage by GPs/emergency services. *For the patient:* Use of blood instead of CFS, eliminates the need of painful lumbar puncture, making it no disturbing for the patients and suitable for the PoC.
Rapid and robust: Microfluidics optimised yield to enable sample preparation in <5min / Rapid SERS detection and complex computational analysis. Automatization enhances robustness with MEDTech (microfluidics and SERS substrate) validated for excellent reproducibility	Only finger prick sampling is needed (no need of phlebotomy), for a rapid, inexpensive and convenient sample collection and preparation. It enables lab-quality results in the detection of neurological biomarker panels by implementing a single-step automated detection process that eliminates variability sources.
Equipment free: A compact system delivered, comprising a reader (common for different neurological diseases) and disposable disease-specific cartridges. Consumption of subsystems (*p.e.,* Raman spectrometer) optimised to enable battery-powered.	Suitable for the PoC. The device has optional connectivity to enable use of cloud-based features and functionalities. The device will facilitate integration with standard software systems at the PoC (*e.g.*, EMR) to simplify data retrieval (*e.g.,* supplementary data for predictive models) and storage.
Deliverable where needed: A portable device developed. Portable Raman spectrometers are a mature technology, enabling SERS as the only high-resolution detection technique deployable at the PoC without a significant loss in performance.	To enable a device that can be used at the PoC. Initially, will be mainly at the Health Centres and the Emergency Services. Progressively, also in the Emergency Care units and even outside the healthcare context (*e.g.,* sport fields).

6.11 Conclusions

Traumatic brain injury is a devastating and debilitating injury with an early intervention being essential for positive outcomes. Detecting and monitoring of TBI is extremely difficult, time consuming and requiring large, hospital based and expensive equipment, with a CT scan currently being the 'gold standard'. When TBI occurs miniscule amounts of the brain specific, neuron biomarkers for instance, NAA, are released and cross the brain blood barrier into the blood stream. Our integrated MEDTech enables a detection of TBI indicative biomarkers from a single finger prick of blood dropped into the inlet area of the microfluidic chip. Using capillary action the blood is then drawn into the chip and the blood plasma is separated out and drawn into the special SERS active areas, comprised of the innovative and optimised RED substrates. The microfluidic chip is inserted into the MEDTech portable Raman setup where near infra-red, 785nm laser light is shone upon the SERS active area. The photons of light interact with the NAA molecular bonds, the electric fields of which have been enhanced by the gold covered RED-SERS substrate, changing the energy of a small fraction of the incident light and thus, scattering a certain amount of Raman light. The MEDTech platforms enable an average SERS enhancement factor on the order of 10^9 of the Raman signal for the NAA biomarker, allowing detection down to the sub-picomolar level, *i.e.,* 1.2×10^{-13}M from blood plasma. Integrating the SERS substrate within a carefully designed and engineered plasma separating microfluidic chip allows measurements to be processed within 2 to 3 minutes. The microfluidic chip subsequently inserted into the portable Raman system and a measurement is taken. The collected spectra are then compared to the reference spectra to determine the levels of the NAA in the blood stream thus, providing a clear

indication of the trauma state within the brain. The development of the TBI can be monitored as a function of time using our miniaturised MEDTech by doing repeat tests, rapidly and at low cost. Our technology lays a platform towards further development and engineering of miniaturised, versatile devices for a broad range of applications in the biomedical diagnostic field.

CHAPTER 7

Summary and Future Outlook

7.1 Summary

The research in this thesis has demonstrated that nano-patterning, using several different techniques, combined with a variety of exploited materials has the potential to produce many novel, miniaturised devices, at low-cost and in a straightforward manner, yet, with high-fidelity. Conventionally, photolithography has been the technique of choice for producing micrometre patterns, however, it is costly and time consuming, requires expensive, bulky equipment to produce the micro-to-nanometre scale structures. Herein, we have exploited the electrohydrodynamic lithography as an innovative and complimentary technique, which *via* using a reusable, patterned top electrode enables high-throughput, precise fabrication of structures with a broad range of sizes and morphologies on the micro and nano-scale. This lithographic technique is simple and cost-effective, which *via* inducing external high electric fields combined with a liquefied media is able to produce minute structures over large areas.

Nevertheless, we have also used combined lithographic methods of conventional photolithography with ion-beam lithography, to produce large area patterning combined with small area nano-patterning, accordingly, in order to

fabricate three-dimensional, hierarchical nanostructures required for the optofluidic chip in our MEDTech, which would be very difficult to achieve with a single lithographic technique. In this combined lithographic method, we have used traditional printed circuit board lithography for simplicity and low-cost, using a copper substrate combined with simple ferric chloride etching to produce the large area patterning for a microfluidic chip. Subsequently, using the ion-beam lithography on the copper master enabled the production of the sub-micron filter structures with a smaller etch depth and width than could have been fabricated *via* the photolithography alone. These advanced lithographic methods, optimised in this work, have then been employed for the development and fabrication of micro-engineered device technologies for two major applications, vertical, conductive-polymer based FETs and MEDTech for point-of-care diagnostics of TBI.

Vertical field effect transistors provide an advanced route towards increasing the transistor's density, which is essential as we approach the limit of horizontal FETs. Development and fabrication of such transistors directly and effectively from conductive polymers by using the electrohydrodynamic lithography, lays a platform for many possibilities towards production of flexible, miniaturised electronics, wearable sensors and portable displays. In Chapter 4, we have successfully demonstrated functional vertical field effect transistors on the scale of 700nm gate size with a maximum current carrying capacity of 20mA at 4V, yielding a maximum power of 80mW per gate. Careful selection of the experimental and setup parameters, the sizes of patterned top substrate structures, the initial thickness of conductive polymer layer, air gap distance between the two electrodes in the patterning device and the strength of the applied electric field, it should be possible to further reduce the gate size of these FETs.

In Chapter 6, the EHL was exploited to engineer and optimise a device technology for diagnosis of traumatic brain injury, *i.e.,* the micro-engineered device technology (MEDTech). Using the electrohydrodynamic lithography we have fabricated reproducible and innovative, single polymer, gold-coated, nano-sized surface enhanced Raman substrates with enhanced performance. These RED-SERS active substrates are tuneable, we are able to change the SERS substrate structure size and spacing by designing different EHD top electrodes to give different enhancement, to yield surface Raman enhancements at different wavelengths. These RED substrates were shown to efficiently enhance the *N*-acetylaspartate signal, a brain neuron specific biomarker, levels of which have been shown to change as a result of TBI. This biomarker is released in minute amounts into the blood stream when traumatic brain injury occurs. Following the development and engineering, we have incorporated these substrates within a microfluidic chip, capable of using a single pin-prick of blood and, *via* the capillary action, separate out the plasma and direct it onto the RED-SERS substrates, allowing us to detect down to picomolar concentrations of the TBI indicative biomarkers particularly NAA. Finally this optofluidic lab-on-a-chip, comprised of the RED-SERS substrates with the microfluidic chip, was inserted into our developed portable Raman device, the MEDTech reader, and within several minutes yielded results indicating whether the patient has signs of early stages of traumatic brain injury or not. The RED substrates can be stored for more than six months without performance degradation, invaluable for employing these for rapid, point-of-care diagnostics and reducing the costs.

7.2 Future Outlook

There are several further development steps that could be undertaken to further improve the vertical FETs. So far the polypyrrole-based vertical field effect transistors have only been produced on a silicon substrate, however, to create flexible electronics, these will need to be produced on a flexible polymer supporting substrates. Furthermore, in our study, we have used potassium hydroxide as the ionic conducting liquid gate however, to be exploited for flexible electronics, a solid gate material with semiconducting properties is essential.

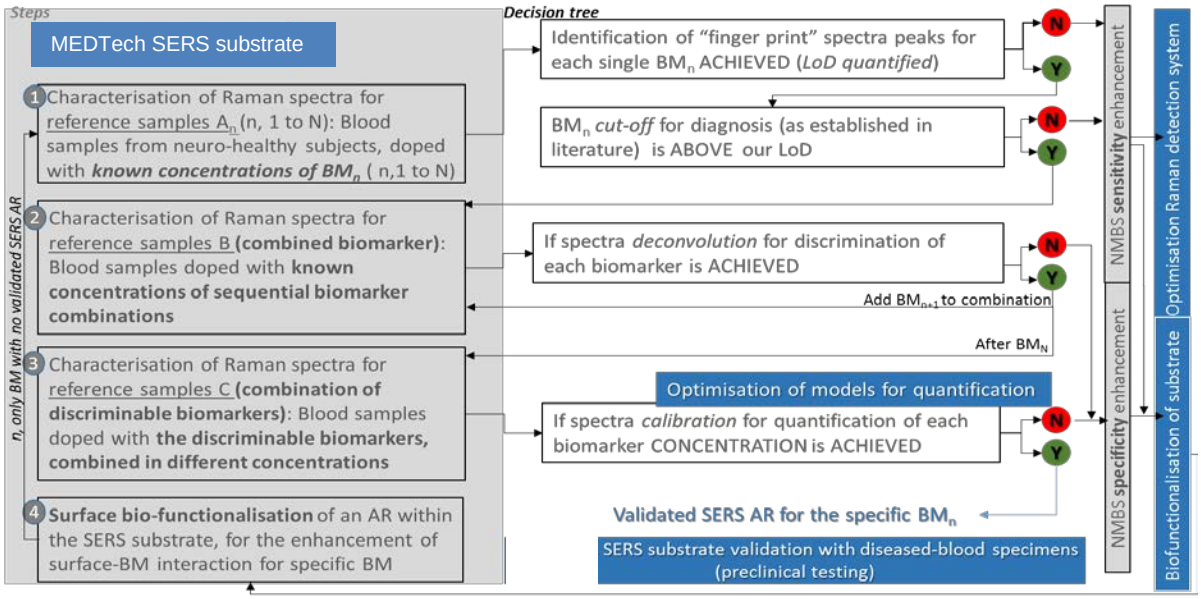

Figure 7.1: Methodology for optimization of a RED substrate for SERS detection of up to *N* biomarkers (BM). Multiplex, ideally under a single excitation wavelength and specificity for the quantification of each target biomolecule are required. This methodology is further used for tailoring the SERS substrate to the target biomarkers (BMs) and defining the required active regions (AR) on the substrate, as a function of multiple surface functionalization, where further required.

Finally, further reduction in dimensions of the polypyrrole-based structures could be achieved *via* an optimization of the EHL, by reducing the structures' size on the

patterned top substrate, reducing the polypyrrole film thickness or the air gap and increasing the electric field strength.

Several optimisation processes and modifications could also be further implemented to improve the MEDTech and accelerate its application for clinical use (Figure 7.1).

First, discriminated multiplex-detection from complex biofluids can be tackled by applying advanced scanning optics for excitation while controlling a sequential beam focusing on specific pillars of the electrohydrodynamically generated structures. We can therefore, fabricate the next-generation, tuneable structural arrays with slight variations in aspect ratios between the adjacent areas which can further be coupled with advanced optical arrangements and functionalization with different capture molecules on each pillar, using molecular bio-imprinting. Secondly, we are currently developing and engineering an advanced detection optics system, which will enable individual SERS spectra to be measured from each active region with individual calibration models. In this manner, the concentration of each biomarker will be established independently, offering a biomarker panel to the clinical users. This advanced optics will be integrated in the MEDTech portable reader to enable laser excitation and spectrum measurement from each active region on the SERS substrate independently. The laser beam will be focused to a spot size smaller than the region, confirm it is focused entirely in the required area combined with mechatronics integrated to automatically and sequentially focus the beam in each different region for each biomarker measurement and then will be scanned between the regions of the SERS substrates using a combination of stepper motors and mirrors from which the excitation beam will pass through each region then pause take a measurement and then move on to the next differently functionalized SERS

area. The SERS-signal will be recorded in a back-scattering geometry using the high numerical aperture scan lens and diverted to the spectrometer from the excitation beam using specially designed sharp edge or holographic notch filters. Importantly, the versatility of the MEDTech technological platform will make it further applicable in many clinical areas and might accelerate the successful early-diagnosis of various major diseases due to detecting biomarkers at very low concentration levels.

References

1. **John Bardeen**. Wikipedia: **2017**.
2. Hendra, P., **THE DISCOVERY OF SERS: an idiosyncratic account from a vibrational spectroscopist**. *Analyst* **2016,** *141* (17), 4996-4999.
3. (a) Aten, Q. T.; Jensen, B. D.; Burnett, S. H.; Howell, L. L., **A self-reconfiguring metamorphic nanoinjector for injection into mouse zygotes**. *Review of Scientific Instruments* **2014,** *85* (5), 055005; (b) Hanay, M. S.; KelberS; Naik, A. K.; ChiD; HentzS; Bullard, E. C.; ColinetE; DuraffourgL; Roukes, M. L., **Single-protein nanomechanical mass spectrometry in real time**. *Nat Nano* **2012,** *7* (9), 602-608; (c) Wu, C.; Lin, T. G.; Zhan, Z.; Li, Y.; Tung, S. C. H.; Tang, W. C.; Li, W. J., **Fabrication of all-transparent polymer-based and encapsulated nanofluidic devices using nano-indentation lithography**. **2017,** *3*, 16084.
4. Smith, B. F., Yongfa; Slocum, Michael; and Zavyalova, Lena,, **25nm Immersion lithography at a 193nm wavelength**. *SPIE* **2005,** *5754*, 141-147.
5. Pease, R. F. W., **Electron beam lithography**. *Contemporary Physics* **1981,** *22* (3), 265-290.
6. Backer, E. W.; Ehrfeld, W.; Münchmeyer, D.; Betz, H.; Heuberger, A.; Pongratz, S.; Glashauser, W.; Michel, H. J.; v. Siemens, R., **Production of separation-nozzle systems for uranium enrichment by a combination of X-ray lithography and galvanoplastics**. *Naturwissenschaften* **1982,** *69* (11), 520-523.
7. Latif, A. **NANOFABRICATION USING FOCUSED ION BEAM.** University of Cambridge, **2000**.
8. Oppenheimer, P. G. **Electrohydrodynamic Patterning of Functional Materials.** University of Cambridge, **2011**.
9. Sandison, M. E. **Micro- and Nano-Electrode Arrays For Electroanalytical Sensing.** University of Glasgow, **2004**.
10. Leuschner, R.; Pawlowski, G., Photolithography. In *Materials Science and Technology*, Wiley-VCH Verlag GmbH & Co. KGaA: 2006.
11. Corporation, I., **From Sand to Silicon "Making of a Chip"**. **2011**.
12. Ito, T.; Okazaki, S., **Pushing the limits of lithography**. *Nature* **2000,** *406* (6799), 1027-31.
13. **Photolithography**. In *wikipedia*, **2017**.
14. Corporation, I. **Immersion lithography**. **2002**.
15. Yayi, W. D., Back, **193nm immersion lithography: Status and challenges**. SPIE, **2007**.
16. Bohr, M., **Intel 32nm Technology**. Intel Corporation.
17. G.R.Brewer, ***Electron Beam Technology in Microelectronic Fabrication***. Academic press inc: **1980**.
18. Vieu, C.; Carcenac, F.; Pépin, A.; Chen, Y.; Mejias, M.; Lebib, A.; Manin-Ferlazzo, L.; Couraud, L.; Launois, H., **Electron beam lithography: resolution limits and applications**. *Applied Surface Science* **2000,** *164* (1), 111-117.

19. Escovitz, W. H.; Fox, T. R.; Levi-Setti, R., **Scanning transmission ion microscope with a field ion source**. *Proc Natl Acad Sci U S A* **1975,** *72* (5), 1826-8.
20. Seliger, R. L.; Ward, J. W.; Wang, V.; Kubena, R. L., **A high-intensity scanning ion probe with submicrometer spot size**. *Applied Physics Letters* **1979,** *34* (5), 310-312.
21. Orloff, J., **High-resolution focused ion beams**. *Review of Scientific Instruments* **1993,** *64* (5), 1105-1130.
22. Melngailis, J., **Focused ion beam lithography**. *Nuclear Instruments and Methods in Physics Research Section B: Beam Interactions with Materials and Atoms* **1993,** *80*, 1271-1280.
23. Wanzenboeck, H. D.; Waid, S., ***Focused Ion Beam Lithography, Recent Advances in Nanofabrication Techniques and Applications***. **2011**.
24. Whitesides, G. M.; Mathias, J. P.; Seto, C. T., **Molecular self-assembly and nanochemistry: a chemical strategy for the synthesis of nanostructures**. *Science (New York, N.Y.)* **1991,** *254* (5036), 1312-1319.
25. Yan, H.; Park, S. H.; Finkelstein, G.; Reif, J. H.; LaBean, T. H., **DNA-templated self-assembly of protein arrays and highly conductive nanowires**. *Science* **2003,** *301* (5641), 1882-4.
26. Antonietti, M.; Förster, S., **Vesicles and Liposomes: A Self-Assembly Principle Beyond Lipids**. *Advanced Materials* **2003,** *15* (16), 1323-1333.
27. Jean, J.; Garcia-Pérez, M. E.; Pouliot, R., **Bioengineered Skin: The Self-Assembly Approach**. *Journal of Tissue Science & Engineering* **2011,** (S5:001), 2157-7552.
28. Lee, O. P.; Yiu, A. T.; Beaujuge, P. M.; Woo, C. H.; Holcombe, T. W.; Millstone, J. E.; Douglas, J. D.; Chen, M. S.; Fréchet, J. M. J., **Efficient Small Molecule Bulk Heterojunction Solar Cells with High Fill Factors via Pyrene-Directed Molecular Self-Assembly**. *Advanced Materials* **2011,** *23* (45), 5359-5363.
29. YanMing, F.; Jie, C.; HuaJie, L.; ChunHai, F., **Programmed self-assembly of DNA origami nanoblocks into anisotropic higher-order nanopatterns**. *Chinese Science Bulletin* **2013,** *58* (21), 2646.
30. Chou, S. Y.; Krauss, P. R.; Renstrom, P. J., **Nanoimprint lithography**. *Journal of Vacuum Science & Technology B: Microelectronics and Nanometer Structures Processing, Measurement, and Phenomena* **1996,** *14* (6), 4129-4133.
31. Oppenheimer, P. G., ***Structural Hierarchy of Functional Block Copolymer System Induced by Electrohydrodynamic Lithography***. Springer: **2013**.
32. Goldberg-Oppenheimer, P.; Steiner, U., **Rapid electrohydrodynamic lithography using low-viscosity polymers**. *Small* **2010,** *6* (11), 1248-54.
33. Gehrke, I.; Geiser, A.; Somborn-Schulz, A., **Innovations in nanotechnology for water treatment**. *Nanotechnology, Science and Applications* **2015,** *8*, 1-17.
34. Hirsch, L. R.; Stafford, R. J.; Bankson, J. A.; Sershen, S. R.; Rivera, B.; Price, R. E.; Hazle, J. D.; Halas, N. J.; West, J. L., **Nanoshell-mediated near-infrared thermal therapy of tumors under magnetic resonance guidance**. *Proceedings of the National Academy of Sciences* **2003,** *100* (23), 13549-13554.
35. Liotta, L. A.; Ferrari, M.; Petricoin, E., **Clinical proteomics: written in blood**. *Nature* **2003,** *425* (6961), 905.

36. Ladd, T. D.; Jelezko, F.; Laflamme, R.; Nakamura, Y.; Monroe, C.; O'Brien, J. L., **Quantum computers**. *Nature* **2010,** *464* (7285), 45-53.
37. Lilienfeld, J. E. **Method and apparatus for controlling electric currents. 1930**.
38. Koezuka, H.; Tsumura, A.; Ando, T., **Field-effect transistor with polythiophene thin film**. *Synthetic Metals* **1987,** *18* (1), 699-704.
39. Wanekaya, A. K.; Bangar, M. A.; Yun, M.; Chen, W.; Myung, N. V.; Mulchandani, A., **Field-Effect Transistors Based on Single Nanowires of Conducting Polymers**. *The Journal of Physical Chemistry C* **2007,** *111* (13), 5218-5221.
40. Ramanathan, K.; Bangar, M. A.; Yun, M.; Chen, W.; Mulchandani, A.; Myung, N. V., **Individually Addressable Conducting Polymer Nanowires Array**. *Nano Letters* **2004,** *4* (7), 1237-1239.
41. Bufon, C. C. B.; Heinzel, T., **Polypyrrole thin-film field-effect transistor**. *Applied Physics Letters* **2006,** *89* (1), 012104.
42. Lee, M. S.; Kang, H. S.; Kang, H. S.; Joo, J.; Epstein, A. J.; Lee, J. Y., **Flexible all-polymer field effect transistors with optical transparency using electrically conducting polymers**. *Thin Solid Films* **2005,** *477* (1), 169-173.
43. Stutzmann, N.; Friend, R. H.; Sirringhaus, H., **Self-aligned, vertical-channel, polymer field-effect transistors**. *Science* **2003,** *299* (5614), 1881-4.
44. Knopfmacher, O.; Hammock, M. L.; Appleton, A. L.; Schwartz, G.; Mei, J.; Lei, T.; Pei, J.; Bao, Z., **Highly stable organic polymer field-effect transistor sensor for selective detection in the marine environment**. *Nat Commun* **2014,** *5*, 2954.
45. Johnston, D. E.; Yager, K. G.; Nam, C.-Y.; Ocko, B. M.; Black, C. T., **One-Volt Operation of High-Current Vertical Channel Polymer Semiconductor Field-Effect Transistors**. *Nano Letters* **2012,** *12* (8), 4181-4186.
46. Lee, S.-Y.; Lee, S.-K.; Lim, H.; Choi, G.-R., ***Irreversible Degradation Behaviors of an Electrolyte-gated Polyaniline (PANI) Nanowire Field-effect Transistor***. **2011**; Vol. 5780.
47. **Light**. https://en.wikipedia.org/wiki/Light (accessed 10-9-2017).
48. Strutt, J., **On the light from the sky, its polarization and colour**. *Philosophical Magazine* **1871,** *41*, 107-120.
49. Raman, C. V.; Krishnan, K. S., **A New Type of Secondary Radiation**. *Nature* **1928,** *121* (3048), 501-502.
50. Stokes, G. G., **On the Change of Refrangibility of Light**. *Philosophical Transactions of the Royal Society of London* **1852,** *142*, 463-562.
51. Ferraro, J. R.; Nakamoto, K.; Brown, C. W., In *Introductory Raman Spectroscopy (Second Edition)*, Nakamoto, K.; Brown, C. W., Eds. Academic Press: San Diego, 2003; p x.
52. Fleischmann, M.; Hendra, P. J.; McQuillan, A. J., **Raman spectra of pyridine adsorbed at a silver electrode**. *Chemical Physics Letters* **1974,** *26* (2), 163-166.
53. Albrecht, M. G.; Creighton, J. A., **Anomalously intense Raman spectra of pyridine at a silver electrode**. *Journal of the American Chemical Society* **1977,** *99* (15), 5215-5217.
54. Jeanmaire, D. L.; Van Duyne, R. P., **Surface raman spectroelectrochemistry**. *Journal of Electroanalytical Chemistry and Interfacial Electrochemistry* **1977,** *84* (1), 1-20.

55. Kneipp, K.; Kneipp, H.; Itzkan, I.; Dasari, R. R.; Feld, M. S., **Ultrasensitive Chemical Analysis by Raman Spectroscopy**. *Chemical Reviews* **1999,** *99* (10), 2957-2976.
56. Ru, E. L.; Etchegoin, P., ***Principles of Surface-Enhanced Raman Spectroscopy 1st Edition***. Elsevier Science: **2008**.
57. Kelly, K. L.; Coronado, E.; Zhao, L. L.; Schatz, G. C., **The Optical Properties of Metal Nanoparticles: The Influence of Size, Shape, and Dielectric Environment**. *The Journal of Physical Chemistry B* **2003,** *107* (3), 668-677.
58. Sharma, B.; Frontiera, R. R.; Henry, A.-I.; Ringe, E.; Van Duyne, R. P., **SERS: Materials, applications, and the future**. *Materials Today* **2012,** *15* (1), 16-25.
59. Moskovits, M., **Persistent misconceptions regarding SERS**. *Physical Chemistry Chemical Physics* **2013,** *15* (15), 5301-5311.
60. Larsson, K.; Hellgren, L., **A study of the combined Raman and fluorescence scattering from human blood plasma**. *Experientia* **1974,** *30* (5), 481-3.
61. Hoey, S.; Brown, D. H.; McConnell, A. A.; Smith, W. E.; Marabani, M.; Sturrock, R. D., **Resonance Raman spectroscopy of hemoglobin in intact cells: A probe of oxygen uptake by erythrocytes in rheumatoid arthritis**. *Journal of Inorganic Biochemistry* **1988,** *34* (3), 189-199.
62. Ozaki, Y., **Medical Application of Raman Spectroscopy**. *Applied Spectroscopy Reviews* **1988,** *24* (3-4), 259-312.
63. Wang, S. Y.; Hasty, C. E.; Watson, P. A.; Wicksted, J. P.; Stith, R. D.; March, W. F., **Analysis of metabolites in aqueous solutions by using laser Raman spectroscopy**. *Appl Opt* **1993,** *32* (6), 925-9.
64. Berger, A. J.; Wang, Y.; Feld, M. S., **Rapid, noninvasive concentration measurements of aqueous biological analytes by near-infrared Raman spectroscopy**. *Appl Opt* **1996,** *35* (1), 209-12.
65. Lorén, A.; Eliasson, C.; Josefson, M.; Murty, K. V. G. K.; Käll, M.; Abrahamsson, J.; Abrahamsson, K., **Feasibility of quantitative determination of doxorubicin with surface-enhanced Raman spectroscopy**. *Journal of Raman Spectroscopy* **2001,** *32* (11), 971-974.
66. Enejder, A. M. K.; Koo, T.-W.; Oh, J.; Hunter, M.; Sasic, S.; Feld, M. S.; Horowitz, G. L., **Blood analysis by Raman spectroscopy**. *Optics Letters* **2002,** *27* (22), 2004-2006.
67. Lyandres, O.; Shah, N. C.; Yonzon, C. R.; Walsh, J. T., Jr.; Glucksberg, M. R.; Van Duyne, R. P., **Real-time glucose sensing by surface-enhanced Raman spectroscopy in bovine plasma facilitated by a mixed decanethiol/mercaptohexanol partition layer**. *Anal Chem* **2005,** *77* (19), 6134-9.
68. Premasiri, W. R.; Lee, J. C.; Ziegler, L. D., **Surface-Enhanced Raman Scattering of Whole Human Blood, Blood Plasma, and Red Blood Cells: Cellular Processes and Bioanalytical Sensing**. *The Journal of Physical Chemistry B* **2012,** *116* (31), 9376-9386.
69. Bonifacio, A.; Dalla Marta, S.; Spizzo, R.; Cervo, S.; Steffan, A.; Colombatti, A.; Sergo, V., **Surface-enhanced Raman spectroscopy of blood plasma and serum using Ag and Au nanoparticles: a systematic study**. *Anal Bioanal Chem* **2014,** *406* (9-10), 2355-65.

70. Luukinen, H.; Herala, M.; Koski, K.; Kivela, S. L.; Honkanen, R., **Rapid increase of fall-related severe head injuries with age among older people: a population-based study**. *J Am Geriatr Soc* **1999,** *47* (12), 1451-2.
71. Maas, A. I. R., **Traumatic brain injury: simple data collection will improve the outcome**. *Wiener Klinische Wochenschrift* **2007,** *119* (1-2), 20-22.
72. **Major trauma care in England Report by the Comptroller and auditor General**. **2010;** Vol. hc 213 Session.

73. OH, E. J.; JANG, K. S. **METHOD FOR MAKING POLYPYRROLE**. **2002**.
74. Jung, G.-Y.; Li, Z.; Wu, W.; Chen, Y.; Olynick, D. L.; Wang, S.-Y.; Tong, W. M.; Williams, R. S., **Vapor-Phase Self-Assembled Monolayer for Improved Mold Release in Nanoimprint Lithography**. *Langmuir* **2005,** *21* (4), 1158-1161.
75. Kimura, W. D.; Kim, G. H.; Balick, B., **Comparison of Laser and CO₂ Snow for Cleaning Large Astronomical Mirrors**. *Publications of the Astronomical Society of the Pacific* **1995,** *107* (715), 888-895.
76. Sherman, R.; Adams, P. In *Carbon Dioxide Snow Cleaning - The Next Generation of Clean*, Precision Cleaning, 1995.
77. In *{Cleaning large optics with CO2 snow}*, {SPIE Astronomical Telescopes and Instrumentation for the 21st Century}, SPIE: 1990; p {}.
78. Hall, D. B.; Underhill, P.; Torkelson, J. M., **Spin coating of thin and ultrathin polymer films**. *Polymer Engineering & Science* **1998,** *38* (12), 2039-2045.
79. FEI, **Product Data Helios NanoLab™ 650**. **2012**.
80. Orloff, J.; Swanson, L. W.; Utlaut, M., **Fundamental limits to imaging resolution for focused ion beams**. *Journal of Vacuum Science & Technology B: Microelectronics and Nanometer Structures Processing, Measurement, and Phenomena* **1996,** *14* (6), 3759-3763.
81. Sia, S. K.; Whitesides, G. M., **Microfluidic devices fabricated in Poly(dimethylsiloxane) for biological studies**. *ELECTROPHORESIS* **2003,** *24* (21), 3563-3576.
82. Whitesides, G. M., **The origins and the future of microfluidics**. *Nature* **2006,** *442* (7101), 368-373.
83. Marchington, R. F. **Applications of microfluidic chips in optical manipulation & photoporation.** University of St. Andrews, **2010**.
84. Turgeon, M. L., ***Clinical Hematology: Theory And Procedures***. Lippincott Williams and Wilkins: **1998**.
85. McMullan, D., **Scanning electron microscopy 1928–1965**. *Scanning* **1995,** *17* (3), 175-185.
86. Binnig, G.; Quate, C. F.; Gerber, C., **Atomic Force Microscope**. *Physical Review Letters* **1986,** *56* (9), 930-933.

87. Oppenheimer, P. G., ***Electrohydrodynamic Patterning of Functional Materials***. Springer International Publishing: **2013**.
88. Nazaripoor, H.; Koch, C. R.; Sadrzadeh, M.; Bhattacharjee, S., **Thermo-Electrohydrodynamic Patterning in Nanofilms**. *Langmuir* **2016,** *32* (23), 5776-5786.
89. Swan, J. W., **Stress and other Effects Produced in Resin and in a Viscid Compound of Resin and Oil by Electrification**. *Proceedings of the Royal Society* **1897,** *62* (38), 379-387.
90. Schäffer, E. **Instabilities in Thin Polymer Films:Structure Formation and Pattern Transfer.** der Universitat Konstanz., **2001**.

91. Goldberg-Oppenheimer, P.; Steiner, U., **Rapid electrohydrodynamic lithography using low-viscosity polymers**. *Small* **2010,** *6* (11), 1248-54.
92. Voicu, N. E.; Harkema, S.; Steiner, U., **Electric-Field-Induced Pattern Morphologies in Thin Liquid Films**. *Advanced Functional Materials* **2006,** *16* (7), 926-934.
93. Teletzke, G. F.; Davis, H. T.; Scriven, L. E., **Wetting hydrodynamics**. *Rev. Phys. Appl. (Paris)* **1988,** *23* (6), 989-1007.
94. Oppenheimer, P. G. **Electrohydrodynamic Patterning of Functional Materials.** University of Cambridge, **2011**
95. Katz, E.; Willner, I.; Wang, J., **Electroanalytical and Bioelectroanalytical Systems Based on Metal and Semiconductor Nanoparticles**. *Electroanalysis* **2004,** *16* (1-2), 19-44.
96. Sonmez, G.; Sonmez, H. B.; Shen, C. K. F.; Wudl, F., **Red, Green, and Blue Colors in Polymeric Electrochromics**. *Advanced Materials* **2004,** *16* (21), 1905-1908.
97. Katz, H. E., **Chemically Sensitive Field-Effect Transistors and Chemiresistors: New Materials and Device Structures**. *Electroanalysis* **2004,** *16* (22), 1837-1842.
98. Wang, J. Z.; Zheng, Z. H.; Li, H. W.; Huck, W. T. S.; Sirringhaus, H., **Dewetting of conducting polymer inkjet droplets on patterned surfaces**. *Nat Mater* **2004,** *3* (3), 171-176.
99. Dong, B.; Zhong, D. Y.; Chi, L. F.; Fuchs, H., **Patterning of Conducting Polymers Based on a Random Copolymer Strategy: Toward the Facile Fabrication of Nanosensors Exclusively Based on Polymers**. *Advanced Materials* **2005,** *17* (22), 2736-2741.
100. Langridge, M., Samsung: No OLED TVs in 2015. *WHAT HI*FI?* 2014.
101. Tarr, G., **How TV Manufacturers Can Get to an OLED Future**. In *The Weekly Riff*, Digital Tech Consulting Inc: **2016**.
102. Lee, J., **LG Display to take on Samsung as it lifts OLED investment**. Thomson Reuters: **2017**.
103. III, L. F. P.; Russel, W. B., **Charge driven, electrohydrodynamic patterning of thin films**. *The Journal of Chemical Physics* **2006,** *125* (18), 184716.
104. Pease, L.; Russel, W., ***Linear stability analysis of thin leaky dielectric films subjected to electric fields***. **2002**; Vol. 102, p 233-250.
105. III, L. F. P.; Russel, W. B., **Electrostatically induced submicron patterning of thin perfect and leaky dielectric films: A generalized linear stability analysis**. *The Journal of Chemical Physics* **2003,** *118* (8), 3790-3803.
106. Schaffer, E.; Thurn-Albrecht, T.; Russell, T. P.; Steiner, U., **Electrically induced structure formation and pattern transfer**. *Nature* **2000,** *403* (6772), 874-877.
107. Mahajan, S.; Hutter, T.; Steiner, U.; Goldberg Oppenheimer, P., **Tunable Microstructured Surface-Enhanced Raman Scattering Substrates via Electrohydrodynamic Lithography**. *The Journal of Physical Chemistry Letters* **2013,** *4* (23), 4153-4159.
108. Goldberg-Oppenheimer, P.; Steiner, U., **Rapid Electrohydrodynamic Lithography Using Low-Viscosity Polymers**. *Small* **2010,** *6* (11), 1248-1254.
109. Oppenheimer, P. G., ***Electrohydrodynamic Patterning of Functional Materials***. Springer International Publishing: **2013**.

110. Ciobotaru, I. C.; Matei, E.; Ciobotaru, C. C.; Polosan, S., **Embedding of IrQ(ppy)2 organometallic compounds in polypyrrole conducting polymer for OLED's applications**. *Synthetic Metals* **2014,** *198*, 323-328.
111. OH, E. J.; JANG, K. S. **METHOD FOR MAKING POLYPYRROLE**. **2002**.
112. Harkema, S.; Steiner, U., **Hierarchical Pattern Formation in Thin Polymer Films Using an Electric Field and Vapor Sorption**. *Advanced Functional Materials* **2005,** *15* (12), 2016-2020.
113. Morariu, M. D.; Voicu, N. E.; Schaffer, E.; Lin, Z.; Russell, T. P.; Steiner, U., **Hierarchical structure formation and pattern replication induced by an electric field**. *Nat Mater* **2003,** *2* (1), 48-52.
114. Armes, S. P., **Optimum reaction conditions for the polymerization of pyrrole by iron(III) chloride in aqueous solution**. *Synthetic Metals* **1987,** *20* (3), 365-371.
115. Campbell, T. E.; Hodgson, A. J.; G.G.Wallace, **Incorporation of Erythrocytes into Polypyrrole to Form the Basis of a Biosensor to Screen for Rhesus (D) Blood Groups and Rhesus (D) Antibodies**. *Electroanalysis* **1999,** *11* (4), 215-222.
116. Diaz, A. F.; Kanazawa, K. K.; Gardini, G. P., **Electrochemical polymerization of pyrrole**. *Journal of the Chemical Society, Chemical Communications* **1979,** (14), 635-636.
117. Oh, E. J.; Jang, K. S.; Park, S. Y.; Han, S. S.; Suh, J. S., **Electrochemical Synthesis and Characterization of Strechable Polypyrrole Films**. *Molecular Crystals and Liquid Crystals Science and Technology. Section A. Molecular Crystals and Liquid Crystals* **2001,** *371* (1), 243-246.
118. Ateh, D. D.; Navsaria, H. A.; Vadgama, P., **Polypyrrole-based conducting polymers and interactions with biological tissues**. *Journal of the Royal Society Interface* **2006,** *3* (11), 741-752.
119. Harkema, S. **Capillary instabilities in thin polymer films: Mechanism of structure formation and pattern replication.** University of Groningen, **2006**.
120. Goldberg-Oppenheimer, P.; Eder, D.; Steiner, U., **Carbon Nanotube Alignment via Electrohydrodynamic Patterning of Nanocomposites**. *Advanced Functional Materials* **2011,** *21* (10), 1895-1901.
121. Goldberg-Oppenheimer, P.; Mahajan, S.; Steiner, U., **Hierarchical Electrohydrodynamic Structures for Surface-Enhanced Raman Scattering**. *Advanced Materials* **2012,** *24* (23), OP175-OP180.
122. Al-Kaysi, R. O.; Ghaddar, T. H.; Guirado, G., **Fabrication of One-Dimensional Organic Nanostructures Using Anodic Aluminum Oxide Templates**. *Journal of Nanomaterials* **2009,** *2009*, 14.
123. Yeonho, I.; Richard, P. V.; Choonsup, L.; Nosang, M.; Reginald, P.; Minhee, Y., **Single metal and conducting polymer nanowire sensors for chemical and DNA detections**. *Journal of Physics: Conference Series* **2006,** *38* (1), 61.
124. Lee, M. S.; Kang, H. S.; Kang, H. S.; Joo, J.; Epstein, A. J.; Lee, J. Y., **Flexible all-polymer field effect transistors with optical transparency using electrically conducting polymers**. *Thin Solid Films* **2005,** *477* (1), 169-173.
125. Alam, M. M.; Wang, J.; Guo, Y.; Lee, S. P.; Tseng, H.-R., **Electrolyte-Gated Transistors Based on Conducting Polymer Nanowire Junction Arrays**. *The Journal of Physical Chemistry B* **2005,** *109* (26), 12777-12784.

126. Mathyssen, H., **http://users.telenet.be/StraffeH/Teksten/Spectrometry.htm**.

127. wikipedia **Electromagnetic radiation**. https://en.wikipedia.org/wiki/Electromagnetic_radiation.
128. Eichinger, I.; Schmitz-Esser, S.; Schmid, M.; R. Fisher, C.; Bright, M., ***Symbiont-Driven Sulfur Crystal Formation in a Thiotrophic Symbiosis from Deep-Sea Hydrocarbon Seeps***. **2014**; Vol. 6.
129. El-Abassy, R. M.; von der Kammer, B.; Materny, A., **UV Raman spectroscopy for the characterization of strongly fluorescing beverages**. *LWT - Food Science and Technology* **2015,** *64* (1), 56-60.
130. Fujiwara, M.; Hamaguchi, H.; Tasumi, M., **Measurements of Spontaneous Raman Scattering with Nd:YAG 1064-nm Laser Light**. *Applied Spectroscopy* **1986,** *40* (2), 137-139.
131. Front Matter A2 - Ferraro, John R. In *Introductory Raman Spectroscopy (Second Edition)*, Nakamoto, K.; Brown, C. W., Eds. Academic Press: San Diego, 2003; p iii.
132. Stokes, G. G., **On the Change of Refrangibility of Light**. *Philosophical Transactions of the Royal Society of London* **1852,** *142*, 463-562.
133. Fleischmann, M.; Hendra, P. J.; McQuillan, A. J., **Raman spectra of pyridine adsorbed at a silver electrode**. *Chemical Physics Letters* **1974,** *26* (2), 163-166.
134. Albrecht, M. G.; Creighton, J. A., **Anomalously intense Raman spectra of pyridine at a silver electrode**. *Journal of the American Chemical Society* **1977,** *99* (15), 5215-5217.
135. Jeanmaire, D. L.; Van Duyne, R. P., **Surface raman spectroelectrochemistry: Part I. Heterocyclic, aromatic, and aliphatic amines adsorbed on the anodized silver electrode**. *Journal of Electroanalytical Chemistry and Interfacial Electrochemistry* **1977,** *84* (1), 1-20.
136. Chulhai, D. V.; Hu, Z.; Moore, J. E.; Chen, X.; Jensen, L., **Theory of Linear and Nonlinear Surface-Enhanced Vibrational Spectroscopies**. *Annual Review of Physical Chemistry* **2016,** *67* (1), 541-564.
137. Polubotko, A. M.; Chelibanov, V. P., **The theory of Surface Enhanced Hyper Raman Scattering (A review)**. *Optics and Spectroscopy* **2016,** *120* (1), 86-108.
138. Lombardi, J. R.; Birke, R. L., **A Unified Approach to Surface-Enhanced Raman Spectroscopy**. *The Journal of Physical Chemistry C* **2008,** *112* (14), 5605-5617.
139. Hong, S.; Li, X., **Optimal Size of Gold Nanoparticles for Surface-Enhanced Raman Spectroscopy under Different Conditions**. *Journal of Nanomaterials* **2013,** *2013*, 9.
140. Guo, H.; Xing, B.; Hamlet, L. C.; Chica, A.; He, L., **Surface-enhanced Raman scattering detection of silver nanoparticles in environmental and biological samples**. *Sci Total Environ* **2016,** *554-555*, 246-52.
141. Muniz-Miranda, M.; Gellini, C.; Giorgetti, E., **Surface-Enhanced Raman Scattering from Copper Nanoparticles Obtained by Laser Ablation**. *The Journal of Physical Chemistry C* **2011,** *115* (12), 5021-5027.

142. Moffett, J. R.; Ross, B.; Arun, P.; Madhavarao, C. N.; Namboodiri, M. A. A., **N-Acetylaspartate in the CNS: From Neurodiagnostics to Neurobiology**. *Progress in neurobiology* **2007,** *81* (2), 89-131.
143. Wide, L.; Gemzell, C. A., **AN IMMUNOLOGICAL PREGNANCY TEST**. *Acta Endocrinologica* **1960,** *XXXV* (II), 261-267.
144. Clarke, S. F.; Foster, J. R., **A history of blood glucose meters and their role in self-monitoring of diabetes mellitus**. *Br J Biomed Sci* **2012,** *69* (2), 83-93.
145. Otoom, A. F.; Kefaye, A.; Ashour, M.; Shanti, Y.; Al-Majali, M., **Real-Time Monitoring of Patients with Coronary Artery Disease**. *International Journal of Future Computer and Communication* **2015,** *4* (3), 207-210.
146. Garnett, M. R.; Blamire, A. M.; Corkill, R. G.; Cadoux-Hudson, T. A. D.; Rajagopalan, B.; Styles, P., **Early proton magnetic resonance spectroscopy in normal-appearing brain correlates with outcome in patients following traumatic brain injury**. *Brain* **2000,** *123* (10), 2046-2054.
147. Ross, B. D.; Ernst, T.; Kreis, R.; Haseler, L. J.; Bayer, S.; Danielsen, E.; Blüml, S.; Shonk, T.; Mandigo, J. C.; Caton, W.; Clark, C.; Jensen, S. W.; Lehman, N. L.; Arcinue, E.; Pudenz, R.; Shelden, C. H., **1H MRS in acute traumatic brain injury**. *Journal of Magnetic Resonance Imaging* **1998,** *8* (4), 829-840.
148. Dash, P. K.; Zhao, J.; Hergenroeder, G.; Moore, A. N., **Biomarkers for the diagnosis, prognosis, and evaluation of treatment efficacy for traumatic brain injury**. *Neurotherapeutics* **2010,** *7* (1), 100-14.
149. Winn, H.; Winn, H., chapter 334 Critical Care Management of Traumatic Brain Injury. In *Youmans Neurological Surgery*, Saunders: 2011.
150. DeKosky , S. T.; Ikonomovic , M. D.; Gandy , S., **Traumatic Brain Injury — Football, Warfare, and Long-Term Effects**. *New England Journal of Medicine* **2010,** *363* (14), 1293-1296.
151. Carney, N.; Totten, A. M.; O'Reilly, C.; Ullman, J. S.; Hawryluk, G. W.; Bell, M. J.; Bratton, S. L.; Chesnut, R.; Harris, O. A.; Kissoon, N.; Rubiano, A. M.; Shutter, L.; Tasker, R. C.; Vavilala, M. S.; Wilberger, J.; Wright, D. W.; Ghajar, J., **Guidelines for the Management of Severe Traumatic Brain Injury, Fourth Edition**. *Neurosurgery* **2017,** *80* (1), 6-15.
152. A Aquino, C.; Woolen, S.; Steenburg, S. D., **Magnetic resonance imaging of traumatic brain injury: a pictorial review**. *Emergency Radiology* **2014,** *22*, 65-78.
153. Di Costanzo, A.; Trojsi, F.; Tosetti, M.; Giannatempo, G. M.; Nemore, F.; Piccirillo, M.; Bonavita, S.; Tedeschi, G.; Scarabino, T., **High-field proton MRS of human brain**. *European Journal of Radiology* **2003,** *48* (2), 146-153.
154. Xiong, K. L.; Zhu, Y. S.; Zhang, W. G., **Diffusion tensor imaging and magnetic resonance spectroscopy in traumatic brain injury: a review of recent literature**. *Brain Imaging Behav* **2014,** *8* (4), 487-96.
155. Diaz-Arrastia, R.; Wang, K. K. W.; Papa, L.; Sorani, M. D.; Yue, J. K.; Puccio, A. M.; McMahon, P. J.; Inoue, T.; Yuh, E. L.; Lingsma, H. F.; Maas, A. I. R.; Valadka, A. B.; Okonkwo, D. O.; Manley; the Track-Tbi Investigators, G. T.; Casey, i. S. S.; Cheong, M.; Cooper, S. R.; Dams-O'Connor, K.; Gordon, W. A.; Hricik, A. J.; Menon, D. K.; Mukherjee, P.; Schnyer, D. M.; Sinha, T. K.; Vassar, M. J., **Acute Biomarkers of Traumatic Brain Injury: Relationship between Plasma Levels of Ubiquitin C-Terminal Hydrolase-L1 and Glial Fibrillary Acidic Protein**. *Journal of Neurotrauma* **2013,** *31* (1), 19-25.

156. Bayir, H.; Tyurin, V. A.; Tyurina, Y. Y.; Viner, R.; Ritov, V.; Amoscato, A. A.; Zhao, Q.; Zhang, X. J.; Janesko-Feldman, K. L.; Alexander, H.; Basova, L. V.; Clark, R. S. B.; Kochanek, P. M.; Kagan, V. E., **Selective early cardiolipin peroxidation after traumatic brain injury: an oxidative lipidomics analysis**. *Annals of Neurology* **2007,** *62* (2), 154-169.
157. Zetterberg, H.; Smith, D. H.; Blennow, K., **Biomarkers of mild traumatic brain injury in cerebrospinal fluid and blood**. *Nat Rev Neurol* **2013,** *9* (4), 201-10.
158. Sharma, R.; Laskowitz, D. T., **Biomarkers in traumatic brain injury**. *Current neurology and neuroscience reports* **2012,** *12* (5), 560-569.
159. Papa, L.; Lewis, L. M.; Falk, J. L.; Zhang, Z.; Silvestri, S.; Giordano, P.; Brophy, G. M.; Demery, J. A.; Dixit, N. K.; Ferguson, I.; Liu, M. C.; Mo, J.; Akinyi, L.; Schmid, K.; Mondello, S.; Robertson, C. S.; Tortella, F. C.; Hayes, R. L.; Wang, K. K., **Elevated levels of serum glial fibrillary acidic protein breakdown products in mild and moderate traumatic brain injury are associated with intracranial lesions and neurosurgical intervention**. *Ann Emerg Med* **2012,** *59* (6), 471-83.
160. Sen, J.; Belli, A.; Petzold, A.; Russo, S.; Keir, G.; Thompson, E. J.; Smith, M.; Kitchen, N., ***Extracellular fluid S100B in the injured brain:a future surrogate marker of acute brain injury?*** Springer-Verlag: **2005**.
161. Thelin, E. P.; Jeppsson, E.; Frostell, A.; Svensson, M.; Mondello, S.; Bellander, B.-M.; Nelson, D. W., **Utility of neuron-specific enolase in traumatic brain injury; relations to S100B levels, outcome, and extracranial injury severity**. *Critical Care* **2016,** *20*, 285.
162. Barnes, W. L.; Dereux, A.; Ebbesen, T. W., **Surface plasmon subwavelength optics**. *Nature* **2003,** *424*, 824.
163. Kneipp, K.; Wang, Y.; Kneipp, H.; Perelman, L. T.; Itzkan, I.; Dasari, R. R.; Feld, M. S., **Single Molecule Detection Using Surface-Enhanced Raman Scattering (SERS)**. *Physical Review Letters* **1997,** *78* (9), 1667-1670.
164. Dinish, U. S.; Balasundaram, G.; Chang, Y. T.; Olivo, M., **Sensitive multiplex detection of serological liver cancer biomarkers using SERS-active photonic crystal fiber probe**. *Journal of Biophotonics* **2014,** *7* (11-12), 956-965.
165. Dinish, U. S.; Balasundaram, G.; Chang, Y. T.; Olivo, M., **Actively targeted in vivo multiplex detection of intrinsic cancer biomarkers using biocompatible SERS nanotags**. *Sci Rep* **2014,** *4*, 4075.
166. Kho, K.; Zhu Mei Qing, K.; Xiang Shen, Z.; Binte Ahmad, I.; Sing Chin Lim, S.; Mhaisalkar, S.; White, T.; Watt, F.; Chee Soo, K.; Olivo, M., ***Polymer-based microfluidics with surface-enhanced Raman-spectroscopy-active periodic metal nanostructures for biofluid analysis***. **2008**; Vol. 13, p 054026.
167. Granger, J. H.; Schlotter, N. E.; Crawford, A. C.; Porter, M. D., **Prospects for point-of-care pathogen diagnostics using surface-enhanced Raman scattering (SERS)**. *Chem Soc Rev* **2016,** *45* (14), 3865-82.
168. (a) Piorek, B. D.; Lee, S. J.; Santiago, J. G.; Moskovits, M.; Banerjee, S.; Meinhart, C. D., **Free-surface microfluidic control of surface-enhanced Raman spectroscopy for the optimized detection of airborne molecules**. *Proceedings of the National Academy of Sciences* **2007,** *104* (48), 18898-18901; (b) Qian, X.; Zhou, X.; Nie, S., **Surface-Enhanced Raman Nanoparticle Beacons Based on Bioconjugated Gold Nanocrystals and**

Long Range Plasmonic Coupling. *J. Am. Chem. Soc.* **2008,** *130* (45), 14934–14935; (c) Ackermann, L.; Althammer, A.; Born, R., **Catalytic Arylation Reactions by C□H Bond Activation with Aryl Tosylates**. *Angewandte Chemie International Edition* **2006,** *45* (16), 2619-2622; (d) Pennathur, S.; Fygenson, D., **Improving fluorescence detection in lab on chip devices**. *Lab on a Chip* **2008,** *8* (5), 649-652; (e) Kho, K.; Zhu Mei Qing, K.; Xiang Shen, Z.; Binte Ahmad, I.; Sing Chin Lim, S.; Mhaisalkar, S.; White, T.; Watt, F.; Chee Soo, K.; Olivo, M., **Polymer-based microfluidics with surface-enhanced Raman-spectroscopy-active periodic metal nanostructures for biofluid analysis**. *Journal of Biomedical Optics* **2008,** *13* (5), 054026; (f) Lim, C.; Hong, J.; Chung, B. G.; deMello, A. J.; Choo, J., **Optofluidic platforms based on surface-enhanced Raman scattering**. *Analyst* **2010,** *135* (5), 837-844.

169. Goldberg Oppenheimer, P.; Rickard, J. J. S.; Di-Pietro, V.; Belli, A. **Surface Enhanced Raman Scattering Apparatus and Method**. **2017**.
170. (a) Goldberg-Oppenheimer, P.; Mahajan, S.; Steiner, U., **Hierarchical Electrohydrodynamic Structures for Surface-Enhanced Raman Scattering**. *Advanced Materials* **2012,** *24* (23), OP175-OP180; (b) Goldberg Oppenheimer, P.; Rickard, J. J. S.; Di-Pietro, V.; Belli, A. **Surface Enhanced Raman Scattering Apparatus and Method**. **2017**.
171. (a) E.R., D.; B, R., ***Magnetic resonance spectroscopy diagnosis of neurological diseases***. Marcel Dekker, Inc: New York, **1999**; Vol. 1st Edition; (b) Tshibanda, J.-F. L.; Demertzi, A.; Soddu, A., Spectroscopy and Diffusion Tensor Imaging in Disorders of Consciousness. In *Coma and Disorders of Consciousness*, Schnakers, C.; Laureys, S., Eds. Springer London: London, 2012; pp 45-54; (c) Coon, A. L.; Arias-Mendoza, F.; Colby, G. P.; Cruz-Lobo, J.; Mocco, J.; Mack, W. J.; Komotar, R. J.; Brown, T. R.; Connolly, E. S., **Correlation of Cerebral Metabolites with Functional Outcome in Experimental Primate Stroke Using in Vivo ¹H-Magnetic Resonance Spectroscopy**. *American Journal of Neuroradiology* **2006,** *27* (5), 1053-1058; (d) Schuff, N.; Capizzano, A. A.; Du, A. T.; Amend, D. L.; O'Neill, J.; Norman, D.; Kramer, J.; Jagust, W.; Miller, B.; Wolkowitz, O. M.; Yaffe, K.; Weiner, M. W., **Selective reduction of N-acetylaspartate in medial temporal and parietal lobes in AD**. *Neurology* **2002,** *58* (6), 928-935; (e) Shannon, R. J.; van der Heide, S.; Carter, E. L.; Jalloh, I.; Menon, D. K.; Hutchinson, P. J.; Carpenter, K. L. H., **Extracellular N-Acetylaspartate in Human Traumatic Brain Injury**. *Journal of Neurotrauma* **2016,** (33), 319–329.
172. (a) Hoshino, H.; Kubota, M., **Canavan disease: Clinical features and recent advances in research**. *Pediatrics International* **2014,** *56* (4), 477-483; (b) Di Pietro, V.; Cavallari, U.; Amorini, A. M.; Lazzarino, G.; Longo, S.; Poggiani, C.; Cavalli, P.; Tavazzi, B., **New T530C mutation in the aspartoacylase gene caused Canavan disease with no correlation between severity and N-acetylaspartate excretion**. *Clinical Biochemistry* **2013,** *46* (18), 1902-1904.
173. Park, A.; Baek, S.-J.; Shen, A.; Hu, J., **Detection of Alzheimer's disease by Raman spectra of rat's platelet with a simple feature selection**. *Chemometrics and Intelligent Laboratory Systems* **2013,** *121* (Supplement C), 52-56.
174. (a) Dadas, A.; Washington, J.; Marchi, N.; Janigro, D., **Improving the clinical management of traumatic brain injury through the pharmacokinetic**

modeling of peripheral blood biomarkers. *Fluids and Barriers of the CNS* **2016,** *13* (1), 21; (b) Lin, S.-N.; Slopis, J. M.; Butler, I. J.; Caprioli, R. M., **In vivo microdialysis and gas chromatography/mass spectrometry for studies on release of N-acetylaspartlyglutamate and N-acetylaspartate in rat brain hypothalamus**. *Journal of Neuroscience Methods* **1995,** *62* (1), 199-205.

175. Shen, A.; Zhang, B.; Ping, J.; Xie, W.; Donfack, P.; Baek, S. J.; Zhou, X.; Wang, H.; Materny, A.; Hu, J., **In vivo study on the protection of indole-3-carbinol (I3C) against the mouse acute alcoholic liver injury by micro-Raman spectroscopy**. **2009,** *40*, 550-555.
176. (a) Belli, A.; Sen, J.; Petzold, A.; Russo, S.; Kitchen, N.; Smith, M.; Tavazzi, B.; Vagnozzi, R.; Signoretti, S.; Amorini, A. M.; Bellia, F.; Lazzarino, G., **Extracellular N-acetylaspartate depletion in traumatic brain injury**. *Journal of Neurochemistry* **2006,** *96* (3), 861-869; (b) Moffett, J.; Arun, P.; Ariyannur, P.; Namboodiri, A., **N-Acetylaspartate reductions in brain injury: impact on post-injury neuroenergetics, lipid synthesis, and protein acetylation**. *Frontiers in Neuroenergetics* **2013,** *5* (11).
177. R-Development-Core-Team *R: a language and environment for statistical computing*, the R Foundation for Statistical Computing: 2016.
178. Granger, J. H.; Schlotter, N. E.; Crawford, A. C.; Porter, M. D., **Prospects for point-of-care pathogen diagnostics using surface-enhanced Raman scattering (SERS)**. *Chemical Society Reviews* **2016,** *45* (14), 3865-3882.